TIMING ANALYSIS IN A CRYSTAL SCINTILLATOR WITH DUAL READOUT

Christopher Bryce Martin

Charlottesville,VA

Bachelor of Science, Widener University, 2021

A Thesis submitted to the Graduate Faculty

of the University of Virginia in Candidacy for the Degree of

Master of Science

Department of Physics

University of Virginia

August 2024

Robert J. Hirosky, Chair

Craig Group

Timing Analysis in a Crystal Scintillator with Dual Readout

Christopher Bryce Martin

(ABSTRACT)

With the introduction of Rutherford's theory of Atomic structure, following his famous gold foil experiment, the need for higher energies to probe deeper structures has been a moving goal post. The development of larger and more powerful accelerators, in the pursuit of furthering our understanding of atomic structure, requires the parallel progression of more robust and precise detectors. Calorimetry is the method of detection in which a proxy is utilized to measure the energy of particles. The proxy by which information may be attained may be the temperature, light, or the charge gathered from interactions observed by such a detector. With the information gathered in large experiments, one can characterize the energy, trajectory, or species of particles involved in such interactions within the calorimeter. Currently, the Large Hadron Collider (LHC) is the largest and most powerful accelerator in the world. Complementary to such an accelerator is an array of advanced detectors. These detectors include ATLAS, ALICE, LHCb and CMS. In particular the Compact Muon Solenoid (CMS) relies on calorimetry to investigate frontier physics such as that of the Higg's Boson or dark matter candidates. The next step in accelerators includes new high energy e^+e^- machines or "Higgs factories". To prepare for this next leap, the development of more sophisticated detectors is paramount. One such approach is to enhance the performance of calorimeter detectors via "Dual-Readout" (DR) capabilities. One such R&D program utilizing this approach is CalVision. In this work, data from a testbeam taken in April 2023 is analyzed to study the timing resolution

of a DR system. The analysis scope is confined to minimum ionizing protons (MIPs) in the crystal. The results indicate promising trends and provide insight to better improve timing resolution in the future. With such observations, improvements can be made on particle flow algorithms and particle identification in jets and showers.

Dedication

To the amazing people I was able to cross paths with in this program. Your friendships mean the world to me and your passions motivate me continuously.

To Heewon for your unwavering support and patience.

Acknowledgments

I would like to thank:

Robert Hirosky for providing the opportunity to work in this field as I dreamt growing up, and finding time in your hectic schedule to meet when possible.

Grace Cummings for bringing me into this project and offering constant guidance and discussion. The mentoring you imparted spurred my natural curiosity to dig deeper and understand when possible.

Alexander Ledovskoy for letting me ask every question under the Sun and providing me your full attention. Your casual wisdom never left me empty handed.

Lastly, Craig Group for your time and feedback during my defense. I greatly enjoyed discussing my work with you.

Contents

List of Figures

Chapter 1

Introduction

1.1 Calorimetry: Motivation

Calorimetry is the method of detection in which the incoming particles are absorbed, and the information collected is used to render their four momenta. The design of any given calorimeter is determined based on the need of the experiments with which it will be paired. Recently, the Department of Energy and the National Science Foundation produced the Basic Research Needs report [1]. Considerations are made for upcoming advances in particle physics and the technical requirements to achieve them. Ambitious goals are to perform measurements of the Higgs boson to sub-percent precision, to explore its connection with dark matter, and to discover new particles at multi-TeV scales [2]. The construction of the Large Hadron Collider's successor, the Future Circular Collider (FCC), holds vast potential for probing beyond our current understanding of the Standard Model. Studies of the Z boson and Higgs boson production in e^+e^- collisions will require high jet resolution with 90% of final states containing jets [2]. The search for rare new processes would benefit greatly from improvements in electromagnetic resolution. With the promise of better colliders and higher energies comes the obligation for detectors on par.

1.2 Calorimetry: Challenges

Typically, a calorimeter operates by absorbing an incoming particle and measuring the signals produced from the interaction. These interactions can be divided into electromagnetic (EM) and hadronic (non-EM) components, both of which are present in hadronic interactions. Any interactions such as Compton scattering, pair production, Bremsstrahlung, photoelectric effect, etc. can be designated as the EM contribution to hadronic showers. The remaining interactions, typically strong interactions, are the non-EM portion of the shower (Figure 1.1). The issue at hand stems from the non-EM showers whose contributions to the energy often go missing. The nature of the strong interaction implies the loss of energy due to the nuclear binding energy in nuclear breakups. Up to 40% of the non-EM energy may be expended in this manner [3], a contribution of about 8 MeV/nucleon. Other sources of energy loss may be attributed to shower leakage and the escape of hadrons with small interaction cross sections. The complexity only compounds as it is found that this invisible energy fluctuates on an event-by-event basis. As a result, the hadronic response of the calorimeter becomes nonlinear, and the energy resolution of the detector will be diminished. The goal of the Dual Readout approach is to address these challenges.

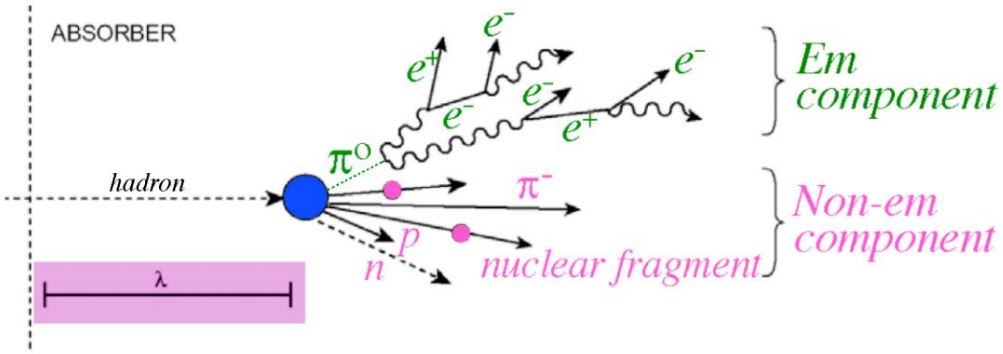

Figure 1.1: Diagram of a typical showering event. The EM showers are initiated by the presence of the neutral pion (π^0) which decays into two gammas. The hadronic cascade consists of strong interactions contributing to missing energies. [3]

1.3 Dual-Readout Calorimetry

In a given event, the energy can be split between EM and non-EM signals. The fraction of energy belonging to EM signals is denoted f_{em} (1.1) [2] with a dependence on the energy of the incoming particle (E) and the properties of the calorimeter (E_0, k)[1].

$$< f_{em} >= 1 - [\frac{E}{E_0}]^{(k-1)} \tag{1.1}$$

This fraction of signal belonging to EM showers typically varies on an event-by-event basis and is non-Gaussian, as illustrated in (Figure 1.2). The leakage of showers, nuclear binding energy, or the escape of neutrinos and neutral hadrons contribute to these fluctuations. As a result, there exists an invisible energy which impacts

[1]Both values must be determined experimentally for a given calorimeter and depend on the material. E_0 relates the to average multiplicity of hadronic interactions and k is a power [2].

the energy resolution, linearity and response function for hadrons. The goal of Dual Readout is to use complementary information on the relativistic signal (C) and the non-relativistic/scintillation signals (S) to apply corrections for this missing energy on an event-by-event basis.

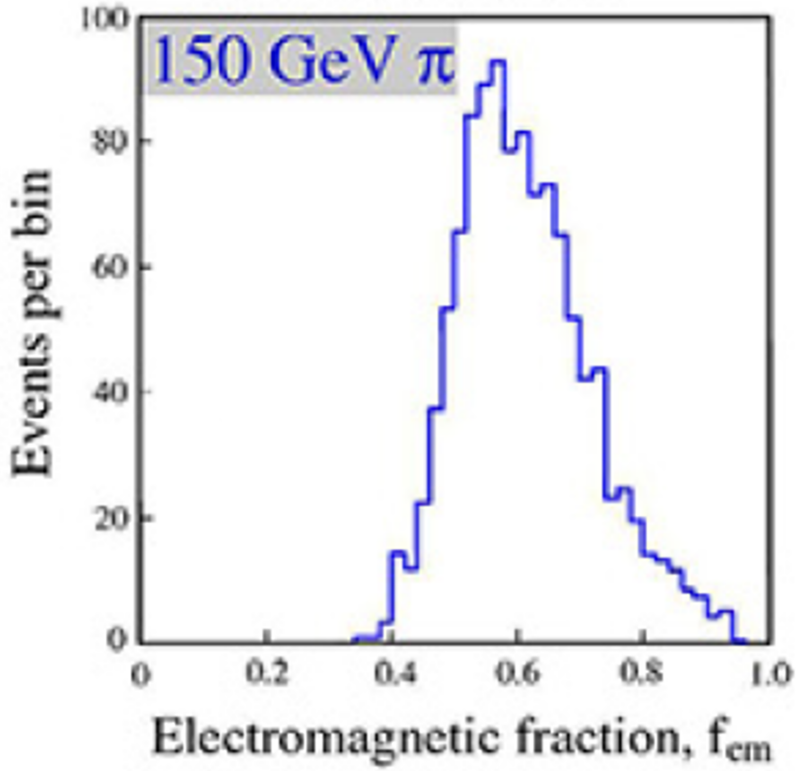

Figure 1.2: Visualization of the asymmetric fluctuations in the fraction of EM energy in showers. Experimental data from a lead and copper based sampling calorimeter with 150 GeV π^-s triggering showers [2].

The relativistic signal includes Cherenkov radiation emitted by charged particles traveling at speeds greater than the phase velocity of the material (v > c/n) with index of refraction n[2]. The majority of Cherenkov signal is imparted by the EM showers and is otherwise less sensitive to the non-EM showers. To get an idea of the distribution of energy in a given shower, one can consult a GEANT4 simulation of showers

[2]for Lead Tungstate ($PbWO_4$) n= 2.2

in PbWO_4. The distribution of energy deposition by particle species in high energy pion-initiated showers with respect to velocity (Figure 1.3 [left]) first shows that protons primarily make up the non-relativistic sources of energy deposition. The number of inelastic interactions is correlated with the invisible energy (Figure 1.3 [right]). Information on the relativistic sources of energy deposition (largely electrons and positrons) can be used on an event-by-event basis to improve hadron energy resolution because it effectively serves as a proxy for the invisible energy.

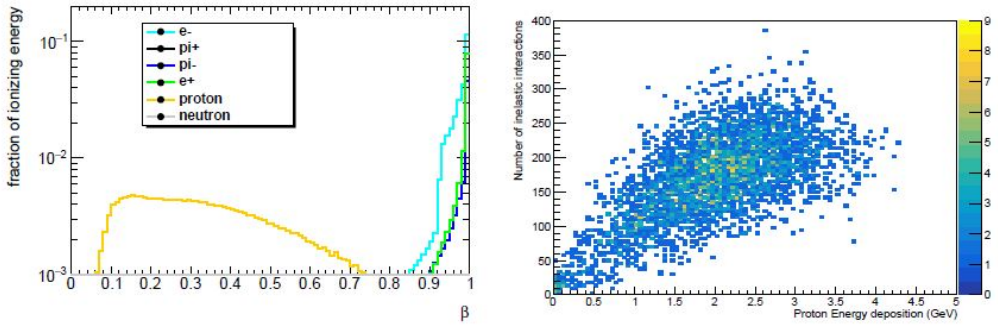

Figure 1.3: GEANT4 simulation of PbWO_4 showers initiated by high energy charged pions. Depicted [left] is the energy deposited with respect to the relativistic speed of particles in the shower. On the [right] an estimation of inelastic collisions expected for protons of a given energy in the crystal.[4]

The expressions for the two signals are given in (1.2) and (1.3) [2] with linear dependencies on energy. The ratio (e/h) represents the relative response of the calorimeter for pure EM and pure hadronic signals[3]. Typically, one calibrates these signals to electrons of known energy E such that the calorimeter response to pure EM showers becomes $< C > /E =< S > /E = 1$ where $f_{em} = 1$. Any subsequent measure of hadronic showers will result in $f_{em} < 1$. Energy dependence can be removed by taking the ratio, and algebraically one can determine f_{em} for any given event based

[3]This ratio is experimentally determined for a given calorimeter. Often, these responses are normalized with respect to minimum ionizing particles (MIPs) [2].

on the measured C and S (1.4) [2].

$$S = E[f_{em} + \frac{1}{(e/h)_S}(1 - f_{em})] \tag{1.2}$$

$$C = E[f_{em} + \frac{1}{(e/h)_C}(1 - f_{em})] \tag{1.3}$$

$$f_{em} = \frac{(h/e)_C - (C/S)(h/e)_S}{(C/S)[1 - (h/e)_S] - [1 - (h/e)_C]} \tag{1.4}$$

Consequentially, the actual energy of the incoming signal (E) can be better estimated by using the two components (1.5)[2]. In this calculation, the invisible energy is effectively estimated, and the energy resolution can be improved. In (Figure 1.4) a visualization of the process is provided. The plot defines the green dashed C = S line intersecting the calibration point (1,1) which characterizes pure EM showers. Hadronic showers, instead, land on the red line whose tangent produces angle θ (1.6) with respect to the horizontal. The red line connects two extremes of activity; on the bottom, purely hadronic events would reside where f_{em}= 0 and at the other end f_{em} = 1 (EM showers). A point occurring on the red line (S,C) for an arbitrary hadron shower will be corrected with the recovered energy and effectively projected to the EM shower response as if f_{em} were equal to unity.

$$E = \frac{S - \chi C}{1 - \chi} \tag{1.5}$$

$$cot(\theta) = \frac{1 - (h/e)_S}{1 - (h/e)_C} = \chi \tag{1.6}$$

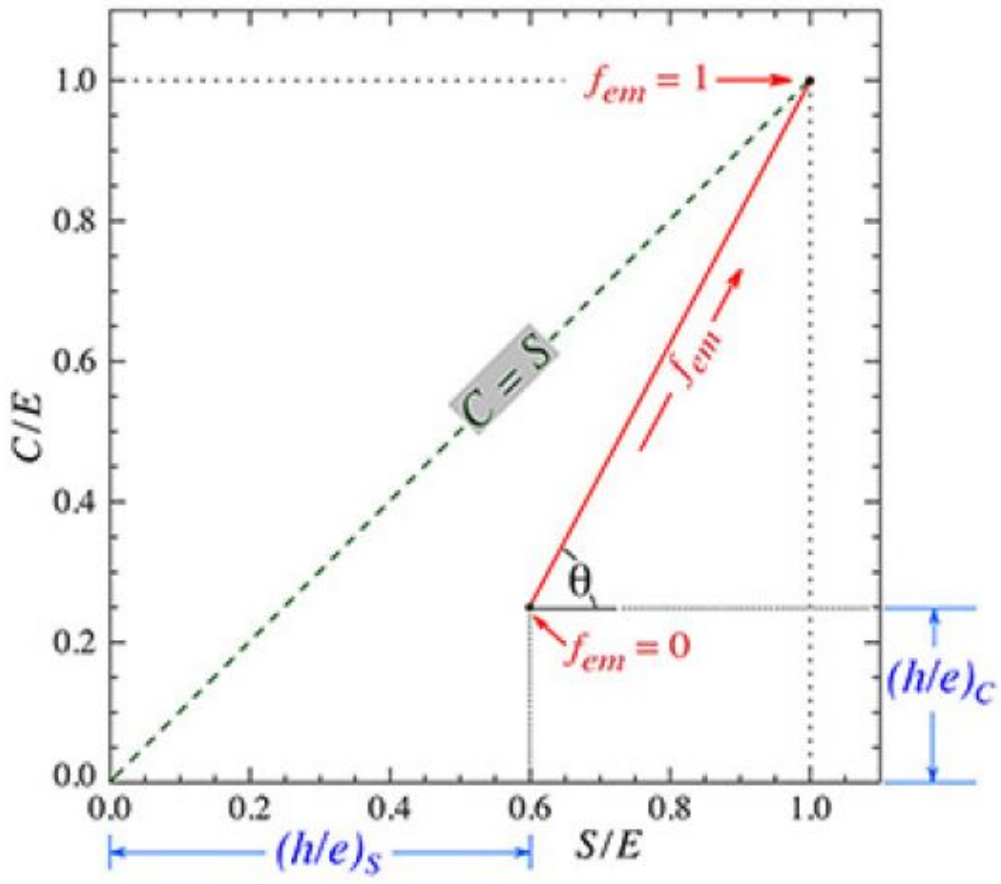

Figure 1.4: A visualization of shower signals in a calorimeter and their regimes. Pure EM showers will appear around the point f_{em}=1, as calibration intended. Any hadronic showers will land on the red line defined by the angle θ, which characterizes the difference in response (e/h) for scintillation and Cherenkov signals [2].

Such a method proves promising in concept and well understood in practice. One of the early uses of the DR method emerged from the Dual-REad-out Module (DREAM) calorimeter work from a collaboration between Texas Tech University, Iowa State, and University of California in 2004[4] [6]. The DREAM calorimeter (Figure 1.5) was a hadron calorimeter consisting of an array of copper rods filled with optical fibers

[4]Initial attempts to utilize dual readout methods were implemented in the ACCESS calorimeter. ACCESS, a cosmic ray experiment for the International Space Station, found success in the DR method but was unable to take full advantage due to its very thin structure [5].

designated to detect scintillation and Cherenkov light separately. Cherenkov signal data collected for showers initiated by 100 GeV π^- beam can be seen in (Figure 1.6). Noticeably, the distribution of the total signal is broad and asymmetric (a) unless the events are redistributed in narrow regions of f_{em} where the signals are individually well resolved (b). The fluctuations of f_{em} skew data into poor resolution and the same can be observed in the scintillation signal. When corrections are applied (Figures 1.7 and 1.8), the entirety of the data becomes well resolved and symmetric about the mean. A visual aid of distributions with respect to the plot in (Figure 1.4) can be seen in (Figures 1.9 and 1.10) in which the signals are shown to meander about the red line defined by the angle θ (1.6) and after correction, they cluster about the point (1,1) just as pure EM showers do.

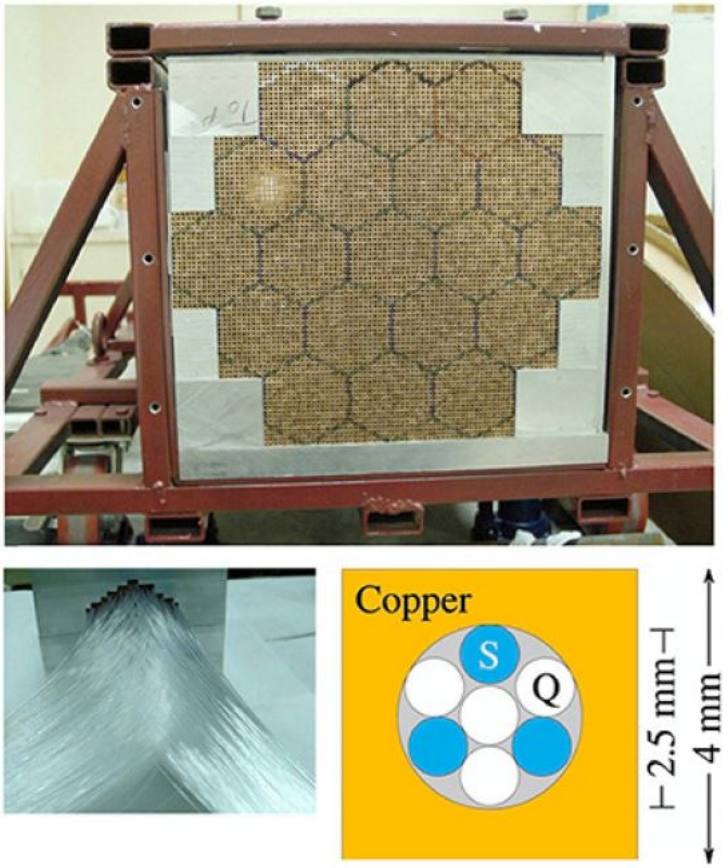

Figure 1.5: The Dream Detector consists of 5580 copper rods, 2m long and hollowed out with an internal diameter of 2.5 mm. Within each rod several optical fibers were placed, 3 for detecting scintillation (S) and 4 to detect Cherenkov (labeled "Q" here). The detector face reveals 19 hexagonal towers, consisting of 270 rods each. From each tower, 2 bundles of optical fibers individually couple to a photomultiplier tube (PMT) for readout (1 S bundle and 1 Q bundle). [6]

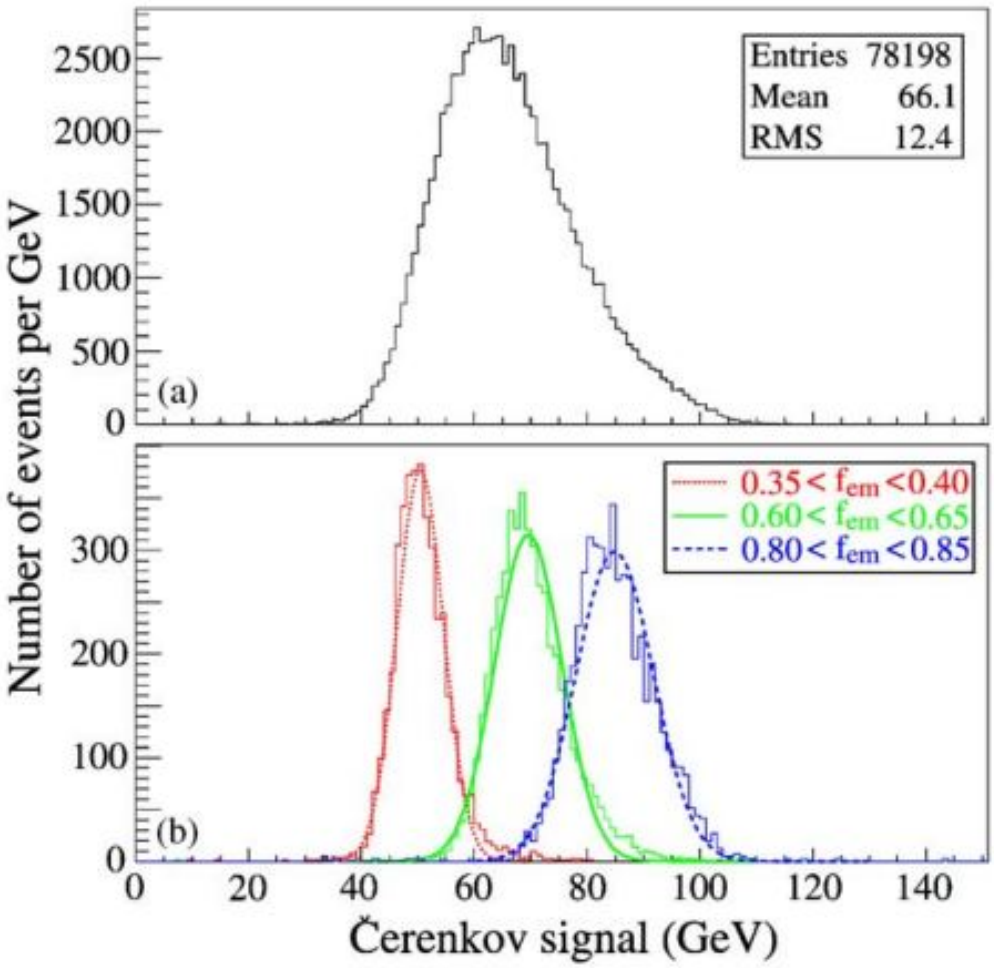

Figure 1.6: Distribution of total Cherenkov signal for 100 GeV π^- induced showers inside the DREAM detector (a) and the same signal organized by f_{em} value (b). [6]

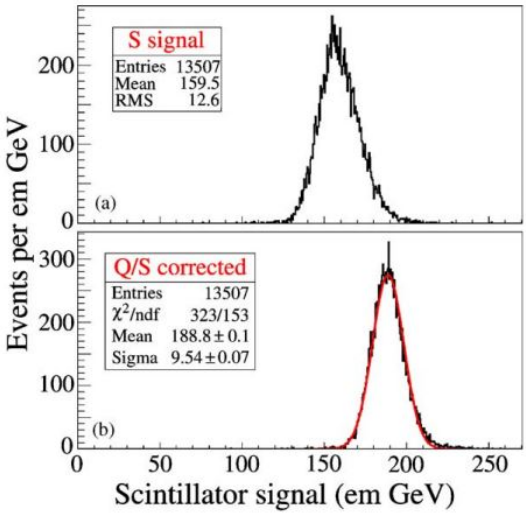

Figure 1.7: Scintillation signal inside DREAM for 200 GeV π^- induced showers prior to corrections (a) and after corrections (b). [6]

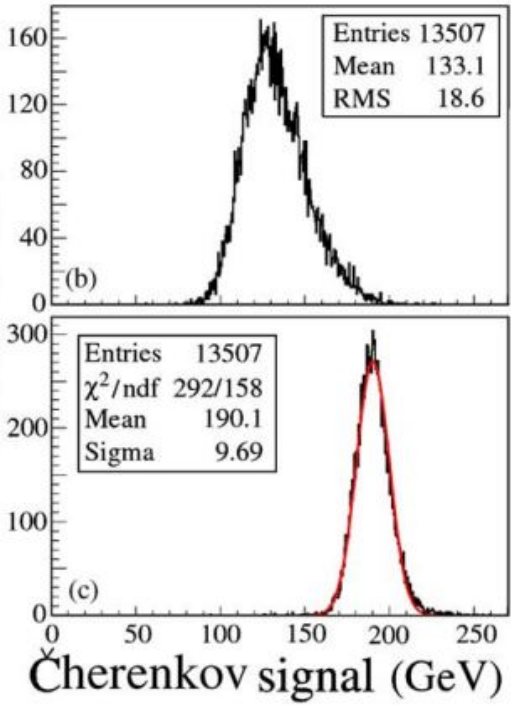

Figure 1.8: Cherenkov signal inside DREAM for 200 GeV π^- induced showers prior to corrections (b) and after corrections (c). [6]

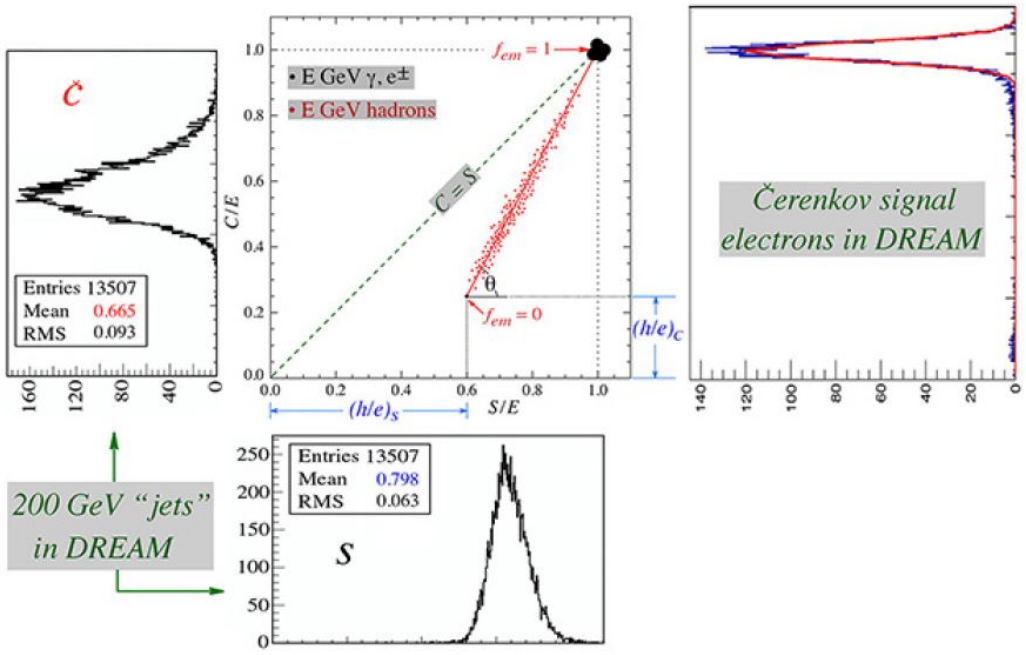

Figure 1.9: A visual correspondence of the correction method with respect to EM showers. As noted in previous figures, the signals are asymmetric and distributed about the red line defined by θ. Pure EM showers produce points clustered about (1,1) as seen with the Cherenkov signal sample [2].

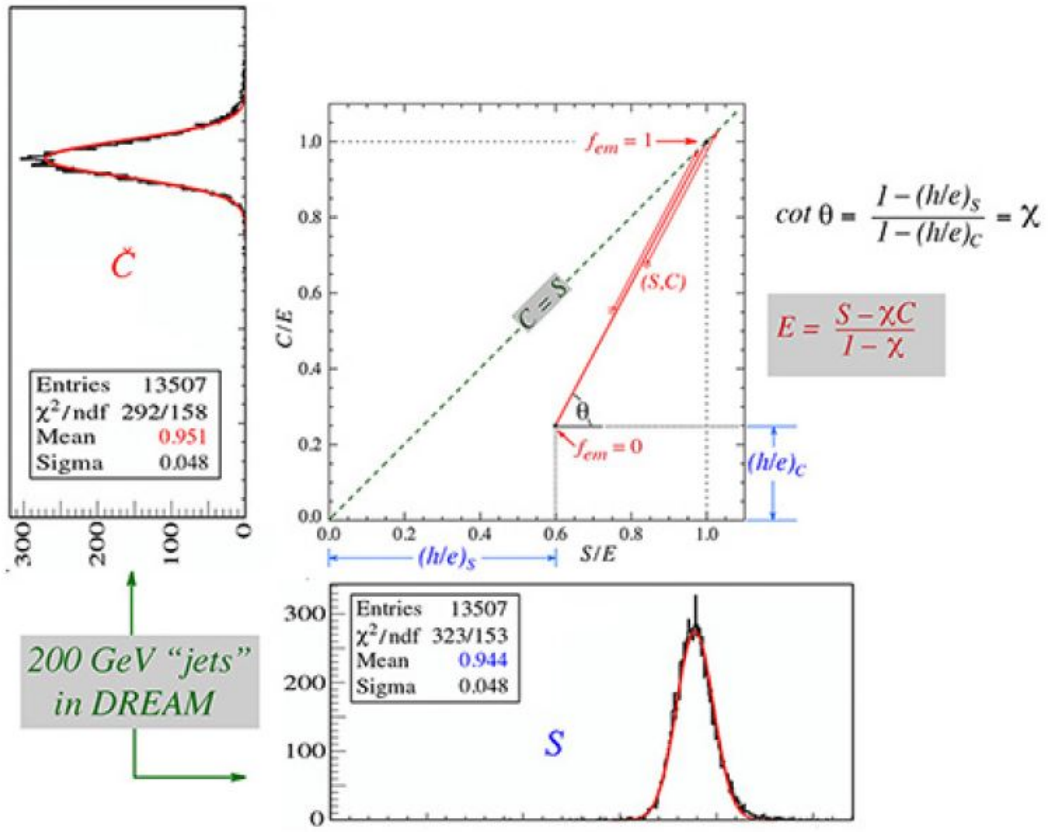

Figure 1.10: The resulting correction applied to data presented in previous figures and it's effect. Corrected data behavior mimics that of pure EM showers as signals approach the point (1,1) [2].

1.4 CalVision

CalVision is a consortium dedicated to research and development for future detector technologies in preparation for future colliders. Dual Readout is one such technology to be improved and capitalized on within the CalVision calorimeter concept (Figure 1.11). The Segmented Crystal Electromagnetic Precision Calorimeter (SCEPCal) is a DR EM calorimeter consisting of two-timing layers and two longitudinally segmented homogeneous scintillating crystals. Such a DR EM calorimeter paired with a DR

hadronic calorimeter will be able to achieve excellent energy resolution for both EM and hadron initiated showers. A branch of R&D within CalVision is dedicated to the evaluation of candidate homogeneous crystals to be used in the SCEPCal to achieve this end[5].

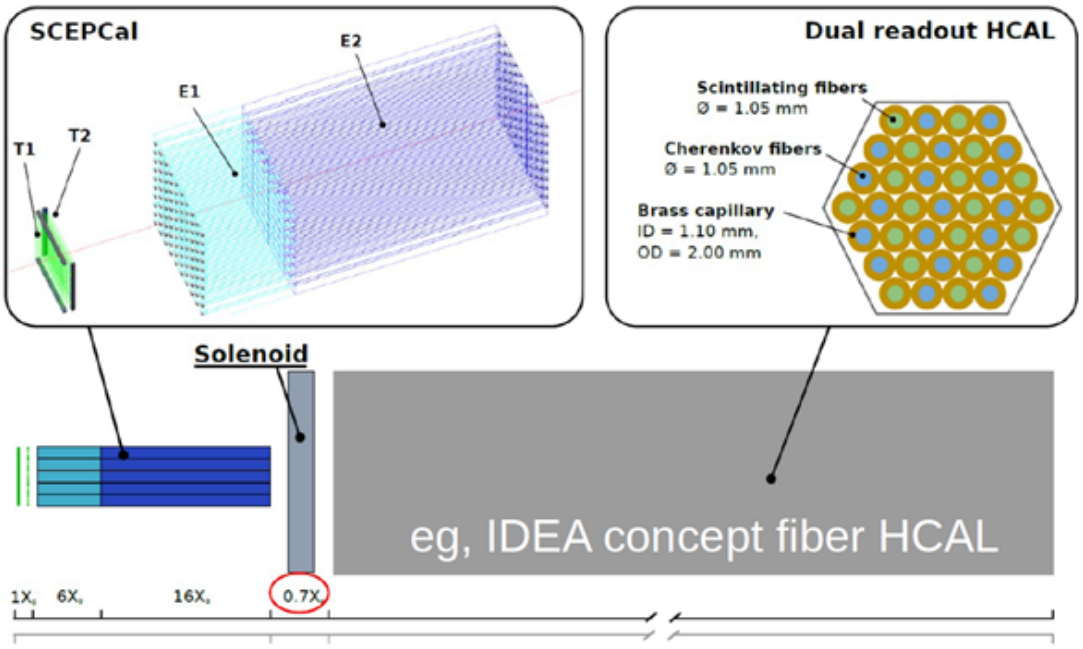

Figure 1.11: The CalVision calorimeter concept including an optional timing layer (T1 and T2), longitudinally segmented homogeneous scintillating crystals (DR EM calorimeter) and a conceptual DR hadron calorimeter with a thin solenoid between the two. [7]

Whereas the DREAM concept has distinct readout channels for S and C, in CalVision, the two signals must be separated after detection in a homogeneous crystal calorimeter in order to implement DR. There are several opportunities to separate the signals resulting from scintillation (S) and Cherenkov (C) by taking advantage of properties inherit to the production of Cherenkov light. Firstly, it is noted that Cherenkov photons are emitted in a cone along the trajectory of the particle with the

[5]Candidate crystals include Bismuth Silicon Oxide (BSO), Bismuth Germanate (BGO) and Lead Tungstate ($PbWO_4$)

angle of emission determined by (1.7). In previous experiments such as the RD52 collaboration studies [8] this was taken into account via dedicated detectors positioned to only receive photons at specific angles (Figure 1.12). Alternatively, knowledge of the polarization of Cherenkov provides the opportunity to separate signal using polarization filters as carried out by the RD52 collaboration [9](Figure 1.13).

$$Cos(\theta_C) = \frac{1}{n * \beta} \tag{1.7}$$

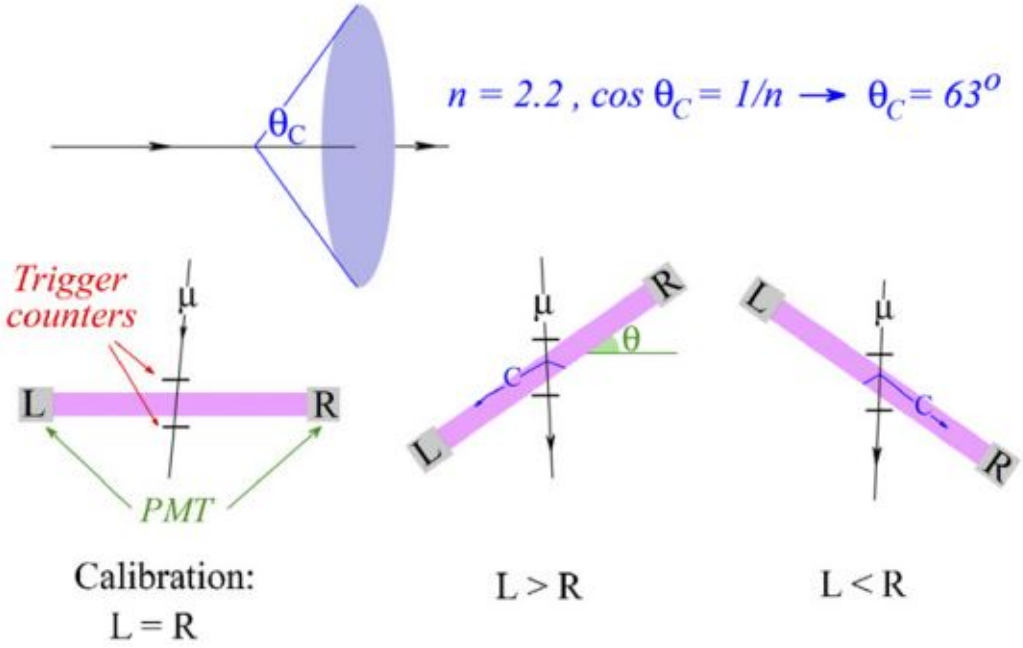

Figure 1.12: PMTs are attached to both sides of a $PbWO_4$ crystal in the path of a 150 GeV beam of μ^+ particles. The crystal is rotated in discrete angles to measure the asymmetry in response. It was found the signals were symmetric about $\theta = 0$ and the maximal asymmetry was found at $90° - \theta_C$. [8]

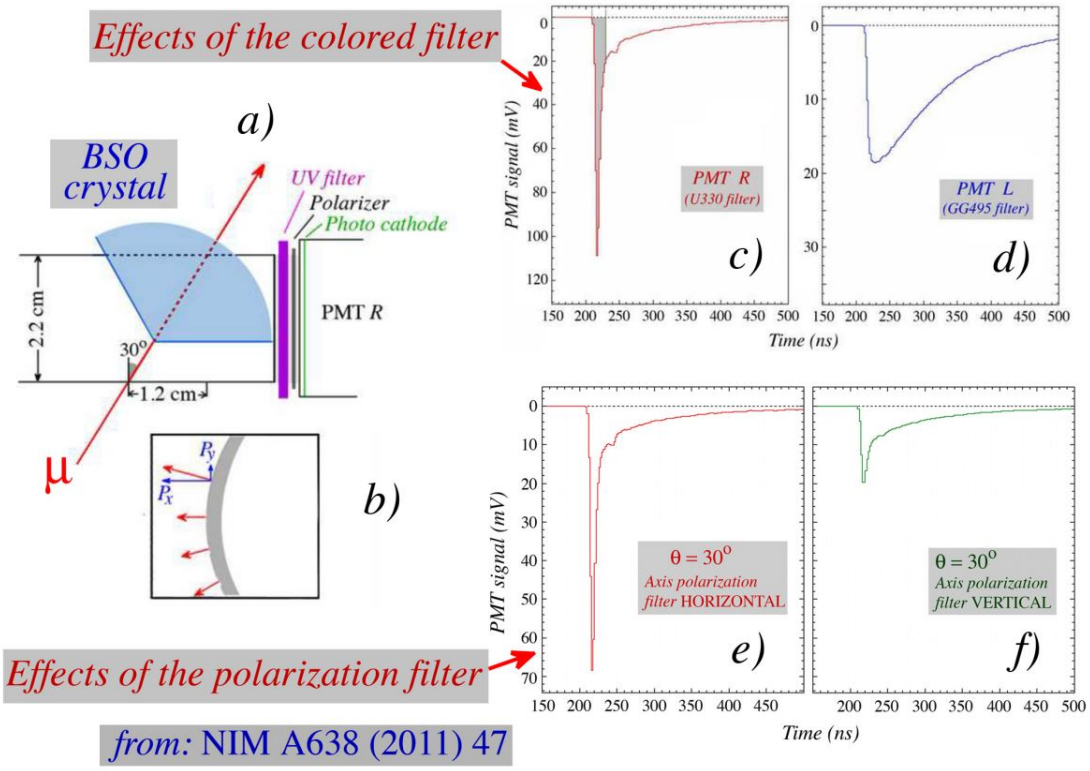

Figure 1.13: The experiment carried out by RD52 consisted of a bismuth silicate (BSO) crystal meant to extend the decay time of scintillation light and further separate its spectrum from that of Cherenkov. The beam composed of 180 GeV π^+ penetrated the BSO crystal, oriented 30° with respect to the beamline (Fig 1.12) (a). The polarization vector of Cherenkov is depicted in (b) and the results of using two spectral filters are depicted in (c) and (d). The effect of the spectral filter was to remove the scintillation from the Cherenkov signal. The UV filter used on the right PMT was successful, except for the small persisting scintillation evidenced by the long decay tail on the final signal (c). The Crystal was then oriented in the optimal $\theta = 30°$ position with the UV filter applied. The results (e) and (f) demonstrate the near total removal of signal once the polarization filter was oriented perpendicular to the Cherenkov signal's polarization. Remaining signals are sourced by persistent scintillation. [9]

Lastly, and most relevant, one can utilize Cherenkov's spectral and pulse shape characteristics. In this respect, one could differentiate the pulses of incoming signals based on the timing information, as will be seen in (Section 2.2), since Cherenkov

is expected to arrive sooner (Figure 1.14). One could also take advantage of the spectrum of scintillation light and Cherenkov light and apply a filter to the detectors to nullify the overwhelming presence of scintillation light (Figure 1.15) as seen previously (Figure 1.13 (c) and (d)).

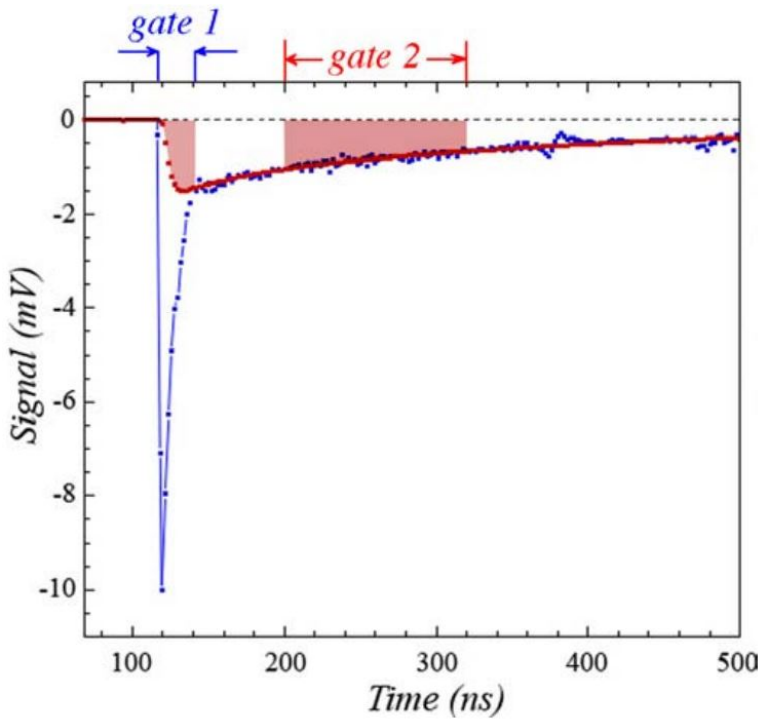

Figure 1.14: Performed by RD52 on a bismuth germanate (BGO) crystal with a UV Filter equipped to remove majority of scintillation. An external trigger opens two gates to isolate the first prompt Cherenkov signal in a 10 ns window and a second gate opens 30 ns later for a 50 ns window to capture remaining scintillation. [9]

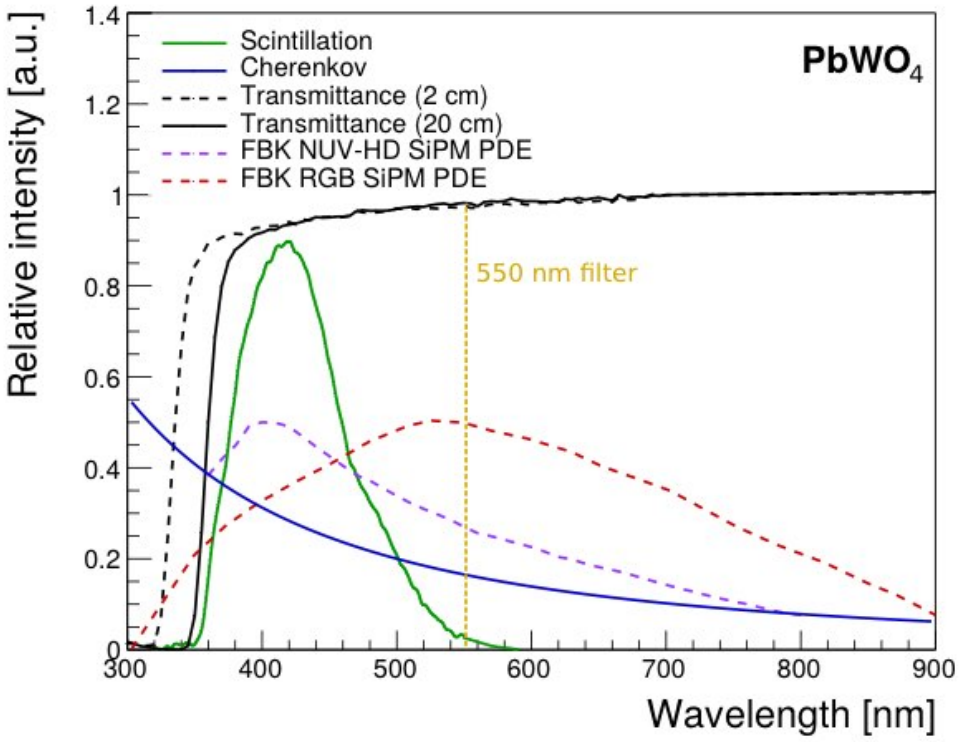

Figure 1.15: Comparison of the spectra for scintillation and Cherenkov signals that allow utilization of long wavelength signals in the Cherenkov distribution whilst filtering out the majority of scintillation. Transmission curves in $PbWO_4$ are drawn in black along with detection efficiencies for SiPMs adjusted to detect scintillation (UV) and both signal types (RGB) [7].

In contrast to earlier work, CalVision uses a SiPM-based readout, which is less expensive than PMT readout and also compatible with use in the magnetic field present in an FCC detector. Furthermore, the extended wavelength sensitivities of SiPMs allow sampling of the C spectrum to longer wavelengths, increasing the amount of light collected over the detector surface area. In the CalVision test beam of April 2023 at FermiLab, single crystals were irradiated with 120 GeV protons. Two crys-

tals were tested separately, $PbWO_4$ and BGO, with high densities ensuring compact EM showers and capability to produce substantial Cherenkov due to their refractive indices. The crystals were outfitted with 7 SiPMs[6] (Figure 1.16), and 1 microchannel plate detector (MCP) was used as a trigger and time reference. The backend SIPMs (channels 0-3) were placed downstream of the beam while frontend SiPMs (4-6) were placed upstream (Figure 1.17). The test beam consisted of roughly 60,000 protons per spill, each spill lasting 4 seconds and occurring 1 minute apart. The goal of the test beam was to consider the timing resolution and ensure sufficient detection of Cherenkov light for applying DR techniques. The test beam was carried out under 4 primary configurations (Figure 1.18). The filter used in half the configurations, meant to filter scintillation and preserve Cherenkov, was coupled via optical grease. A timing analysis of the $PbWO_4$ crystal with DR capabilities is presented. The analysis will remain focused on the minimum ionizing protons (MIPs) for their relatively consistent energy deposition. As a result, there will be a lack of showers. The Cherenkov light produced will originate from the protons themselves and the Scintillation, of course, a result of ionization by said protons.

[6] 8 SiPM were technically attached but only 7 (channel 0-6) were read out.

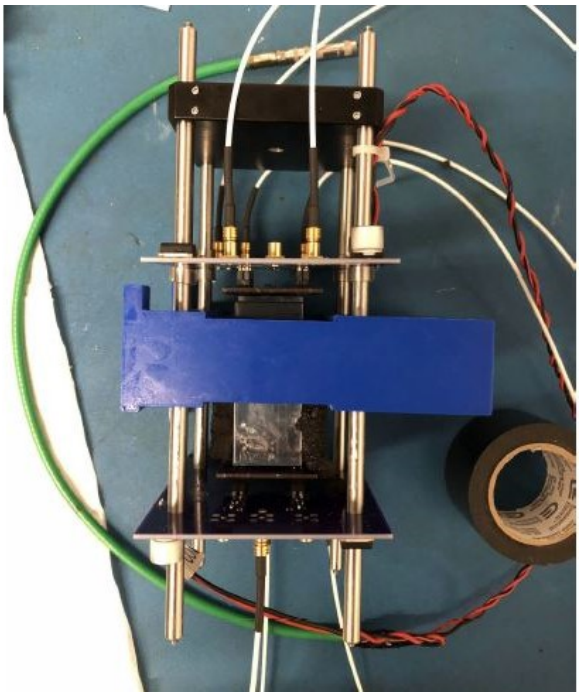

Figure 1.16: CalVision April testbeam apparatus used to secure the crystal of dimensions 2.5 x 2.5 x 6.0 cm. The SiPMs (Hamamatsu S14160-6050HS) were 6x6 mm and placed on both ends of the crystal. For the $PbWO_4$ crystal, a 660 nm interference filter was used, coupled via optical grease.

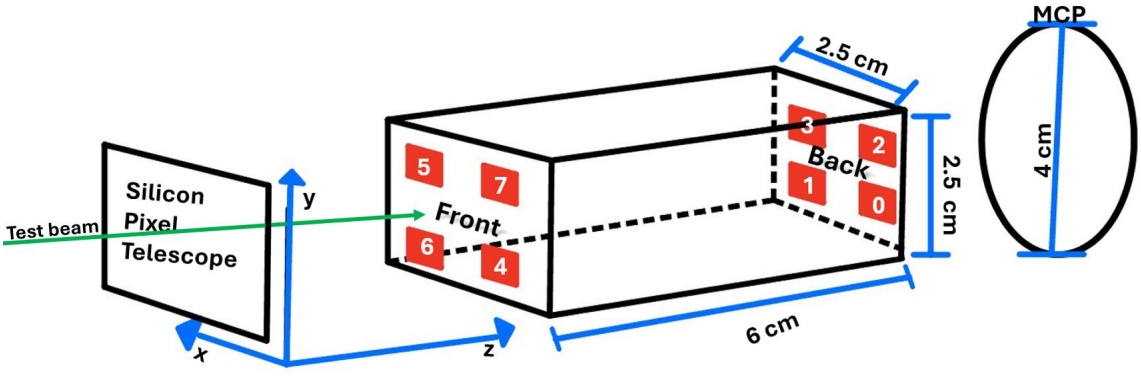

Figure 1.17: The 120 GeV proton beam passes through the silicon pixel telescope, for position tracking, and meets the frontend of the crystal (channels 4,5, and 6). If a filter is used, it is placed between the back face of the crystal and the backend channels (0,1,2, and 3). Lastly, the MCP trigger is seen on the far end, capable of a timing resolution up to 25 ps.

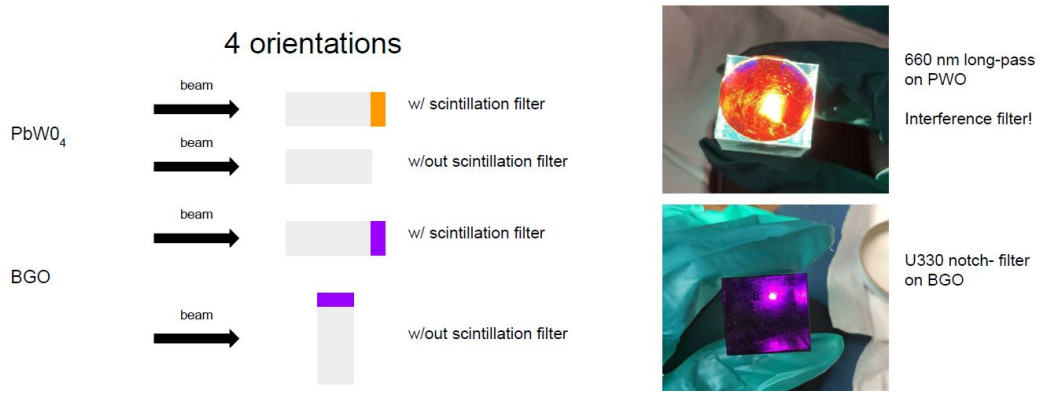

Figure 1.18: 4 Primary configurations were tested. The first two observed PbWO_4 placed parallel to the beamline either with or without the 660 nm interference filter. Other configurations used BGO crystal with an absorption filter in both cases, either along the beamline or oriented perpendicular to the beam. The PbWO_4 is the focus of this analysis. Credit: Grace Cummings.

In the following Section (Section 2.2), analysis of the timing resolution for the single crystal test is presented. The first discussion of timing analysis does not include the totality of work completed but serves as a starting point to understand the data and methods. The analysis also covers the timing resolution in the testbeam when a 660 nm interference filter was coupled to the backend of the PbWO_4 crystal. The interference filter serves to remove scintillation light and enable the DR method in future experimentation unrelated to the analysis itself. By first presenting the timing resolution for unfiltered data, it is motivated to explore methods to improve the resolution. Once these corrections are made, an analysis on the noticeably different filtered data set can be pursued. With the improvements implemented, a discussion of final results will follow. With the results gathered, conclusions will be drawn and actionable goals can be suggested for future work.

Chapter 2

Methods

2.1 Initial Analysis

Initial waveforms are generated on an event-by-event basis lasting about 60 ns. An example of such a waveform can be seen in (Figure 2.1)[1]. Individual events are dominated by high frequency noise that can be mitigated by taking an average of similar events. To select comparable events, their integrals are calculated and events with similar integrals have their amplitudes averaged together. A histogram of these average amplitudes over time compared to the integral can be seen in (Figure 2.2), from which a correlation is drawn between the single event waveform integral and an average pulse amplitude. The average amplitude of an event A'_{max} is then proportional to the integral of the event. For example, by taking events within an arbitrary range of integral values, their average pulse can be seen (Figure 2.3). Distributions of event amplitudes are seen (Figures 2.4 and 2.5), where pure noise wave forms peak around $A'_{max} = 0$, and MIP peaks are visible with radiative tails extending into the showering regime. It is designated that events with $A'_{max} < 80$ mV constitute a MIP event, setting the range of the analysis.

[1]Notation aside: "PWOp" refers to the parallel orientation lead tungstate crystal and the "F" denotes whether or not the filter is introduced on the backend of the crystal.

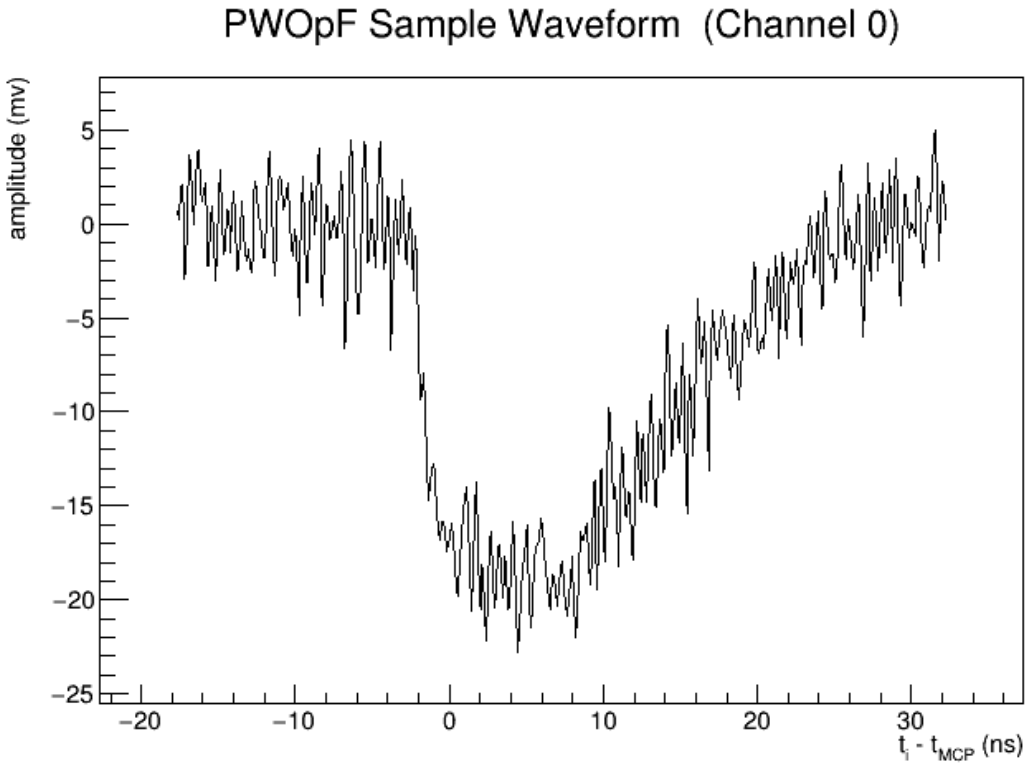

Figure 2.1: $PbWO_4$ Filtered Channel 0: Single Event Waveform. The time of the event is measured with reference to the trigger of the MCP (t_{MCP}).

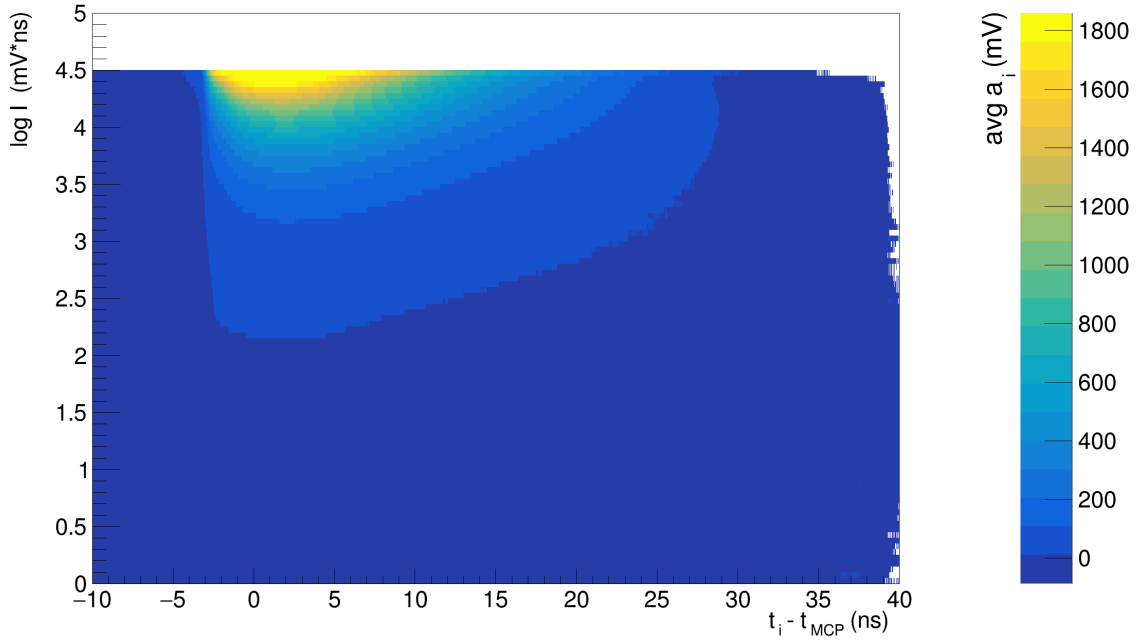

Figure 2.2: $PbWO_4$ Filtered Channel 0: Histogram of event integral Vs. average waveform. From such a distribution, projections of narrow bins of integral values allow the assignment of an average pulse amplitude to an event based on it's integral (integrals are plotted on a logarithmic scale) [10].

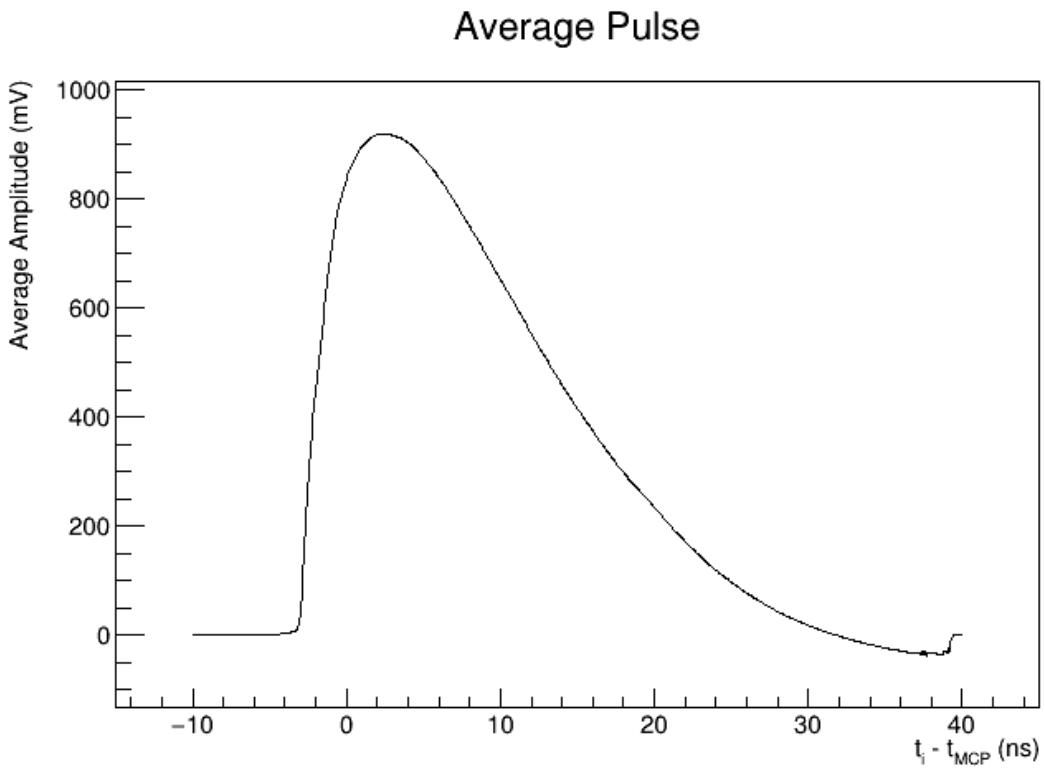

Figure 2.3: $PbWO_4$ Unfiltered Channel 0: average wave form projected from (Figure 2.2) for waveforms with integral values in an arbitrarily selected range.

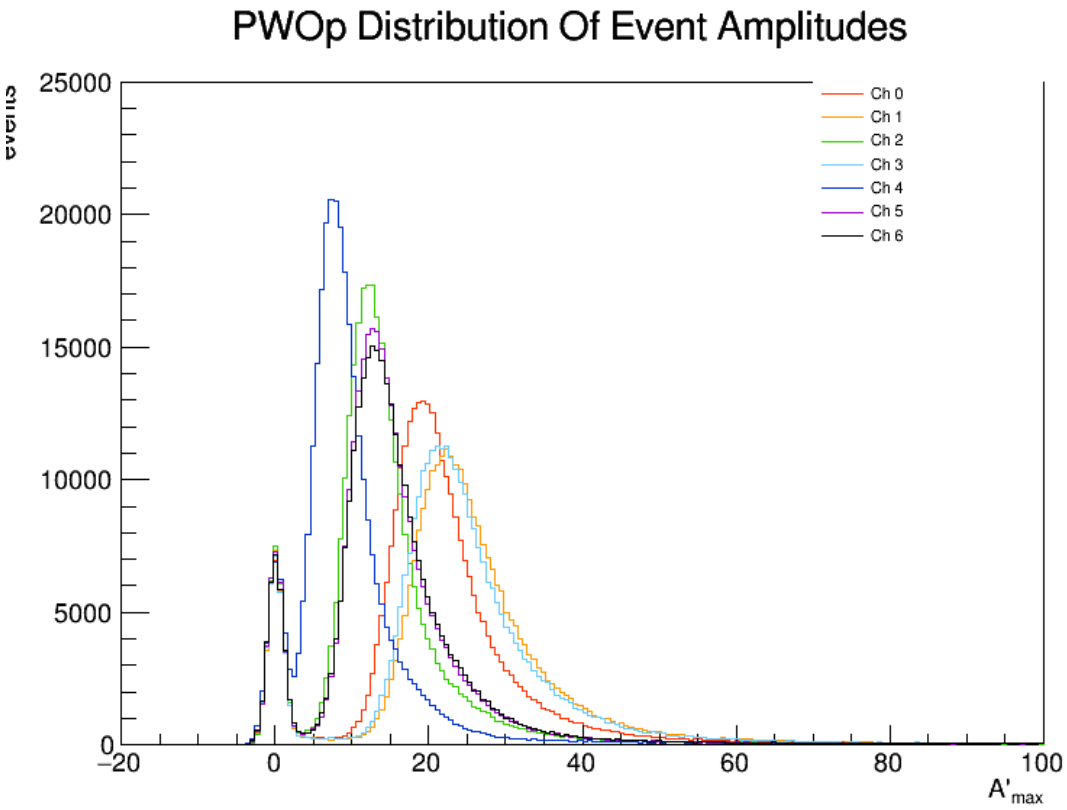

Figure 2.4: $PbWO_4$ Unfiltered, all channel distributions of typical event amplitudes A'_{max}.

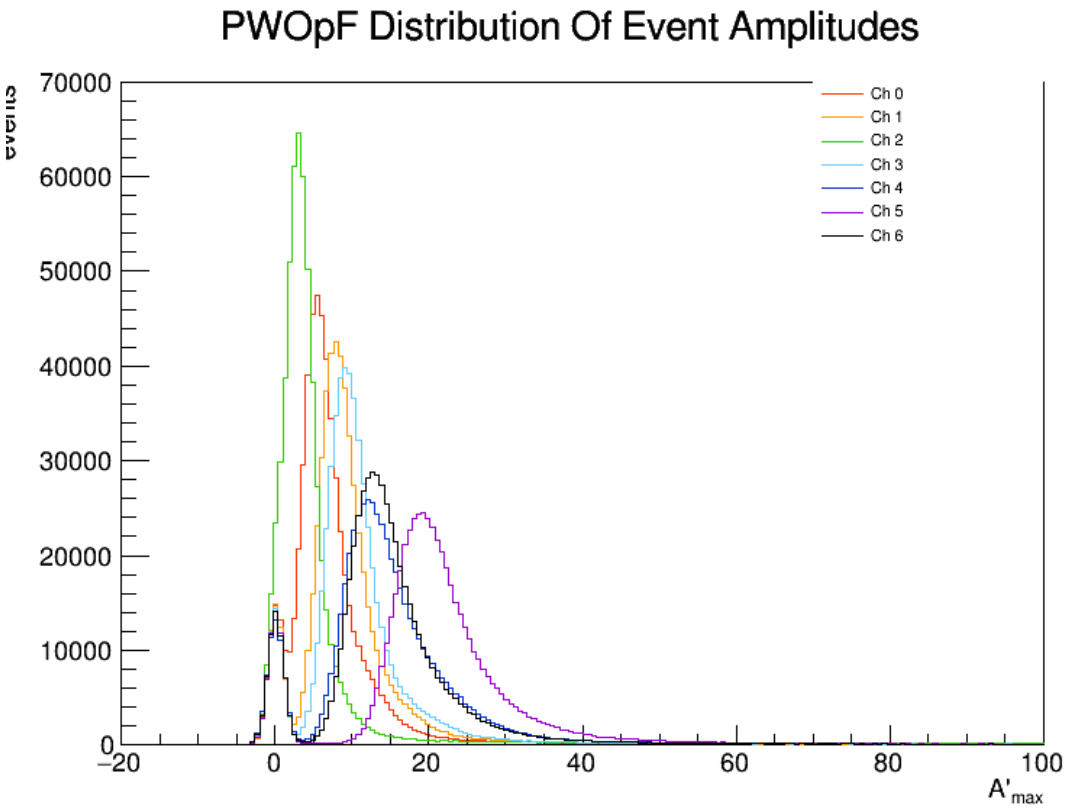

Figure 2.5: $PbWO_4$ Filtered event distributions of typical event amplitudes A'_{max}.

2.2 Timing Analysis of Unfiltered PbWO_4

For an individual event, the integrated waveform is generated (Figure 2.6) and from it, a time is specified for achieving a threshold voltage. 20 different threshold voltages are used (Figure 2.7) and from each, a 2D distribution of the timing of events and their relative amplitudes can be constructed (Figure 2.8). In the unfiltered dataset, these distributions are often straightforward with a singular central peak. When the filter is applied to the PbWO_4 crystal, the structure of these distributions becomes altered due to the separation of scintillation and Cherenkov light. The consequences are disruptive in characterizing a timing resolution for a given SiPM (Section 2.4).

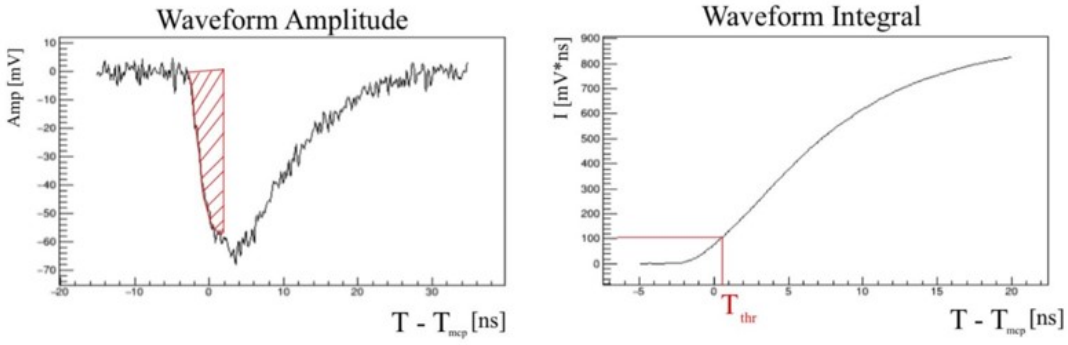

Figure 2.6: Sample single event waveform undergoing integration (left) and the corresponding threshold voltage timestamp T_{Thr} assigned based on the integrated waveform (right). Credit: Max Dubnowski

Int	Thr (mV*ns)	Int	Thr (mV*ns)
0	2.51	10	25.12
1	3.16	11	31.62
2	3.98	12	39.81
3	5.01	13	50.12
4	6.31	14	63.10
5	7.94	15	79.43
6	10.00	16	100.00
7	12.59	17	125.89
8	15.85	18	158.49
9	19.95	19	199.53

Figure 2.7: Table of exponentially generated threshold voltages used to assign timestamp T_{Thr} for an event.

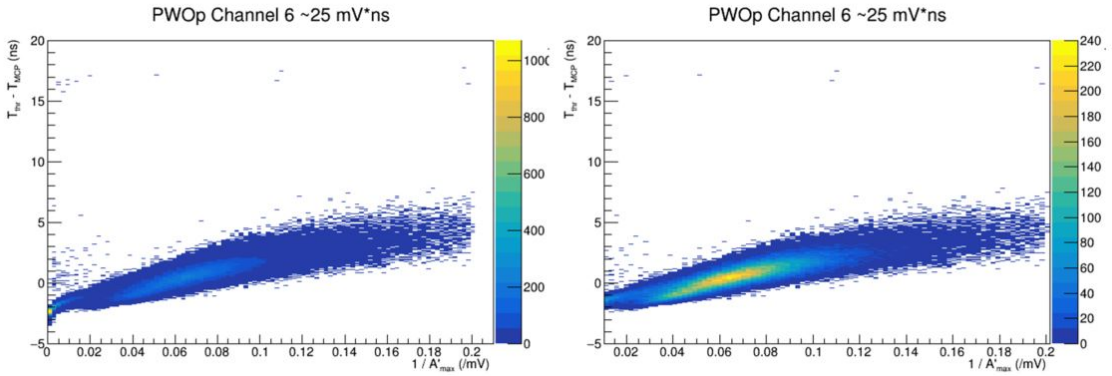

Figure 2.8: PbWO_4 unfiltered channel 6 at a threshold voltage of 25 mV*ns. Shown (left) is the distribution of events with respect to the timing $T_{Thr} - T_{MCP}$ and their (inverted) amplitudes A'_{max}. Shown (right) is the same plot truncated at an amplitude of 80 mV.

Beginning with the example of PbWO_4 unfiltered, one can consider the distribution shown in (Figure 2.8). Taking such a distribution, one can specify several bins of nominal amplitude[2] from which to project the timing of events. Projections of the events within the amplitude range in question are then fitted with a gaussian curve (Figure 2.9). The width of this curve will then characterize the timing resolution of the events in the given amplitude range for the channel observed when utilizing the specific threshold voltage for timing. Repeating this process for each configuration, one can gather the optimal timing resolution conditions. Figure (2.10) contains one such plot to evaluate the trend of timing resolution across Channel 6 for events with amplitude 31 - 35 mV.

[2]There were 7 nominal amplitudes studied with windows ±2 mV wide about the given values: (16 mV, 19 mV, 24 mV, 33 mV, 45 mV, 63 mV, and 87 mV).

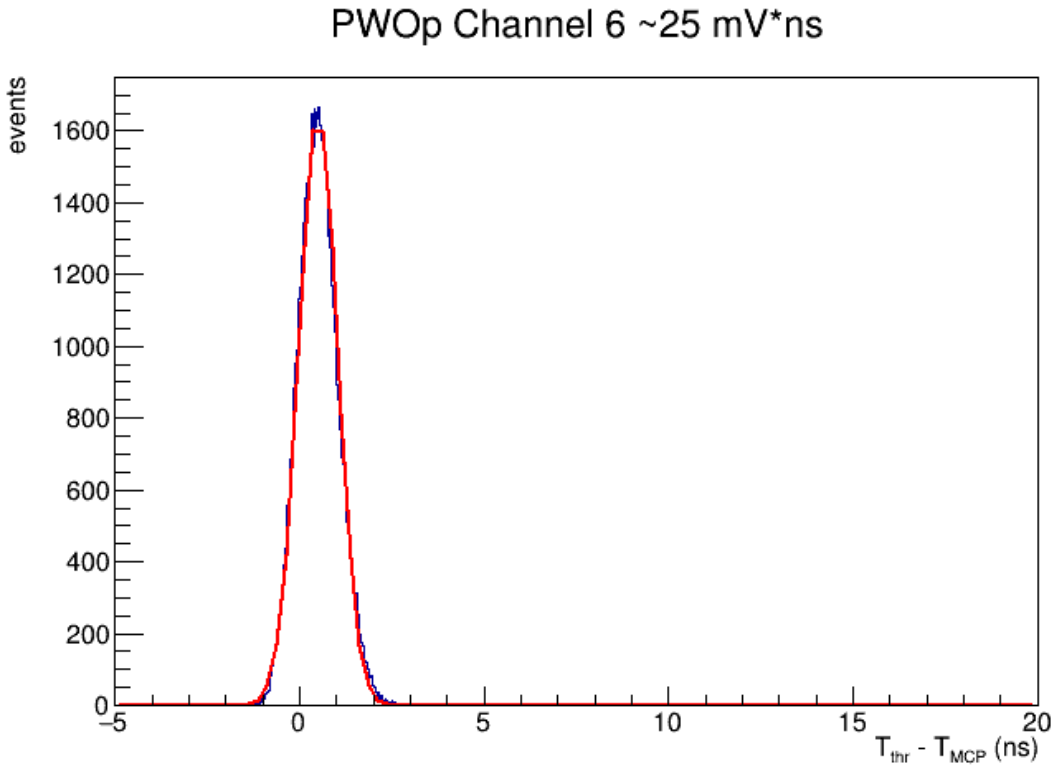

Figure 2.9: A projection of events in $PbWO_4$ unfiltered in which the threshold voltage of 25 mV*ns was used and events between 31-35 mV were selected. From this fit, a timing resolution is measured for these specific parameters (channel,amplitude,threshold).

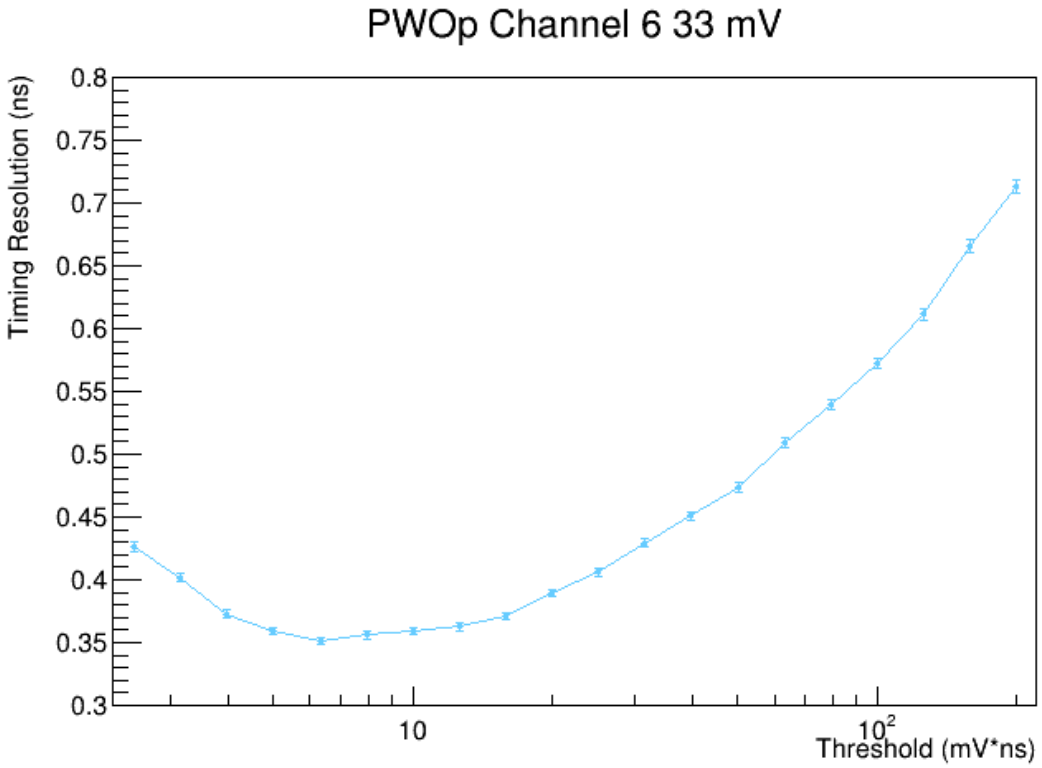

Figure 2.10: The culmination of many measurements across thresholds, such as that in (Figure 2.9), representing the timing resolution of channel 6 for events between 31-33 mV in unfiltered PbWO_4.

2.3 Improvement of Resolution

2.3.1 Amplitude Walk Corrections

Noticeably, distributions of timing and amplitude imply a dependency between the two. As the threshold voltage ramps up, the distribution for a given channel walks into an arcing curve. This dependence is nonuniform and inherently biases findings of timing resolution. To remove this dependence, the distributions are evaluated bin-by-bin in amplitude to determine the mean timing (T_{thr}-T_{MCP}). Then, on an

event-by-event basis, the timing is rebinned with the mean removed to eliminate the dependency. The result (Figure 2.11) shows success wherein the distributions have smeared out into smooth, flat peaks centered about 0 ns.

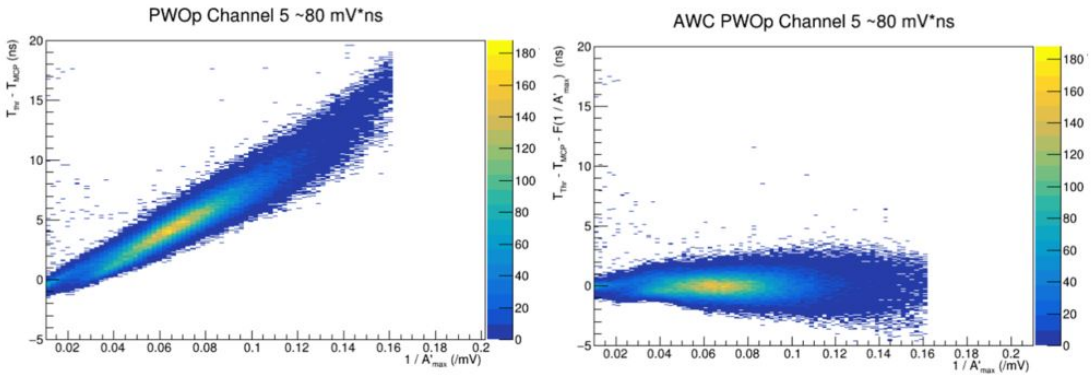

Figure 2.11: Unfiltered Channel 5 (at a threshold voltage of about 80 mV*ns) before (left) and after (right) amplitude walk corrections.

From this set of corrections, the process of calculating the timing resolution is repeated with improved results. The improvements are noticeable at high threshold voltages, one such example can be demonstrated here. (Figure 2.12) presents the superimposed distribution of timing vs. amplitude for Channel 0 at a Threshold of about 200 mV*ns, before and after amplitude walk corrections. The distributions are projected between 14 mV and 18 mV to produce similar histograms of timing (Figure 2.13). By visual inspection, one can surmise the nonuniform amplitude dependence on timing produces wider and skewed peaks, compromising the reliability of fits. The improvement is further established in (Figure 2.14), where a comparison of the timing resolution trends diverge at higher amplitudes. It can be stated that amplitude walk corrections improve timing resolution as a result.

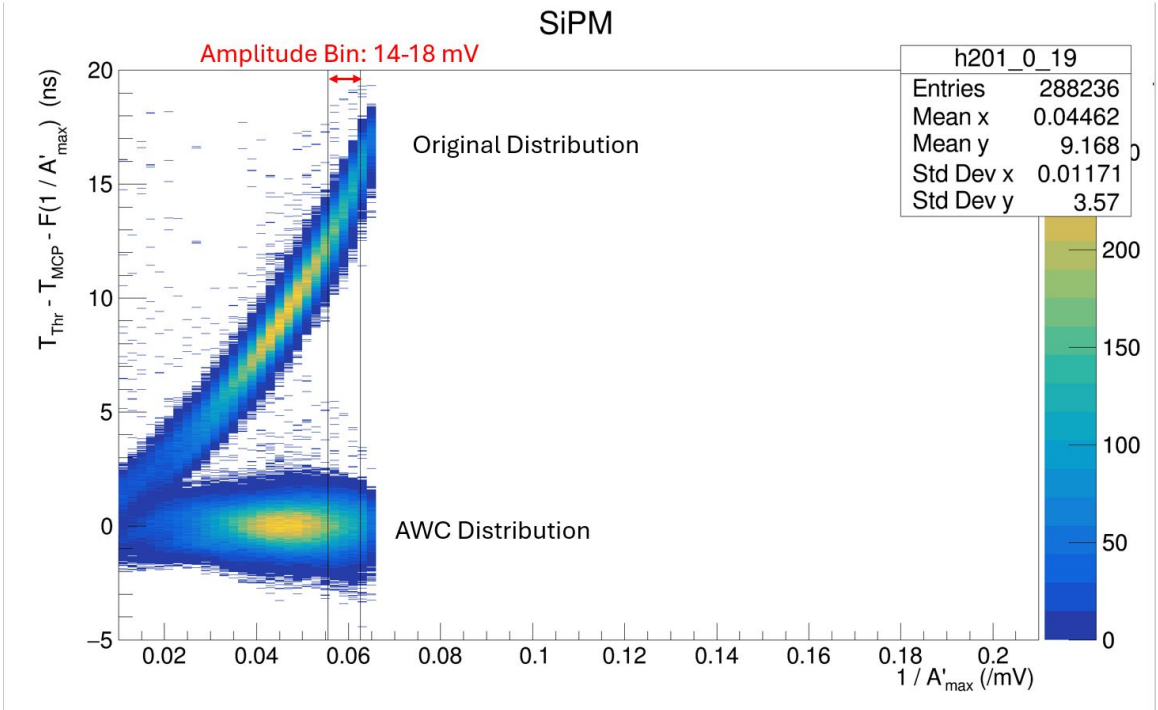

Figure 2.12: Superimposed are the same distributions before and after amplitude walk correction. Arcing upwards is the original distribution for channel 0 at a high threshold of about 200 mV*ns. Beneath the original distribution lies the corrected version, which has timing nicely distributed about 0 ns. Two black lines outline the amplitude bin from which projections in (Figure 2.13) are retrieved (unfiltered $PbWO_4$).

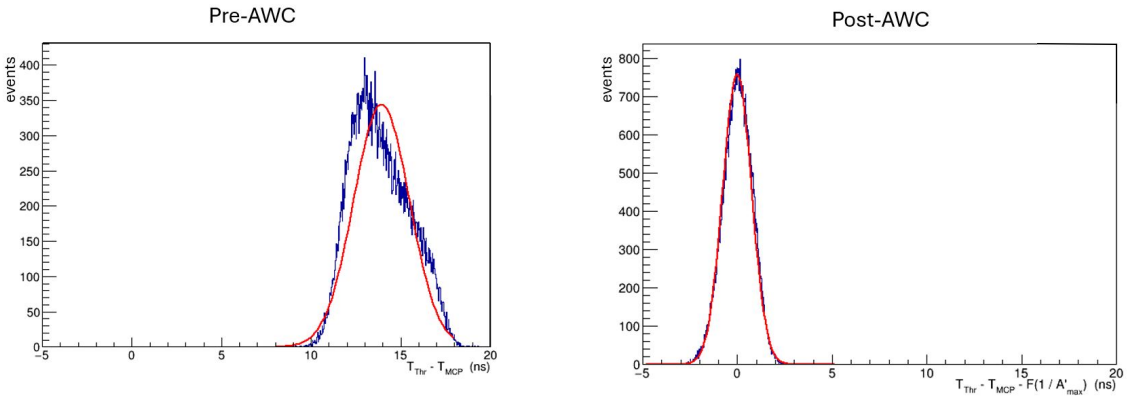

Figure 2.13: Seen in (Figure 2.12) is the same distribution before and after amplitude walk corrections. The projection (left) from the original distribution in the 16 mV window of events is noticeably wider and asymmetric compared to the same projection for the corrected data (right) (unfiltered $PbWO_4$).

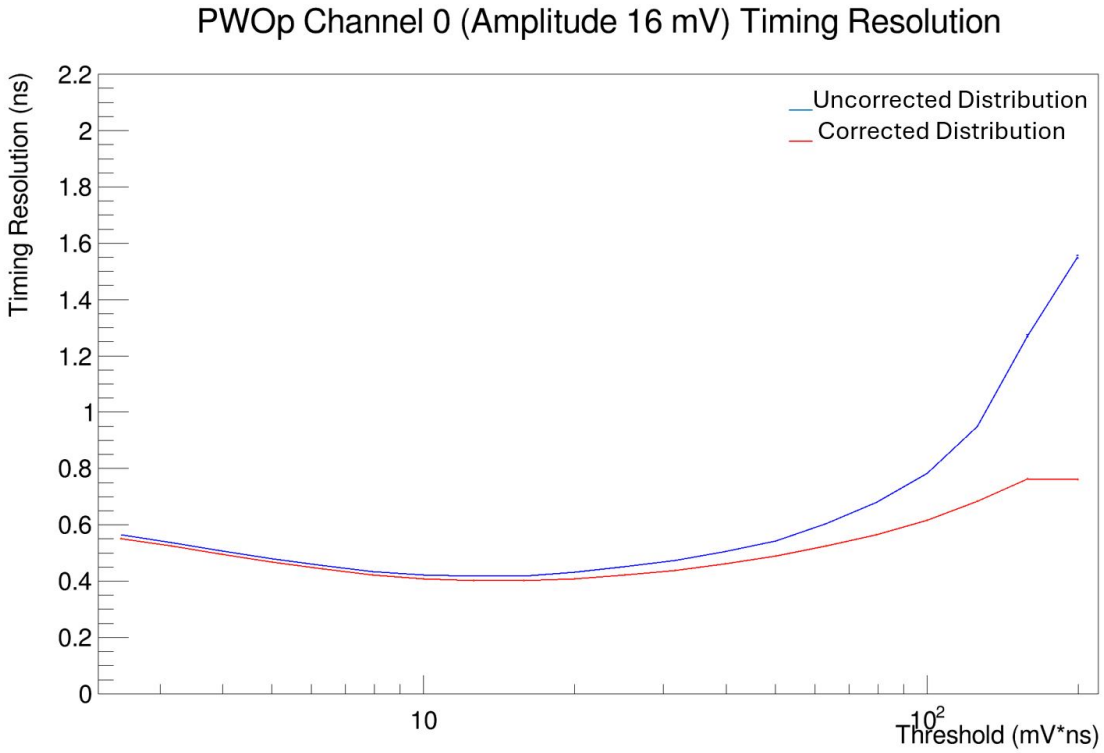

Figure 2.14: Comparison of the timing resolution for channel 0 in the 16 mV bin of amplitude before and after correction. It is noted that the corrected distribution tends to diverge at high thresholds where the dependence on amplitude was more prominent (unfiltered $PbWO_4$).

2.3.2 Channel Combinations

With the nonuniform dependence of timing on amplitude removed, the opportunity to improve timing resolution presents itself once again. By averaging the readings from multiple channels for a single event, one could expect the resolution to improve with statistical power. Consider the proof of concept in which the backend channels of unfiltered PbWO_4 are averaged together one channel at a time (Figure 2.15). The distributions become noticeably more narrow and the resolution improves. Prior to any averaging process, channel 0 at the threshold 10 mV*ns achieves a timing resolution of 420.17 ± 0.68 ps. Once channel 0 is averaged with channel 1, the resolution becomes 289.19 ± 0.47 ps. Averaging in channel 2 yields 263.92 ± 0.43 ps and lastly, including channel 3 finds 226.42 ± 0.37 ps. By averaging these channels together there is a 46% improvement to timing resolution. The same exercise can be carried out for frontend channels on unfiltered PbWO_4 (Figure 2.16).

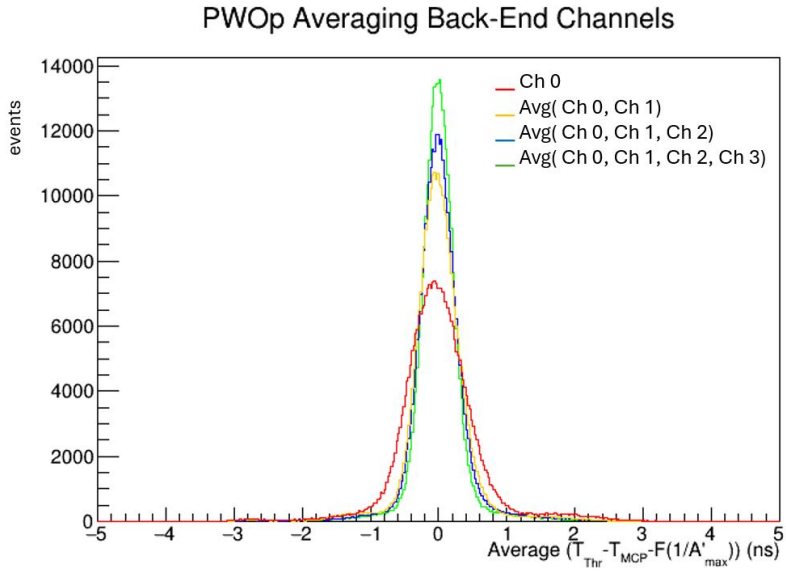

Figure 2.15: Comparing the timing resolution for each channel compounded in the averaging of event signals. Results in a 46% improvement to resolution.

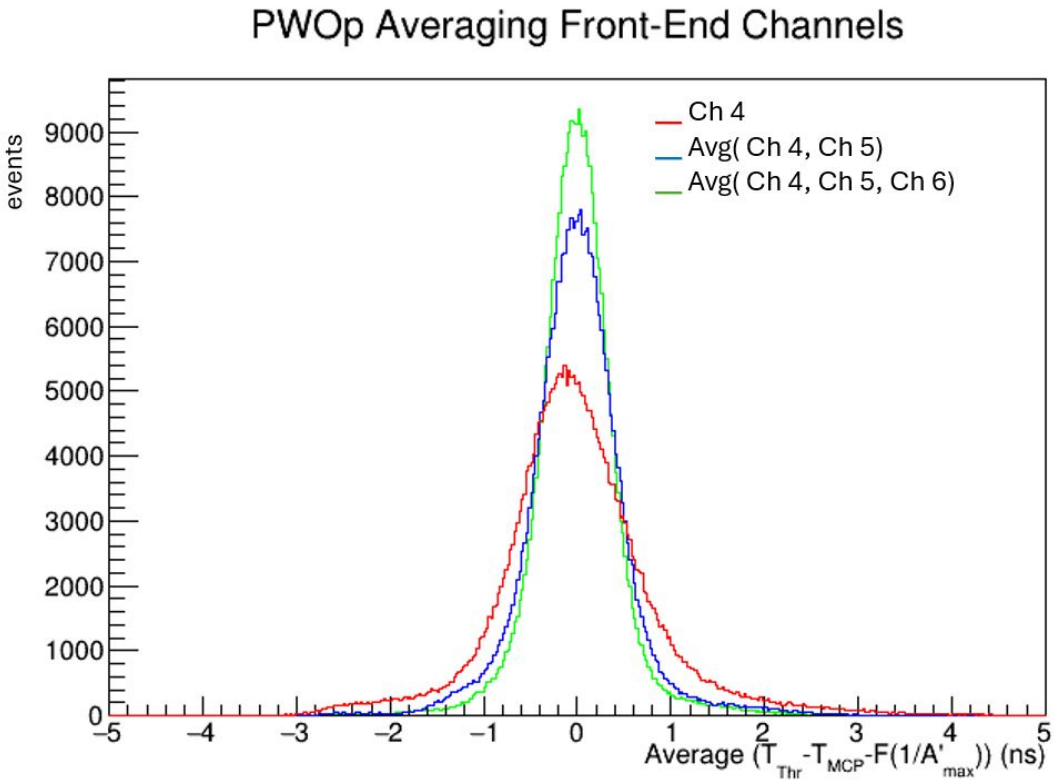

Figure 2.16: Comparing the timing resolution for each channel compounded in the averaging of event signals. One finds that channel 4 at a threshold of 10 mV*ns will attain a resolution of 651.1 ± 1.3 ps. Once channel 4 is averaged with channel 5; 427.98 ± 0.76 ps. Lastly, using channel 6 in the average yields a resolution of 351.36 ± 0.60 ps and thus improves resolution by 46%. This process shows promise for increasing resolution in future testbeams.

2.4 Timing Analysis of Filtered PbWO_4

When the interference filter is introduced between the back face of the crystal and channel 0-3 SiPMs, the process of measuring timing resolution becomes difficult. This was first noted when evaluating the timing resolution for channel 0 around 16 mV (Figure 2.17). The disjunction in the filtered timing resolution curve can be

attributed to the presence of two distinct peaks in the distribution shown in (Figure 2.18). The two unique regimes, separated in time and amplitude, become prevalent at low threshold voltages and only affect the backend channels in the filtered data set. There is no sign of similar behavior in frontend channels of the filtered data set, nor does there seem to be any indication of these peaks in unfiltered data. In early studies of the BGO crystal, one can find the same structure when a filter is applied (Figure 2.19). Overall, the impact of the double-peak structure is inflation of timing resolution on backend channels in amplitudes where the peaks overlap (Figure 2.17).

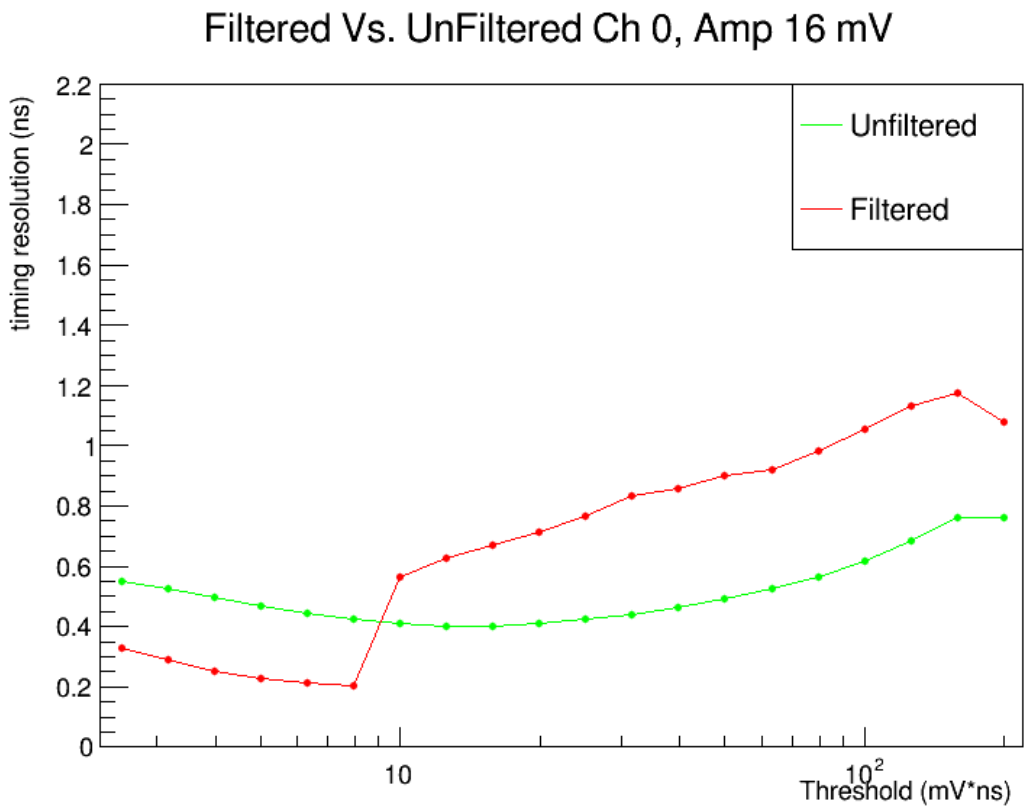

Figure 2.17: Comparing the timing resolution results (with corrections) between the filtered and unfiltered data for $PbWO_4$ in channel 0 for amplitudes 14-18 mV. It can be seen the backend channels experience dramatic changes in resolution. The locations where these spikes occur are the amplitude bins in which both peaks overlap.

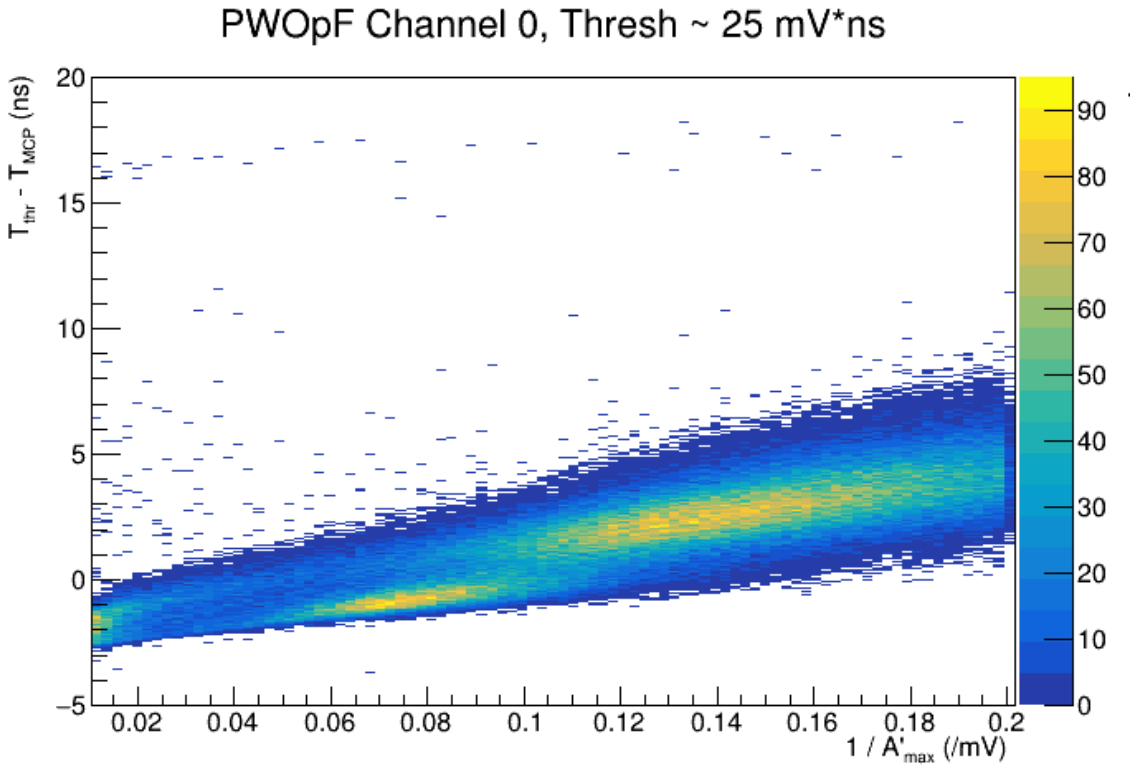

Figure 2.18: Timing distribution (uncorrected) for filtered channel 0 in PbWO_4. The double peak structure which is responsible for trends such as that seen in (Figure 2.17).

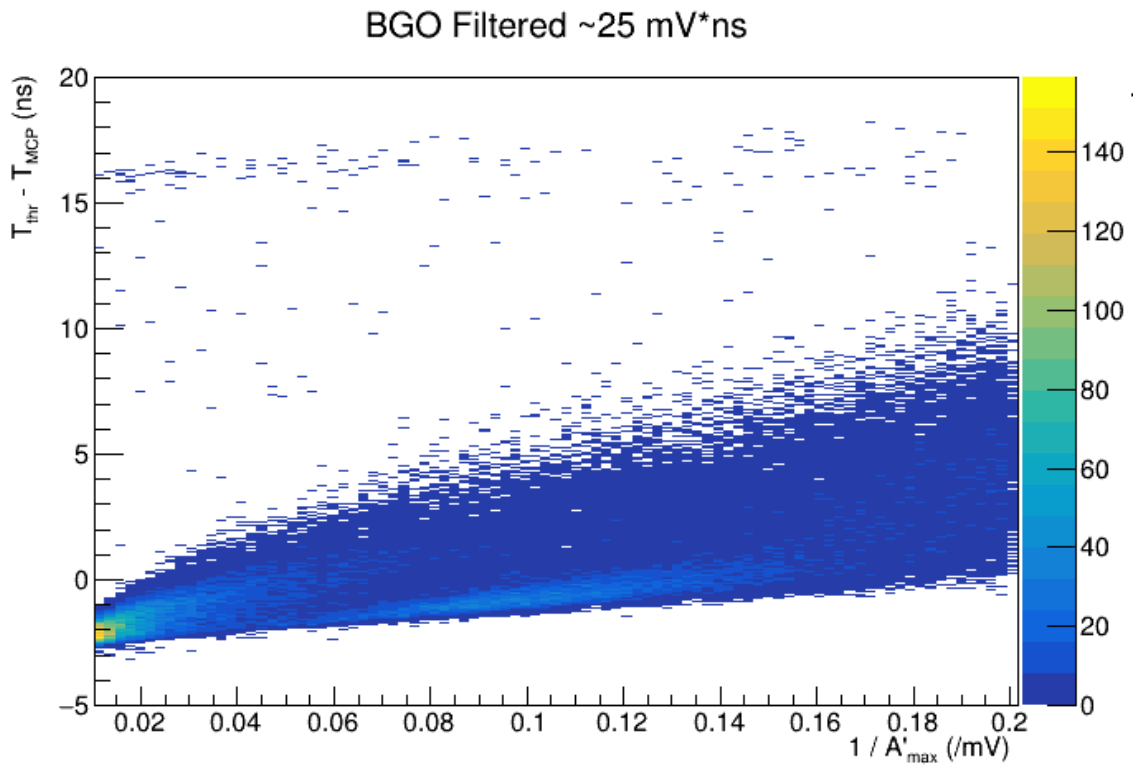

Figure 2.19: Timing distribution for BGO crystal data (uncorrected) where a similar double peak structure is seen (filtered BGO, parallel to beamline).

2.4.1 Double-Peak Structure

Studies into the origin of the double peak structure began with investigation of the positional dependence of the events belonging to each regime. The position of an event track in the plane of a given SiPM face is described with respect to the center of the SiPM (Figure 2.20). Initial results were suggestive that around 8 mm from the center of a given SiPM, the regimes were split (Figure 2.21). Consistently, it can be shown that the average pulses of events belonging to R $<$ 8 mm from the SiPM center will produce pulses that arrive earlier than those striking R $>$ 8 mm (Figure 2.22). This positional dependence and pulse shape (Figure 2.22) is indicative of a larger

ratio of Cherenkov radiation to scintillation signal in one of the peaks. This is once again true of both PbWO_4 and BGO (Figures 2.23 and 2.24). Such an observation is expected as the backend channels were outfitted with a filter intending to remove contaminating scintillation from Cherenkov signals, but it seems that a significant scintillation component is still present.

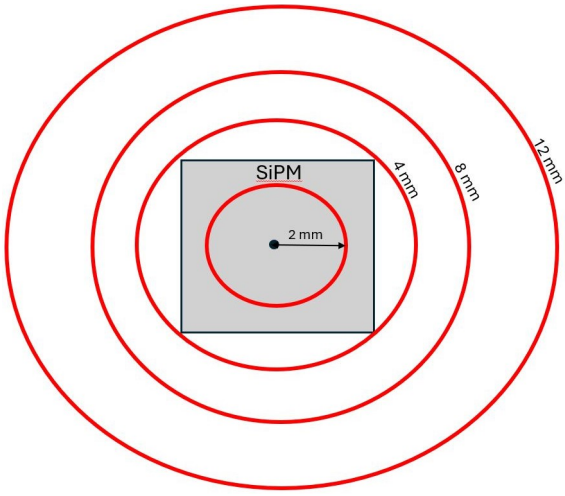

Figure 2.20: Pictured center is an arbitrary SiPM, and from it, several radial distances are specified. In studies of the double peak, the regions of interest observed were: R $>$ 2 mm, 2 mm $<$ R $<$ 4 mm, 4 mm $<$ R $<$ 8 mm, 8 mm $<$ R $<$ 12 mm and R $>$ 12 mm. It is also noted that with a square dimension of 6 x 6 mm, the SiPM can be approximated as a disc of $\sqrt{18}$ mm radius. This approximation will serve to define events that hit the SiPM or miss the SiPM later.

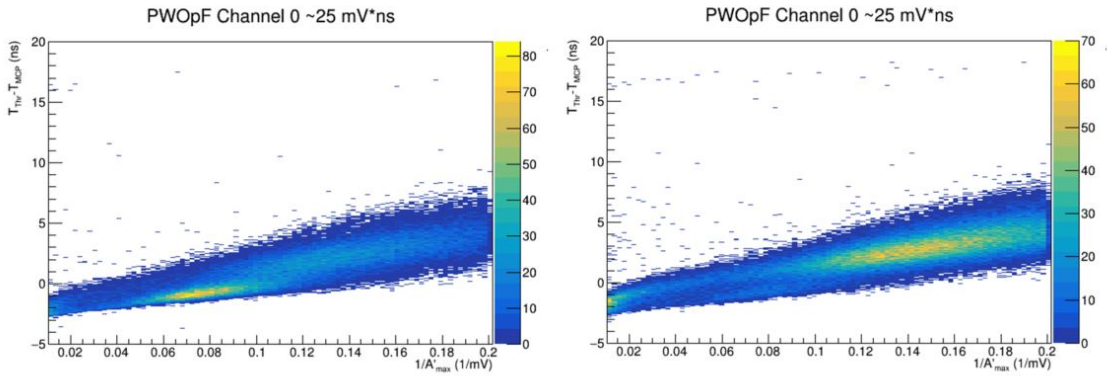

Figure 2.21: Informed by studies on the events in each of the 5 rings, specified in (Figure 2.20), it was found that the two prominent peaks in backend channels were divided by the radial boundary of 8 mm. Shown (left), the distribution of events with distance R $<$ 8 mm from the center of the channel 0 SiPM. Those events that have tracks R $>$ 8 mm from the center of the SiPM produce the other peak seen (right) (PbWO_4 Filtered).

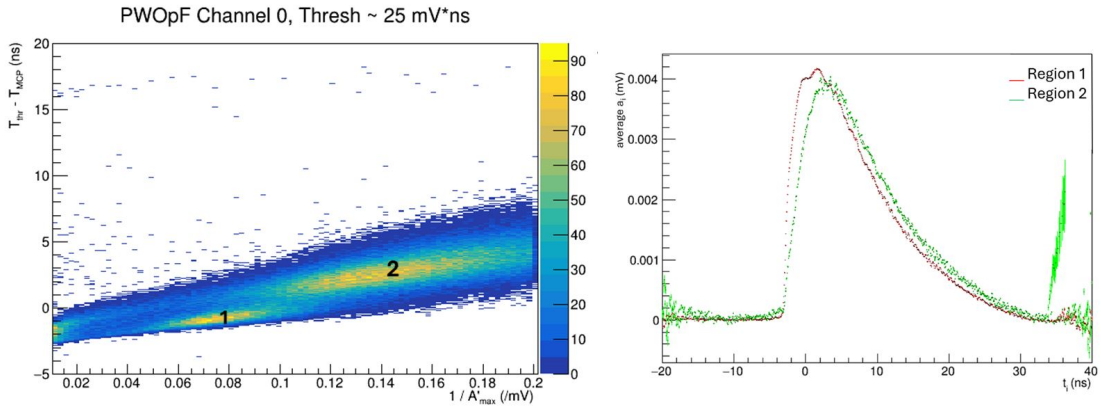

Figure 2.22: A graph of the average wave forms in the center of each peak of the channel 0 SiPM at a threshold of 25 mV*ns. The lower left distribution (denoted "1") produces a noticeably more prompt signal than that of the other peak (both signals normalized to their respective integrals from [-5,20] ns).

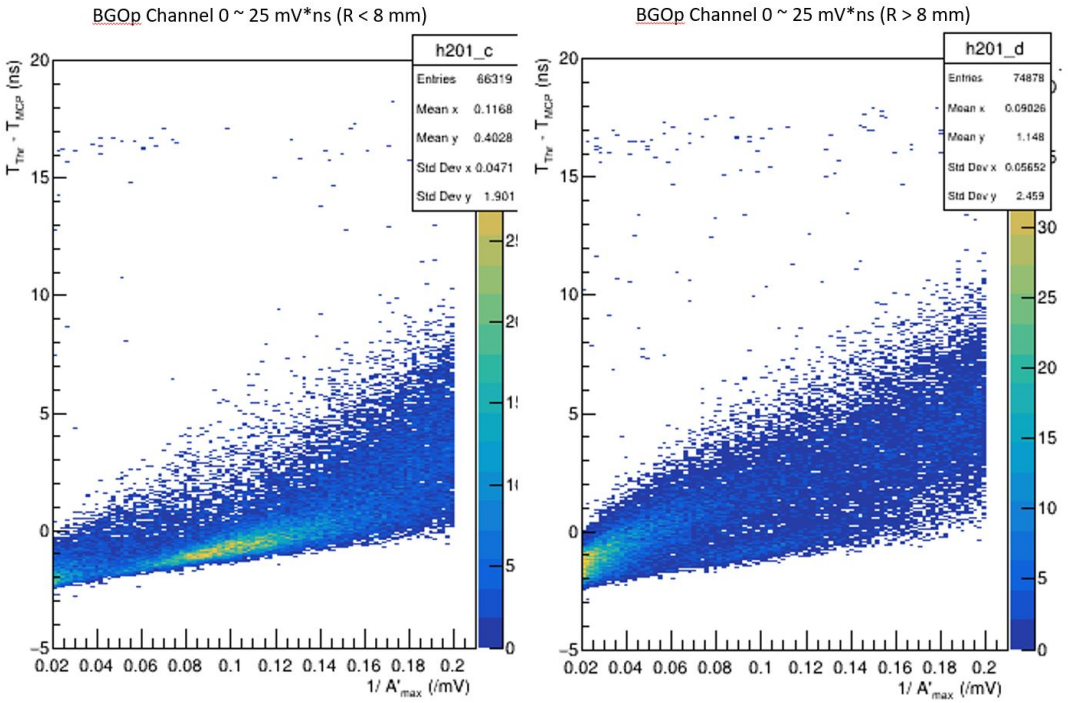

Figure 2.23: Much like $PbWO_4$, BGO tends to have more than one peak in the filtered backend channels. Here, the distribution of channel 0 at a threshold of 25 mV*ns can be seen divided by the same 8 mm cut (BGO filtered, parallel orientation).

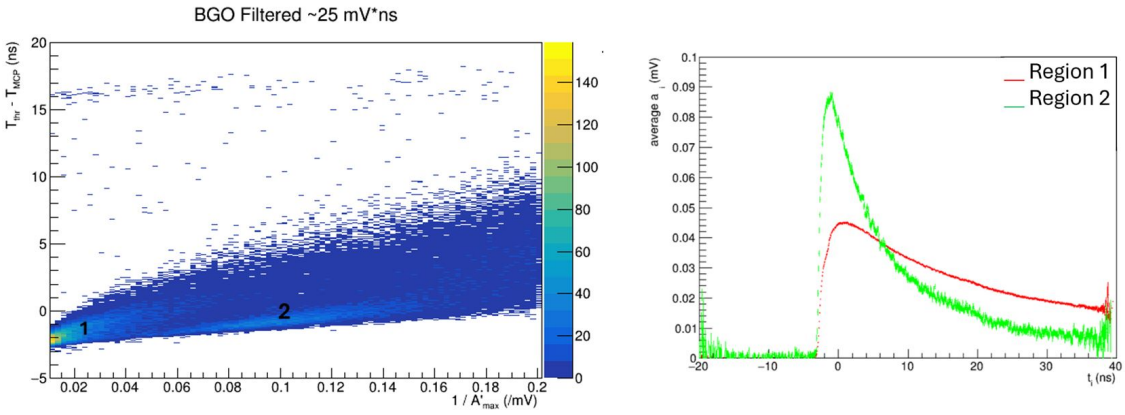

Figure 2.24: In much the same way as $PbWO_4$, observing average wave forms originating from the distinct peaks yields two different pulses. The green pulse belonging to the narrow peak from about 6 to 16 mV has a much steeper rising edge than that of the other peak. (BGO filtered, parallel orientation, both signals normalized to their respective integrals from [-5,20] ns).

Studies of position dependence did not end with the double peak structure. It was also observed that events originating from proton tracks striking a given SiPM directly (within a radial $\sqrt{18}$ mm distance from the center of a SiPM) produced a better timing resolution (Figures 2.25 and 2.26). Considering the case of unfiltered PbWO_4 and evaluating channel 4 at a threshold of 8 mV*ns, it is seen that the overall distribution has a timing of 651.1 ± 1.3 ps. The events that miss have a resolution of 678.6 ± 1.4 ps, while those that strike the SiPM directly have a resolution of 332.5 ± 2.1 ps. There is a 69% difference between the hit and miss resolutions, and obviously, the events that miss degrade resolution. This suggests that future accommodations can be made in the calorimeter to further enhance timing resolution, a possibility discussed in conclusions (Chapter 3).

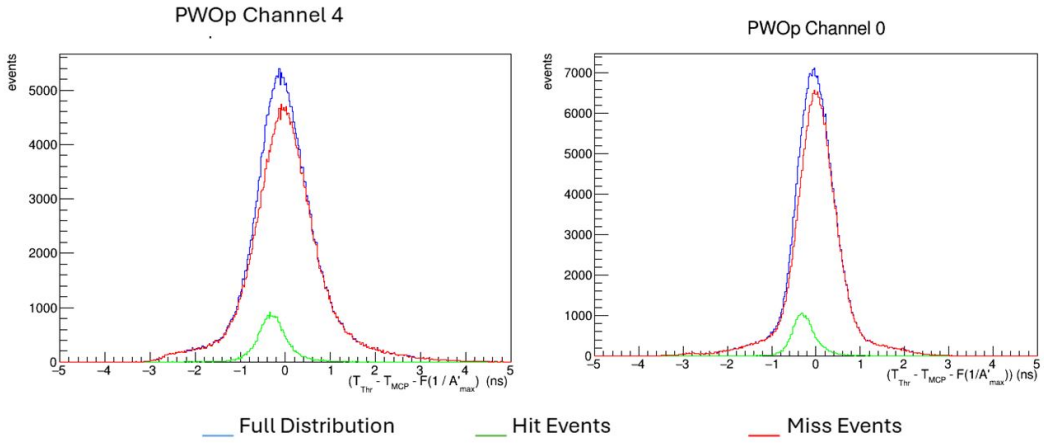

Figure 2.25: Unfiltered PbWO_4: Cutting on events that either strike the SiPM directly (R < $\sqrt{18}$ mm) or miss the SiPM (R > $\sqrt{18}$ mm) reveals the best resolution is found for those that strike the SiPM. Seen (left) is the unfiltered channel 4 and on the (right) a backend counterpart (channel 0). This reveals this trend is true on both crystal faces.

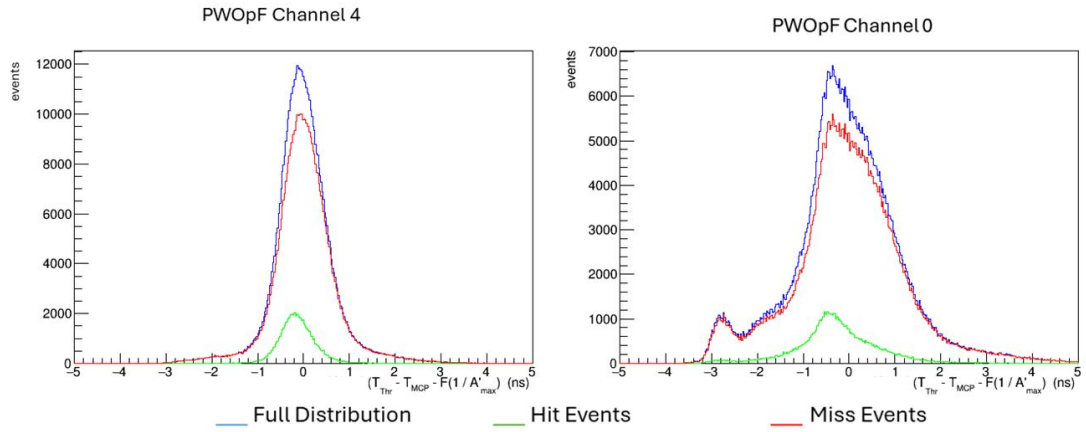

Figure 2.26: Filtered $PbWO_4$: Cutting on events that either strike the SiPM directly ($R < \sqrt{18}$ mm) or miss the SiPM ($R > \sqrt{18}$ mm) reveals the best resolution is found for those that strike the SiPM. Here, channel 4 is shown again as well as channel 0 which is noticeably sensitive to the double peak. Since it was found that the peaks are separated by the radial cut of 8 mm, the "hit" condition is well within the single peak regime such that it does not experience a large asymmetry as the full set of events does. Regardless, the improvement is still true with or without the filter enabled.

2.5 Discussion of Results

With amplitude walk corrections implemented, the timing resolution results can be presented (see Appendix A for bulk data). The data is organized by the signal amplitude window analyzed and the channel from which the signal was read (Channel 0-6) (Figure 2.27).

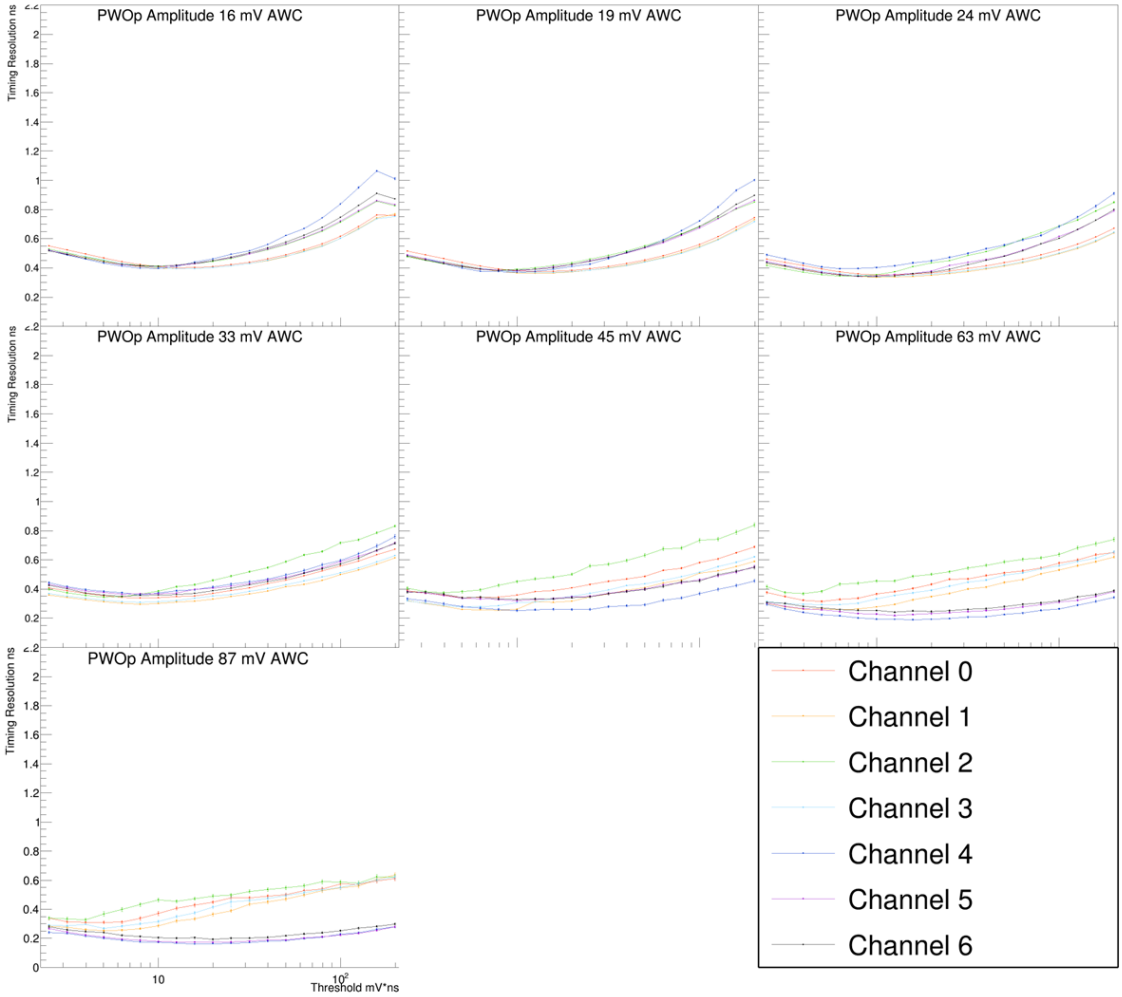

Figure 2.27: Collection of amplitude walk corrected timing resolution curves for $PbWO_4$, probing different amplitude ranges for each channel. On the x axis lies the threshold used to designate the timestamp T_{Thr} of an integrated event waveform. It can immediately be seen that channels on the backend (0-3) tend to behave similarly as do frontend channels (4,5,6). It can also be seen that as amplitude increases, the timing resolution improves. The entirety of the data is provided in (Appendix A).

Some noticeable features are easily picked out. Firstly, observing the behavior across channels for any given amplitude, the channels belonging to the backend behave similarly[3], and separately, the frontend channels exhibit their own group behavior.

[3]With the exception of unfiltered channel 2, which tends to have worse resolution consistently.

These diverging behaviors are exposed at high thresholds and high amplitudes (Figure 2.27). Further, it can be observed (Figures 2.28 - 2.31) that for a given channel and threshold, there is improved timing resolution with increasing amplitude as expected due to increased photostatistics. This observation holds at low thresholds, where it is found the best timing resolution usually occurs, and holds for both filtered and unfiltered data.

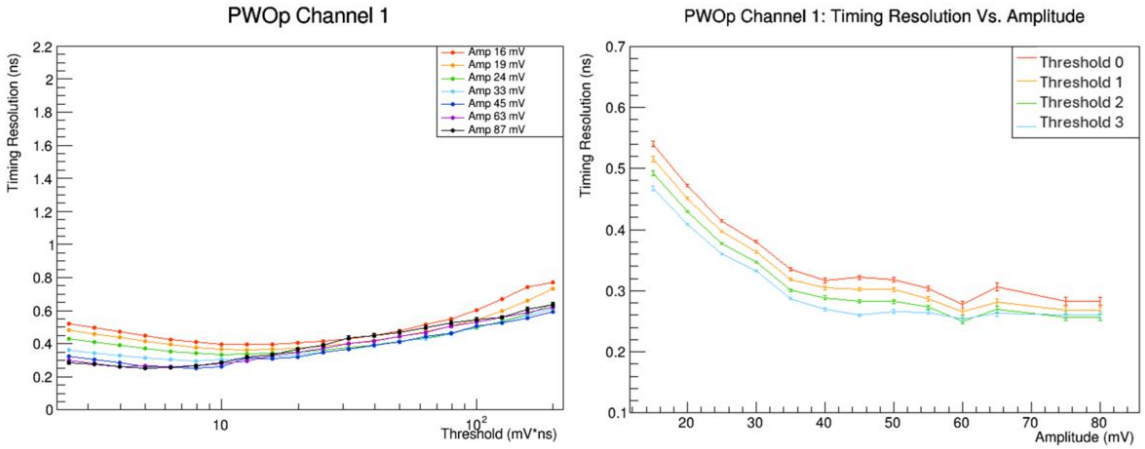

Figure 2.28: Timing resolution for channel 1 in unfiltered $PbWO_4$ (left). It can be seen, that at low thresholds, the increasing amplitude improves resolution. To further support this point, shown (right), the timing resolution versus amplitude for the first 4 thresholds of channel 1 are provided.

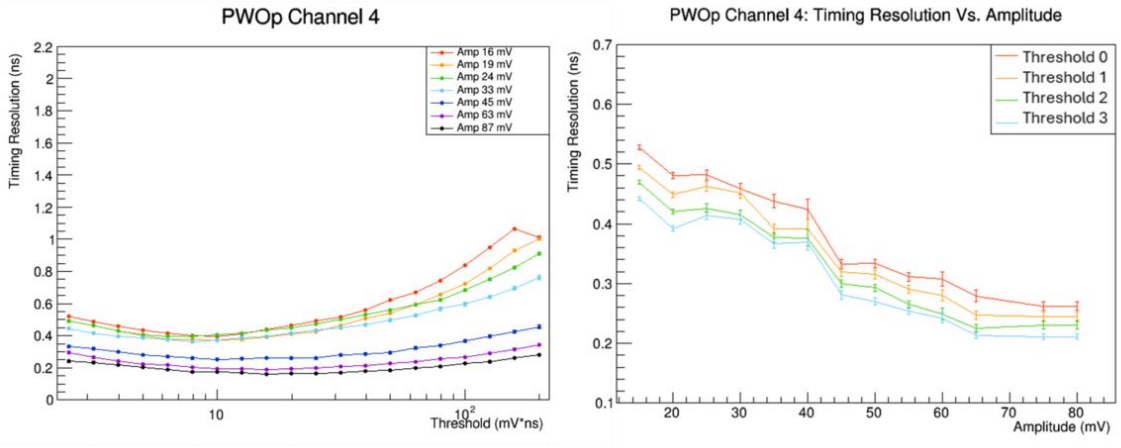

Figure 2.29: Timing resolution for channel 4 in unfiltered $PbWO_4$ (left). Frontend channel resolution improves with amplitude at most thresholds unlike backend channels. Shown (right), the timing resolution versus amplitude for the first 4 thresholds of channel 4 are provided.

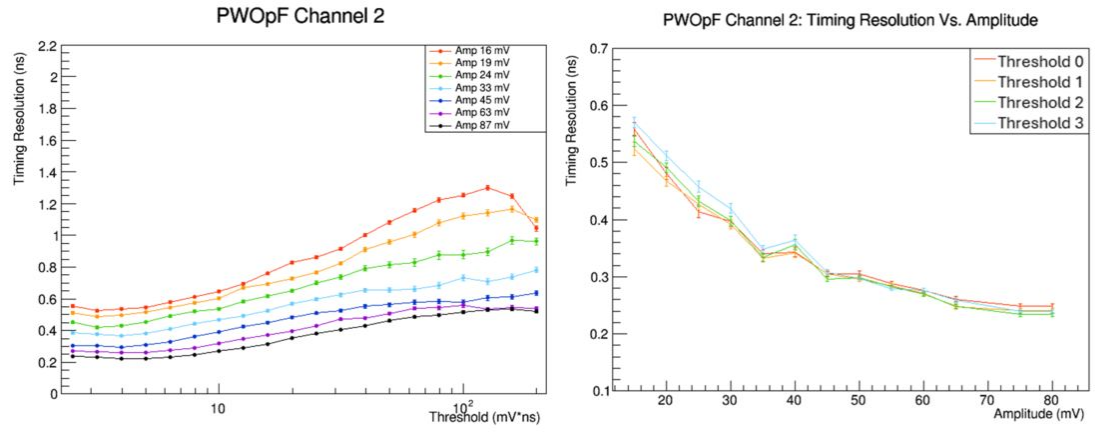

Figure 2.30: Timing resolution for channel 2 in filtered $PbWO_4$ (left). The resolution dependence at constant thresholds can be seen (right) to follow the same trend as the rest of the data.

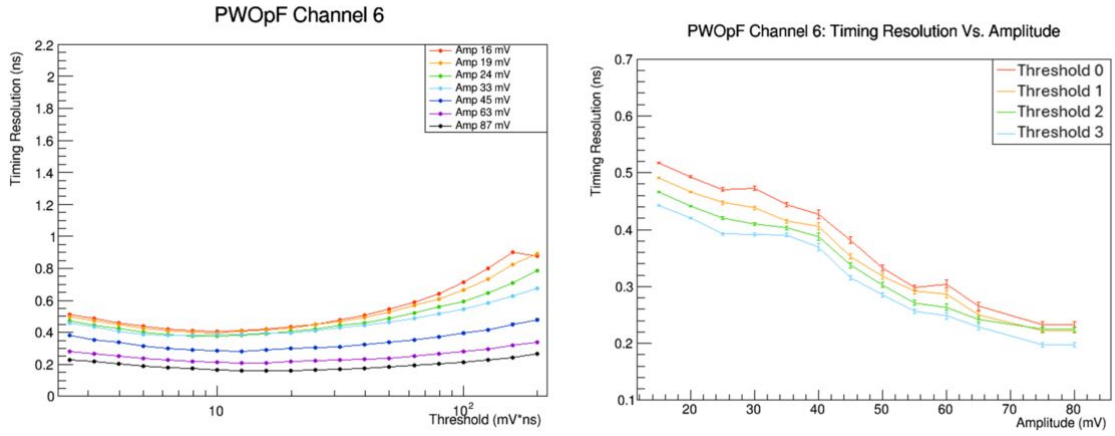

Figure 2.31: Timing resolution for channel 6 in filtered $PbWO_4$ (left). The resolution dependence at constant thresholds can be seen (right) to follow the same trend as the rest of the data.

Closer inspection will also reveal that, for unfiltered data, there tends to be better performance of backend channels for low amplitudes (Figure 2.32). Around 45 mV the best resolution is instead found in frontend channels. Conversely, the best resolution in filtered data rests with backend channels up until 24 mV, at which point frontend channels are more suitable (Figure 2.33). Across both data sets, it's observed the best resolution is achieved within the first 16 mV*ns[4].

[4]With exception of filtered data at 86 mV (±2 mV), achieving the best resolution at 19.95 mV*ns.

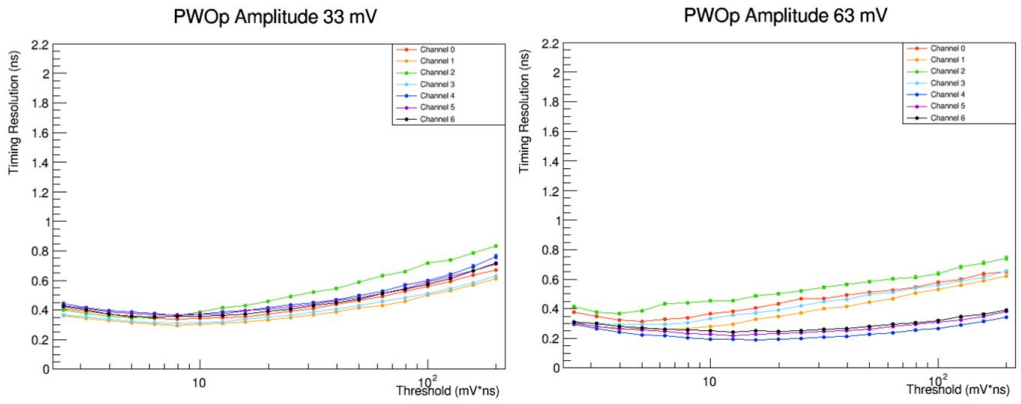

Figure 2.32: (Unfiltered $PbWO_4$) As amplitude rises, a steady progression of frontend channels overtaking backend channels in resolution can be seen. Here, it can also be seen, that the grouping behavior (frontend Vs. backend) diverges at high amplitudes.

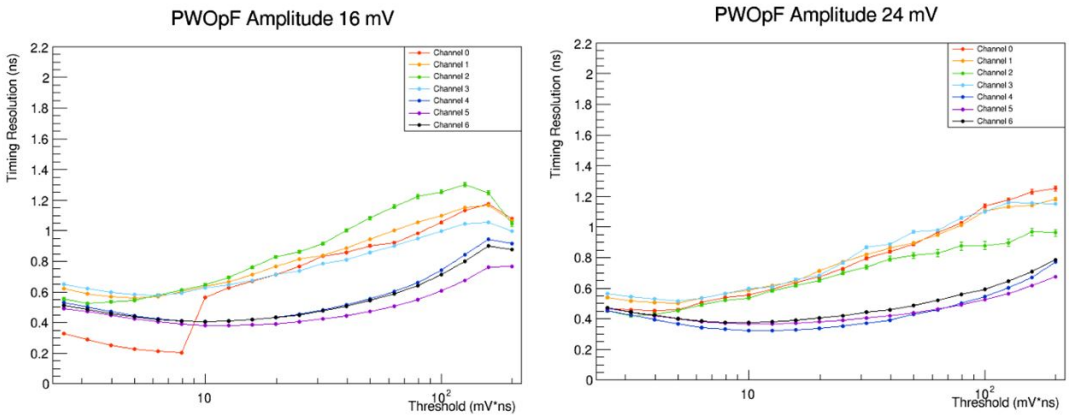

Figure 2.33: (Filtered $PbWO_4$) The frontend channels surpass the resolution of the backend channels sooner than in unfiltered data (around 24 mV).

The best resolution across all the unfiltered data is found in channel 4 for the 85 mV – 89 mV window (161.6 $\pm$ 3.6 picoseconds). The minimum for channel 4 around 87 mV, in the filtered dataset, (172.0 $\pm$ 3.0 ps) is 2.2σ from its unfiltered counterpart. The Filtered data sees a better resolution at the same amplitude window, but in channel 6 (158.0 $\pm$ 2.5 picoseconds), 6.2σ from that of channel 6 around 87 mV in the unfiltered

data (193.0 ± 5.1 ps). The two minima from each data set are only 0.82σ apart.

Generally, there doesn't appear to be a consistent trend between the filtered and unfiltered datasets across all channels. frontend channels are expected to be less sensitive to the presence of the filter on the back face of the crystal. While the timing resolution trends for frontend channels are not dissimilar, when the filter is introduced there are slight variations between the two (Figure 2.34) that could indicate an unexplained effect. Alternatively, backend channels tend to experience non-comparable trends once the filter is introduced (Figure 2.35). The accuracy of the filtered results are questionable due to the presence of the double-peak structure inflating resolutions.

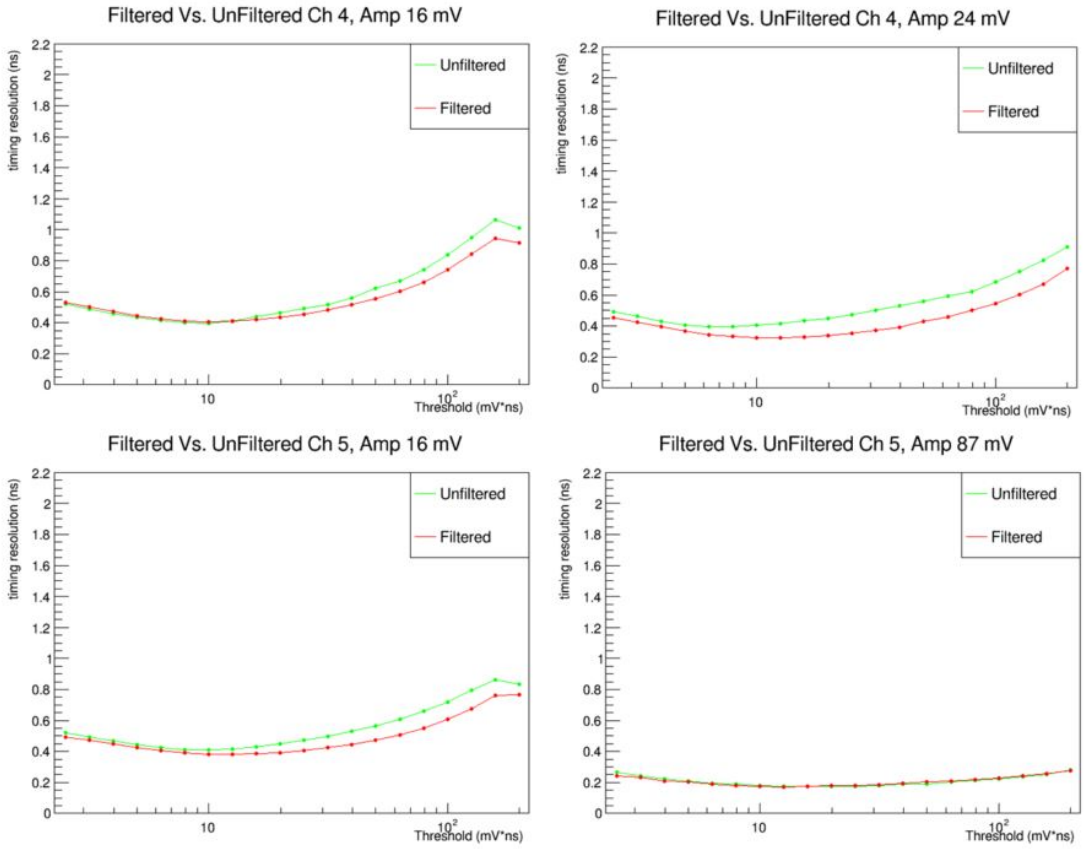

Figure 2.34: Comparison of timing resolution for frontend channels when the interference filter is applied between the back face of the crystal and the backend SiPMs. The filter appears to have little effect.

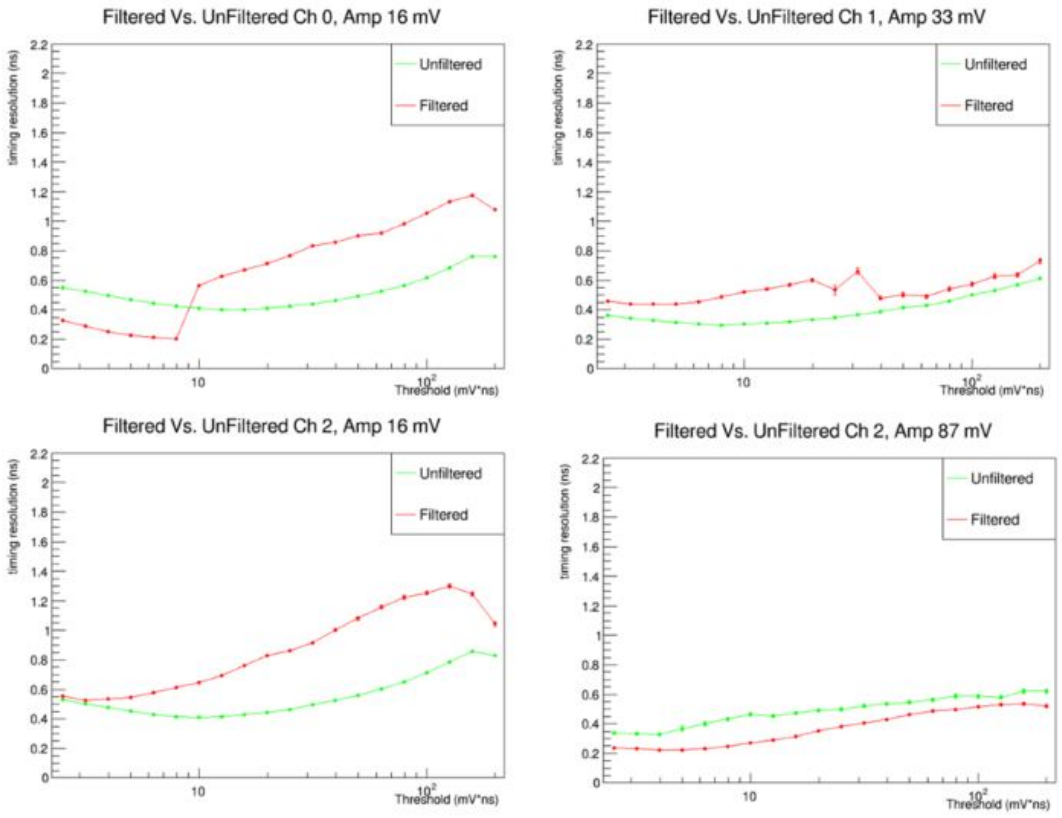

Figure 2.35: Behavior of backend channels in $PbWO_4$ before and after the use of an interference filter. The filter tends to reveal a double-peak structure, which broadens timing distributions in amplitude regions between these two peaks.

Since it is known that the best resolutions are often found for low thresholds, observing the difference between filtered and unfiltered data at fixed thresholds may be more telling. It can be seen, that channels 1, 3, 4, and 5 typically offer best resolution when unfiltered at low thresholds (Figures 2.36 and 2.37). Channels 0 and 2 are understandably difficult to profile due to their high sensitivity to the double-peak, leaving filtered data sporadic (Figure 2.38). Channel 6 has conflicting behavior, where low amplitudes will grant unfiltered data better resolution, but around 45 mV, a switch is made in preference to filtered data (Figure 2.39).

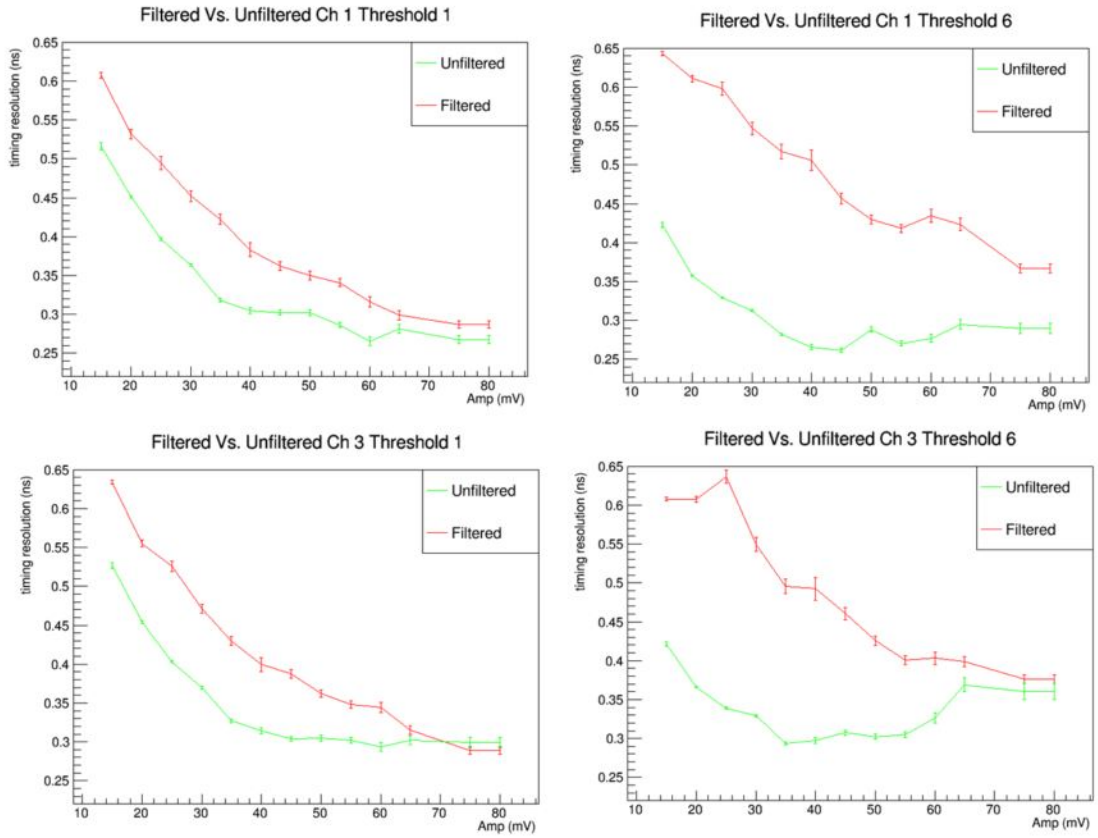

Figure 2.36: A comparison of timing resolution in backend channels and it's dependence on amplitude at low thresholds, with and without a filter applied. It can be noted that, while both improve with amplitude, unfiltered channels tend to have better resolution.

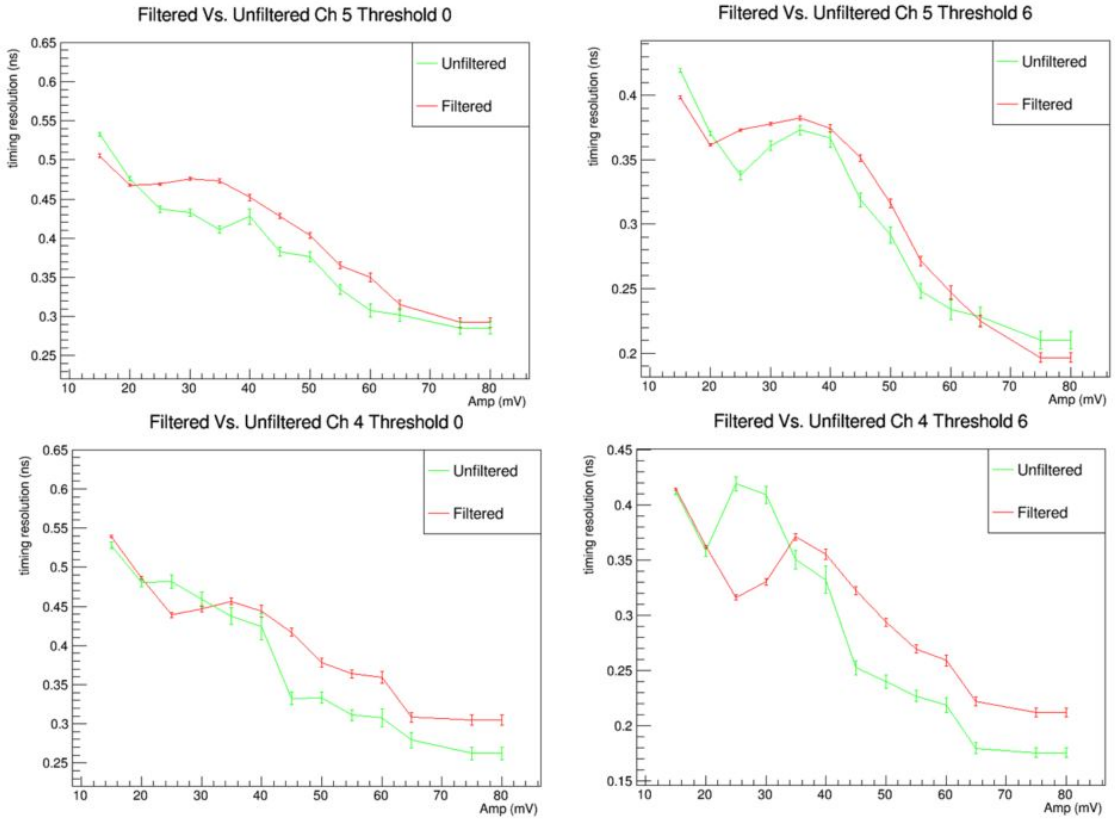

Figure 2.37: Comparing the amplitude dependence of timing resolution for frontend channels at constant threshold, with and without a filter. The trends are similar and seem to intersect at low amplitudes. For the majority of amplitudes, unfiltered data tends to have better resolution.

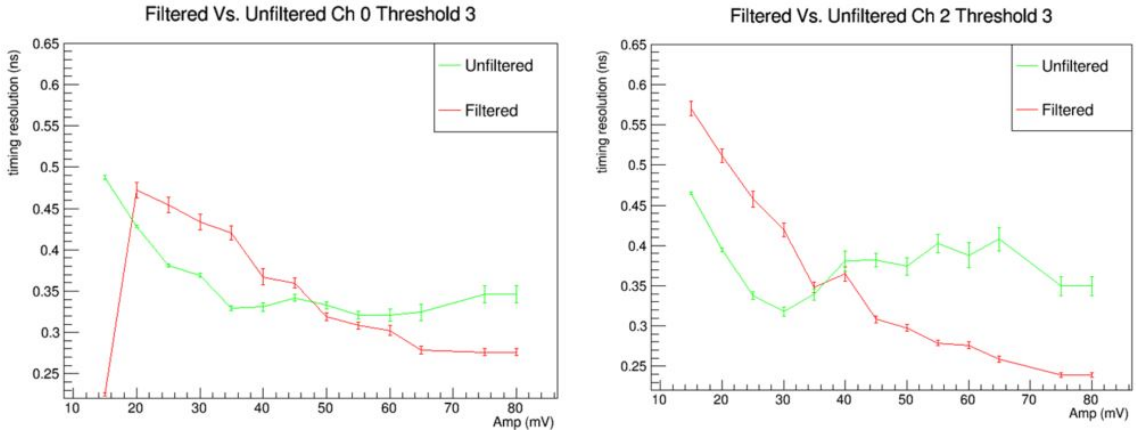

Figure 2.38: Channel 0 and Channel 2 on the backend are difficult to characterize in terms of resolution, with and without a filter. The behavior of the channels is compromised by the double-peak structure, and the resulting resolution is poorly behaved. Cycling through the first 10 mV*ns of threshold voltages reveals no clear pattern.

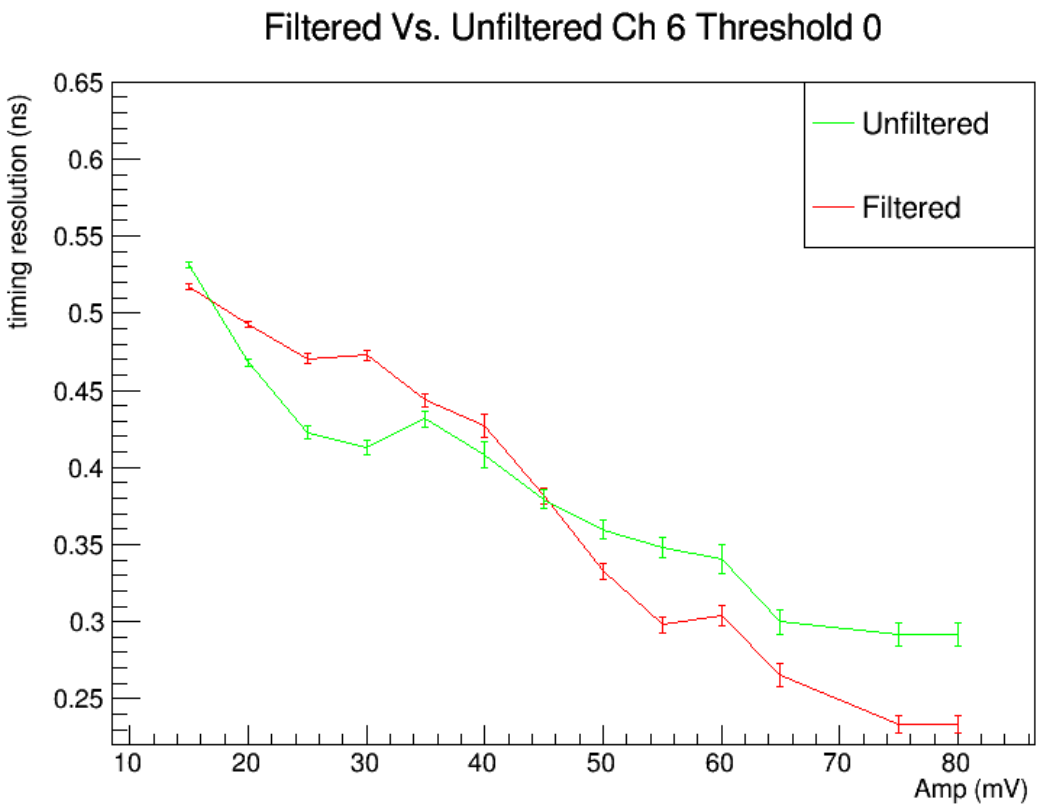

Figure 2.39: Channel 6 behaves differently than its frontend companions (4 and 5), as it consistently intersects around 45 mV and begins to improve resolution more in the filtered data than the unfiltered.

Chapter 3

Conclusions

With the goal of DR in mind, it is essential to separate the Cherenkov light from that of scintillation. While the spectral filters used managed to contribute to this separation, there still exists signal in the filtered backend channels which contaminates data. This contamination is evidenced by the strong positional dependence of the signals and their apparent differences in pulse shapes, as the Cherenkov is more prompt. This contamination contributes to a worsening of the timing resolution results in backend channels and requires special attention. The method of calculation for timing resolution may need be reconsidered for a method less sensitive to the contamination unlike the integral method used in this analysis. It may also be considered to use more aggressive techniques to further separate the Cherenkov from the scintillation. Such techniques, studied by the RD52 program (Section 1.4), would include taking advantage of the polarization of Cherenkov, its directionality, or the pulse shape analysis. The filter used (660 nm interference filter) could be speculated to contribute to the scintillation presence in the filtered backend channels because it is less effective for non-normal incidence of light. To further understand the effects of the filter, studies on the available BGO crystal may offer insight as the filter applied was an absorption filter. A careful evaluation of the systematic effects due to light coupling and transmission should be part of future work. Newer electronics and test beam infrastructure can increase the signal to noise ratio in the readout, improving

timing performance. Lastly, making measurements around or below a 100 ps level can be very challenging, a more detailed evaluation of our timing reference (the MCP) will clarify the size of the constant limiting factor in these studies.

Results of the analysis revealed a positive trend with increasing amplitude and that best results were consistently found for low thresholds under 16 mV*ns. It was also found that more often than not, the unfiltered data offered better resolution with some exceptions (Section 2.5). Also discovered was the relationship of resolution with track position. Results suggest that MiPs striking the SiPM directly offer best resolution. For this reason, it may be more advantageous to use crystals with smaller faces or larger area SiPMs to ensure more uniform response. In the same vein, application of amplitude walk corrections proved useful in improving the timing resolution noticeably. It was also found that averaging the readings offered up to 46% improvement in resolution. Perhaps, utilizing more readouts would be beneficial in the future. In the end, the best timing resolution measurement was yielded by channel 6 in the filtered $PbWO_4$ data set at a nominal amplitude of 87 mV and a threshold voltage of about 20 mV*ns (158.0 $\pm$ 2.5 picoseconds). These methods and results can be applied to future work on the CalVision calorimeter research and can contribute to studies on further improving the timing capabilities.

Bibliography

[1] Bonnie Fleming et al. "Basic Research Needs for High Energy Physics Detector Research and Development: Report of the Office of Science Workshop on Basic Research Needs for HEP Detector Research and Development: December 11-14, 2019". In: (Dec. 2019). DOI: 10.2172/1659761. URL: https://www.osti.gov/biblio/1659761.

[2] Sehwook Lee, Michele Livan, and Richard Wigmans. "Dual-readout calorimetry". In: *Reviews of Modern Physics* 90.2 (Apr. 2018). ISSN: 1539-0756. DOI: 10.1103/revmodphys.90.025002. URL: http://dx.doi.org/10.1103/RevModPhys.90.025002.

[3] S. Lee. "On the limits of the hadronic energy resolution of Calorimeters". In: *Journal Name* 1162.1 (2019), p. 012043. URL: https://iopscience.iop.org/article/10.1088/1742-6596/1162/1/012043/pdf.

[4] I. Pezzotti et al. *Dual-Readout Calorimetry for Future Experiments Probing Fundamental Physics*. 2022. arXiv: 2203.04312 [physics.ins-det]. URL: https://arxiv.org/abs/2203.04312.

[5] Vladimir Nagaslaev amd Alan Sill and Richard Wigmans. "Beam tests of a thin dual-readout calorimeter for detecting cosmic rays outside the Earth's atmosphere". In: *Nuclear Instruments and Methods in Physics Research A462 (2001) 411–425* (2000). URL: http://www.phys.ttu.edu/~dream/resources/publications/462_411.pdf.

[6] N. Akchurin et al. "Hadron and jet detection with a dual-readout calorimeter". In: *Nuclear Instruments and Methods in Physics Research A537 (2005) 537–*

561 (Sept. 2004). URL: http://www.phys.ttu.edu/~dream/resources/publications/1-s2.0-S0168900217305703-main.pdf.

[7] M.T. Lucchini et al. "New perspectives on segmented crystal calorimeters for future colliders". In: *Journal of Instrumentation* 15.11 (Nov. 2020), P11005–P11005. ISSN: 1748-0221. DOI: 10.1088/1748-0221/15/11/p11005. URL: http://dx.doi.org/10.1088/1748-0221/15/11/P11005.

[8] N. Akchurin et al. "Contributions of Cherenkov light to the signals from lead tungstate crystals". In: *Nuclear Instruments and Methods in Physics Research A582 (2007) 474–483* (2007). URL: http://www.phys.ttu.edu/~dream/resources/publications/582_474.pdf.

[9] Gabriella Gaudio and Richard Wigmans. *Dual-Readout Calorimetry for High-Quality Energy Measurements: Progress Report and Request for Allocation of Resources*. DREAM Collaboration (Cagliari - Cosenza - Iowa State - Pavia - Pisa - Roma I - Texas Tech), June 2011.

[10] Alexander Ledovskoy. *Analysis of CALVISION Test Beam at FNAL in April 2023*. Presentation. Private Communication. 2023.

Appendices

Appendix A

Appendix A: Timing Resolution Plots

In this section, the entirety of timing resolution plots are displayed (post-amplitude walk corrections). The first section provides the data from unfiltered $PbWO_4$ organized by amplitude such that each figure presents the trends of all channels across a single amplitude bin. The second section contains the same data reorganized by multiple amplitude trends for a single channel in each plot. Sections 3 and 4 mirror that of sections 1 and 2 except using the filtered $PbWO_4$ data set.

A.1 Section 1: Unfiltered PbWO_4 Timing Resolution by Amplitude

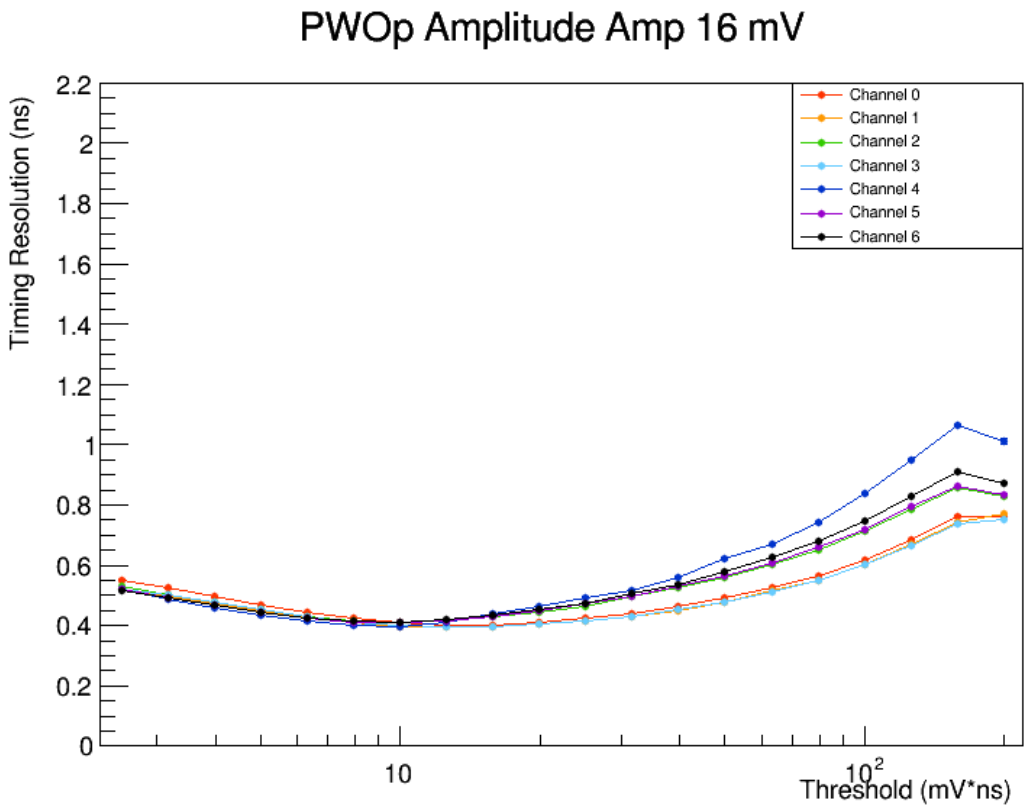

Figure A.1: Unfiltered PbWO_4 timing resolution vs. threshold voltage for all channels (14-18 mV in amplitude).

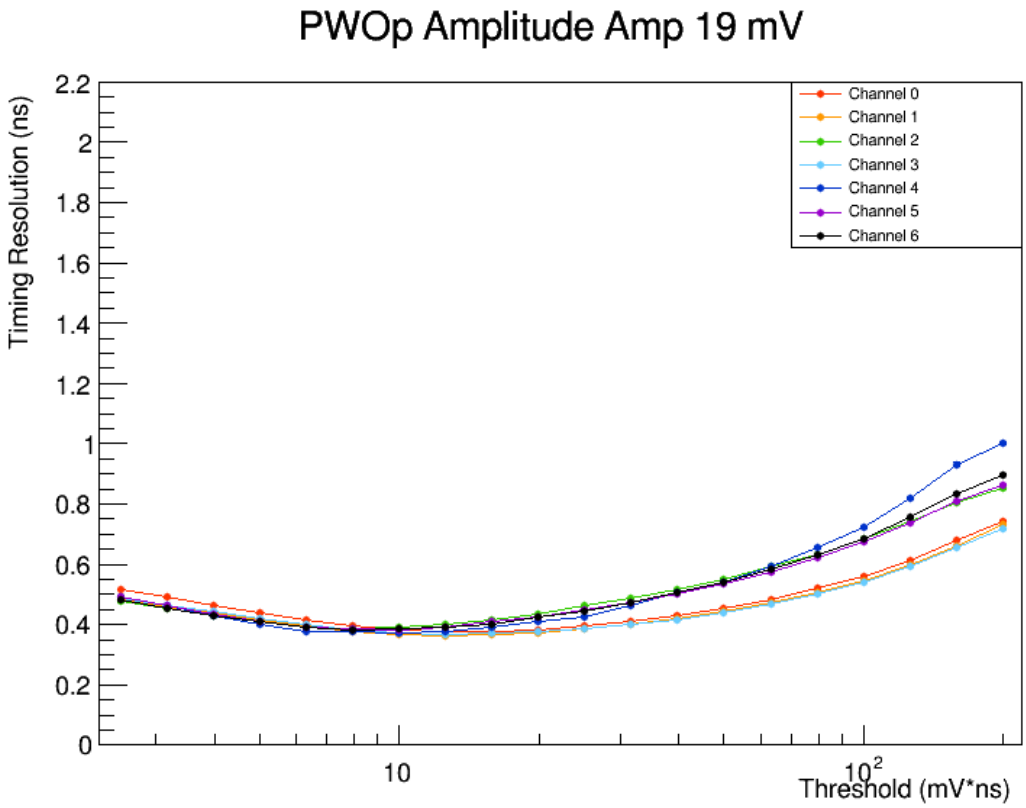

Figure A.2: Unfiltered $PbWO_4$ timing resolution vs. threshold voltage for all channels (17-21 mV in amplitude).

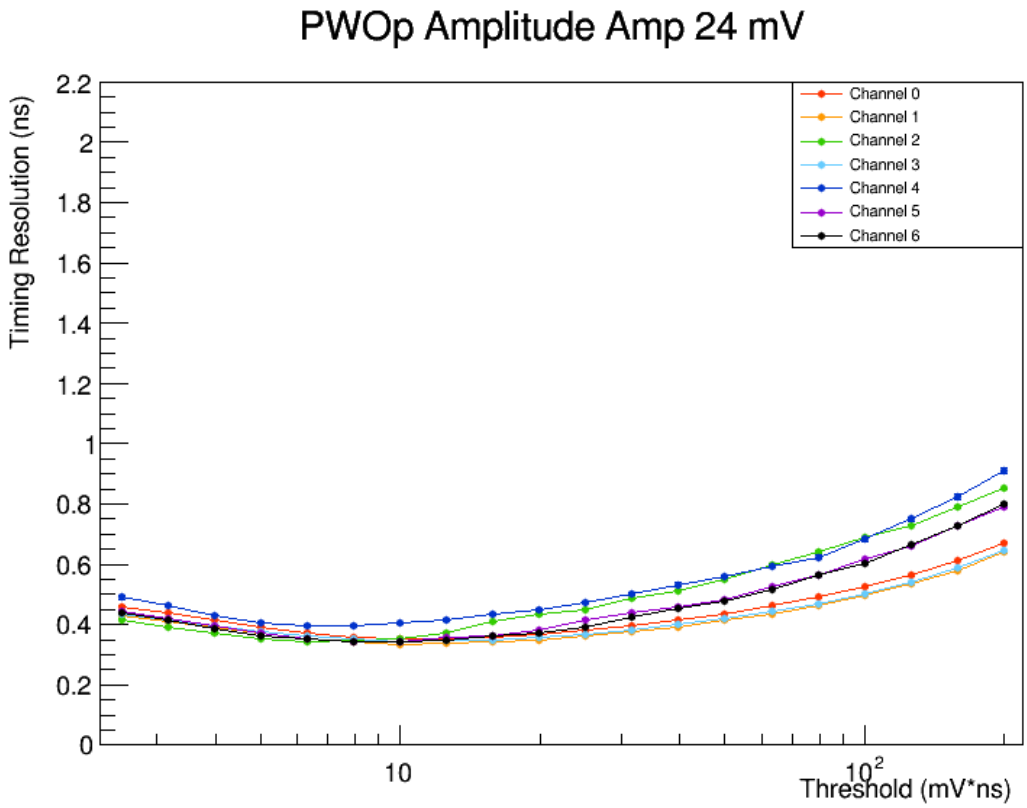

Figure A.3: Unfiltered $PbWO_4$ timing resolution vs. threshold voltage for all channels (22-26 mV in amplitude).

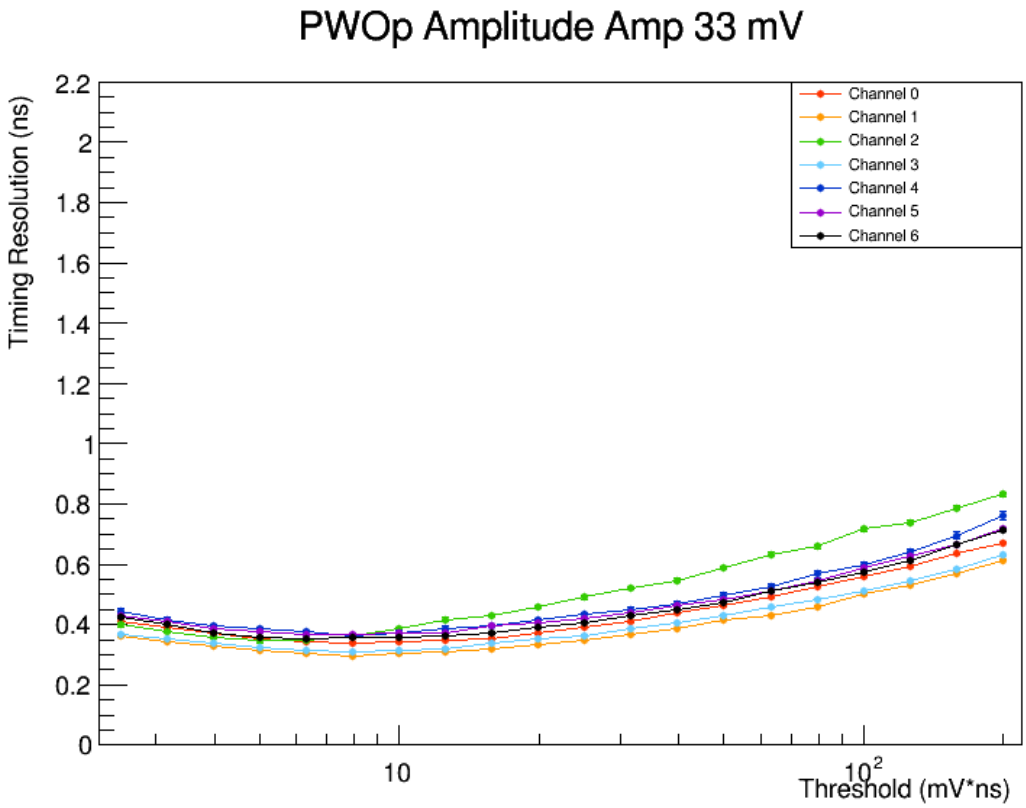

Figure A.4: Unfiltered $PbWO_4$ timing resolution vs. threshold voltage for all channels (31-35 mV in amplitude).

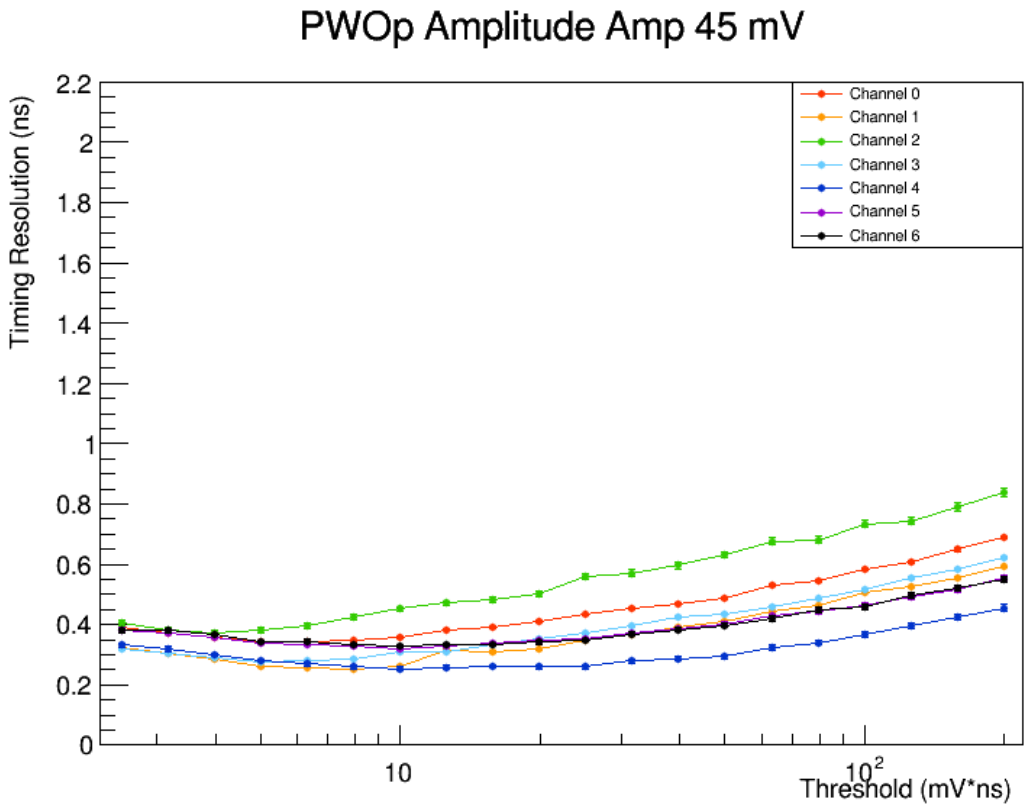

Figure A.5: Unfiltered $PbWO_4$ timing resolution vs. threshold voltage for all channels (43-47 mV in amplitude).

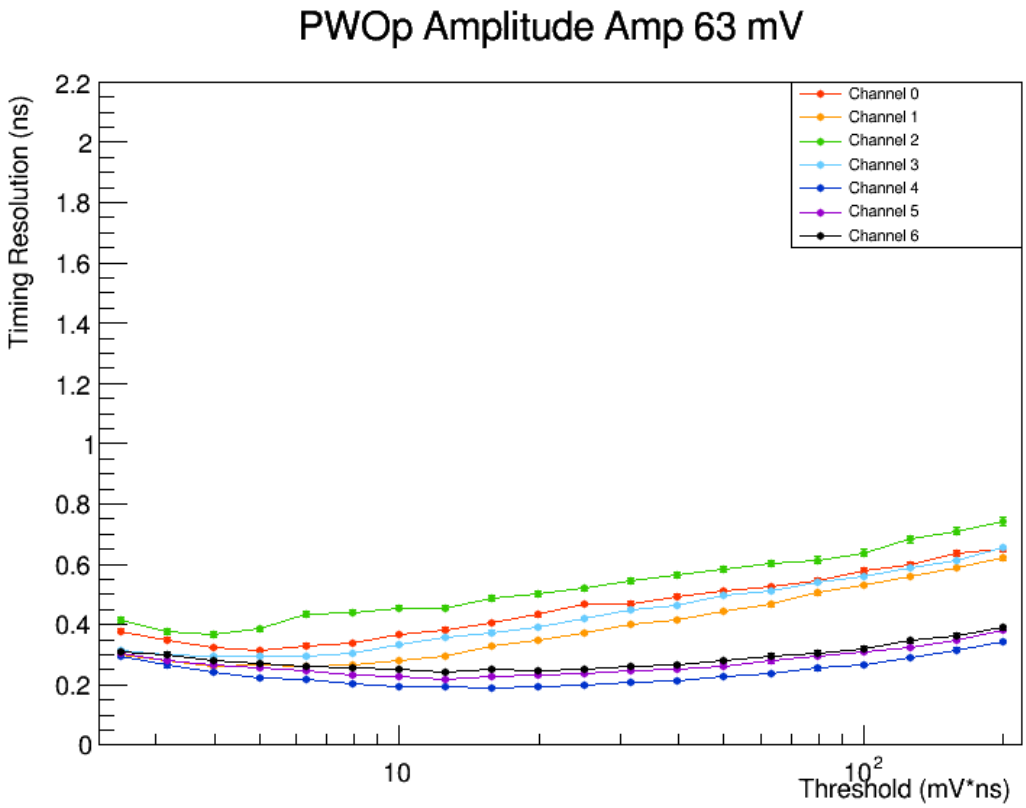

Figure A.6: Unfiltered $PbWO_4$ timing resolution vs. threshold voltage for all channels (61-65 mV in amplitude).

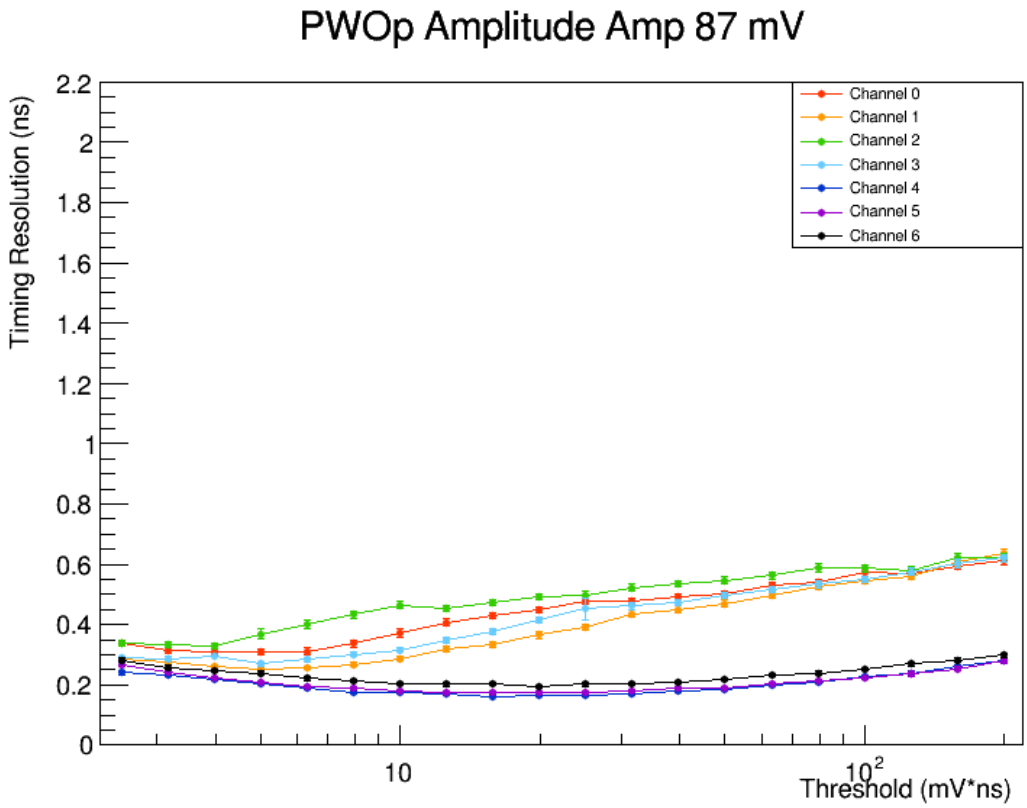

Figure A.7: Unfiltered $PbWO_4$ timing resolution vs. threshold voltage for all channels (85-89 mV in amplitude).

A.2 Section 2: Unfiltered PbWO_4 Timing Resolution by Channel

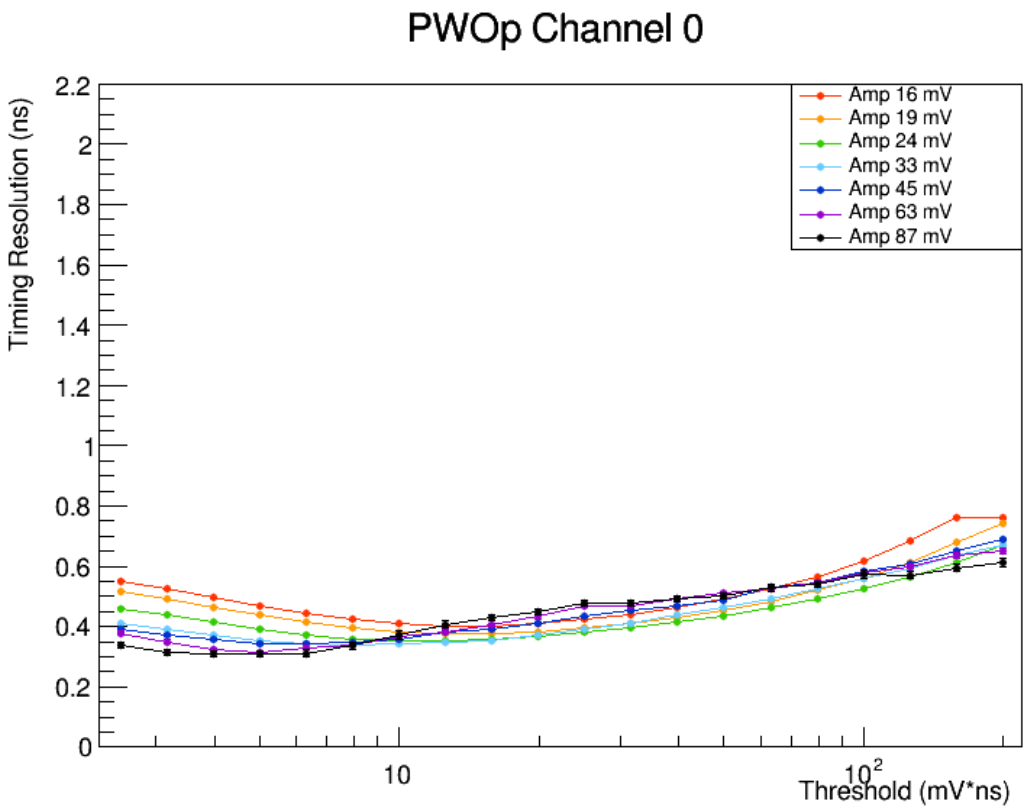

Figure A.8: Unfiltered PbWO_4 timing resolution vs. threshold voltage Channel 0.

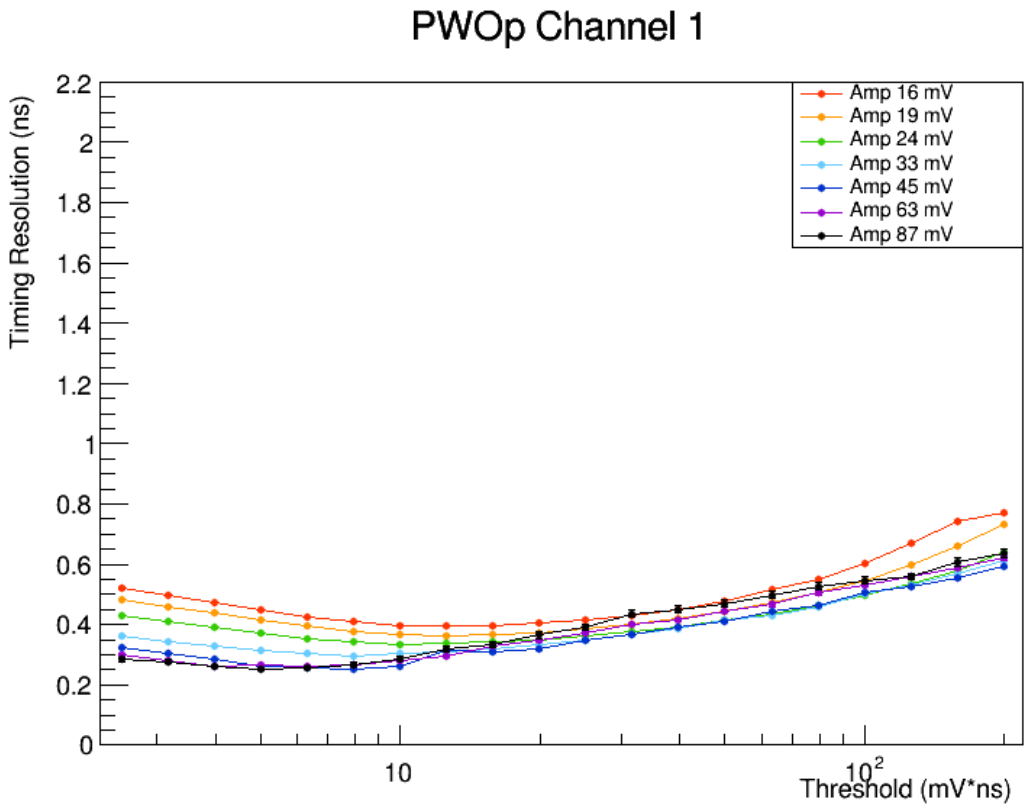

Figure A.9: Unfiltered $PbWO_4$ timing resolution vs. threshold voltage Channel 1.

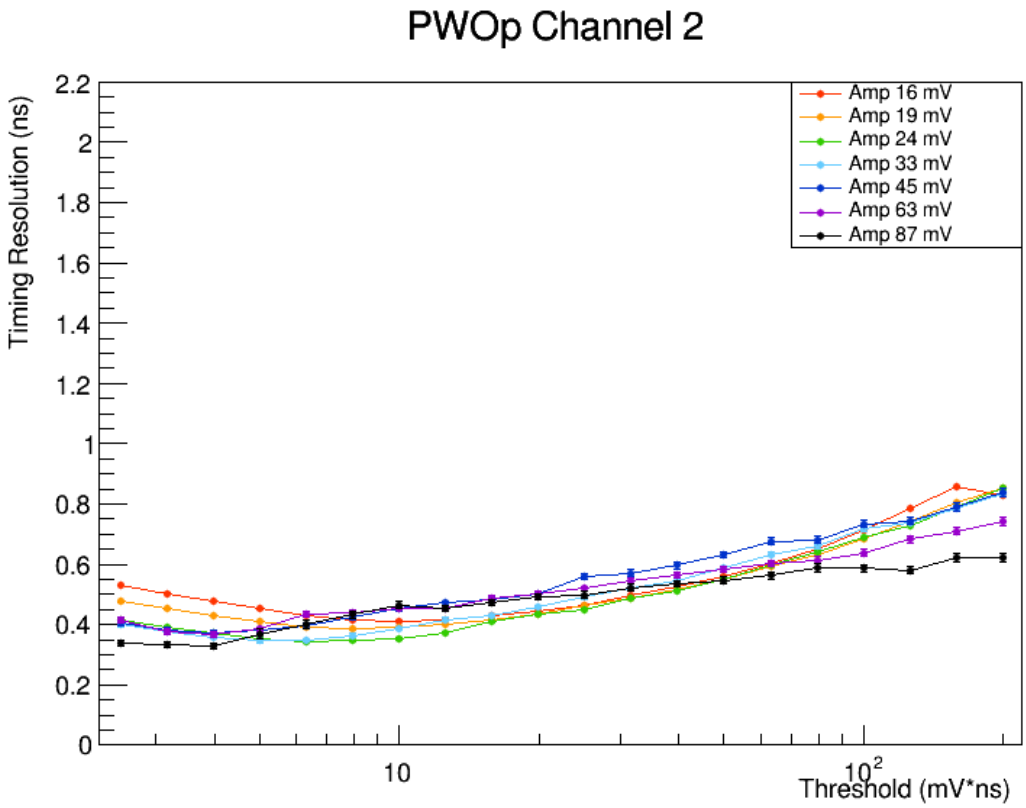

Figure A.10: Unfiltered PbWO_4 timing resolution vs. threshold voltage Channel 2.

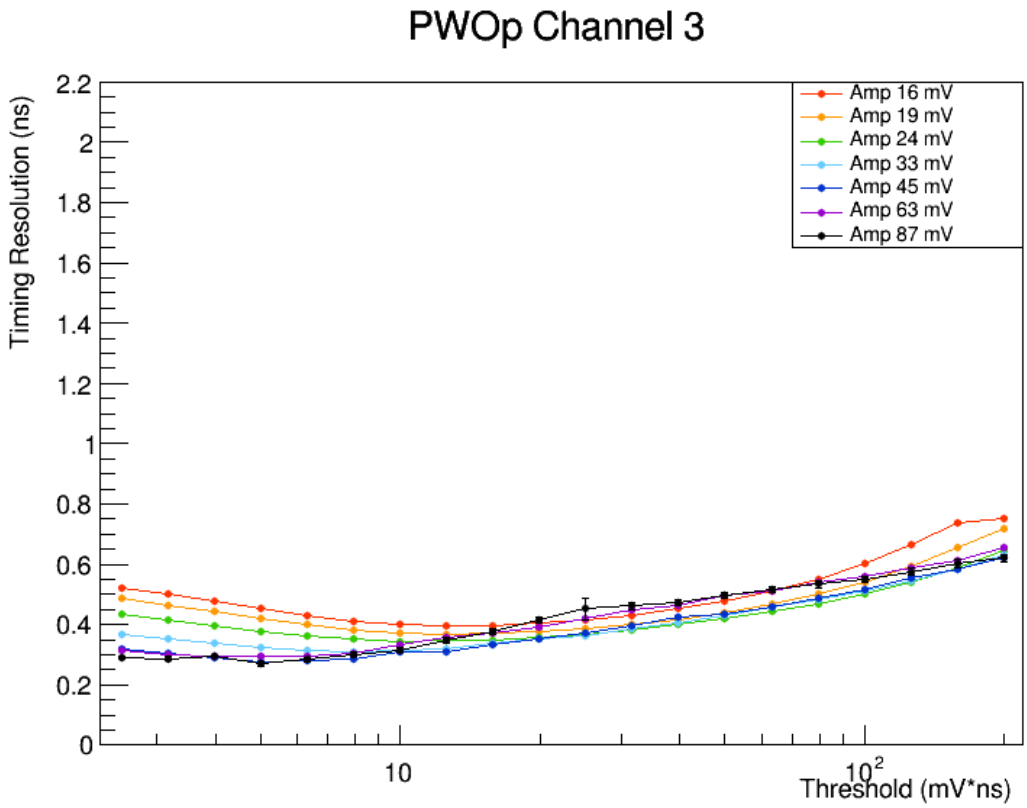

Figure A.11: Unfiltered PbWO_4 timing resolution vs. threshold voltage Channel 3.

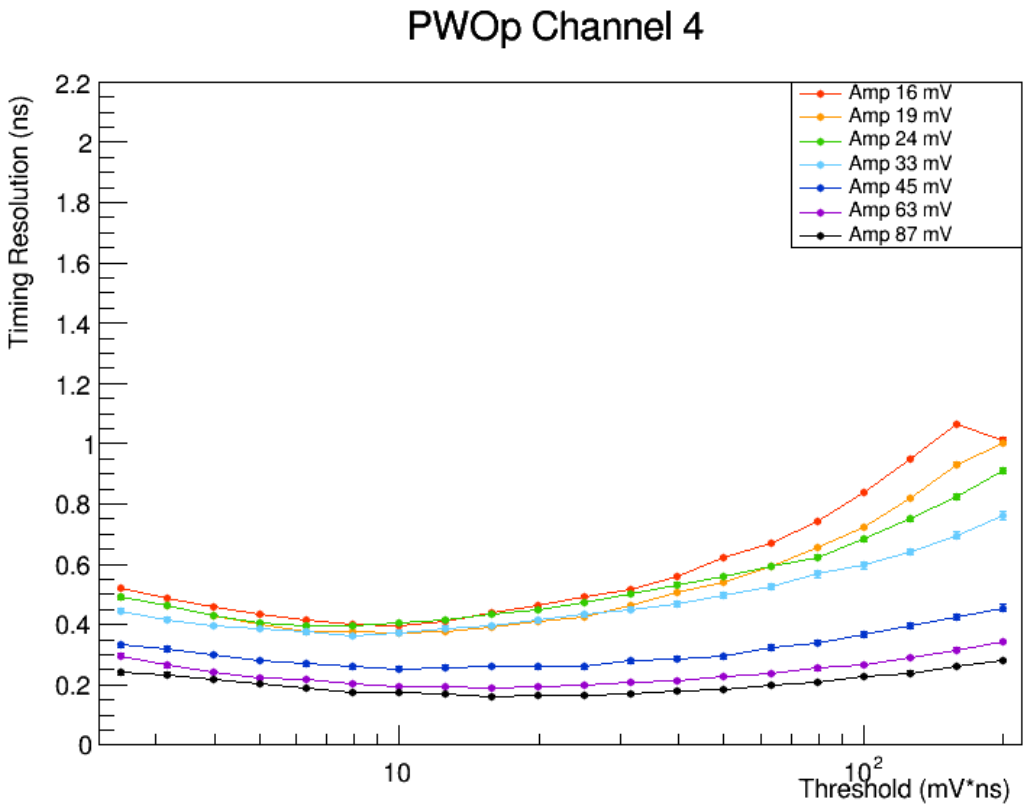

Figure A.12: Unfiltered PbWO_4 timing resolution vs. threshold voltage Channel 4.

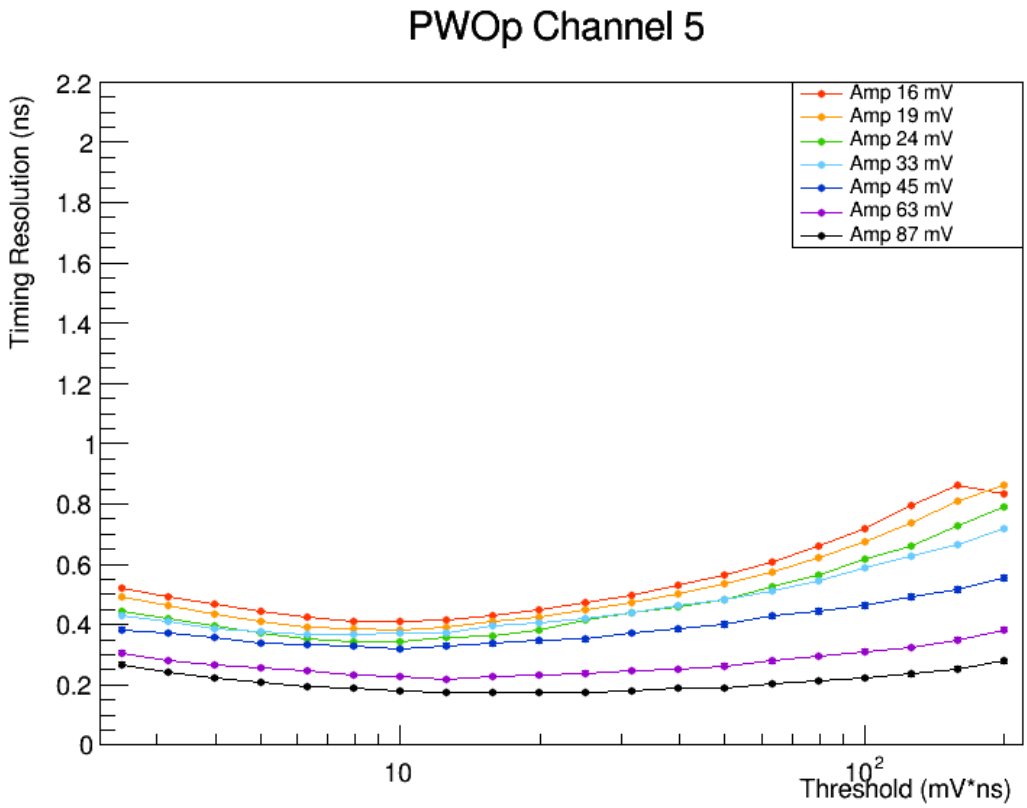

Figure A.13: Unfiltered PbWO_4 timing resolution vs. threshold voltage Channel 5.

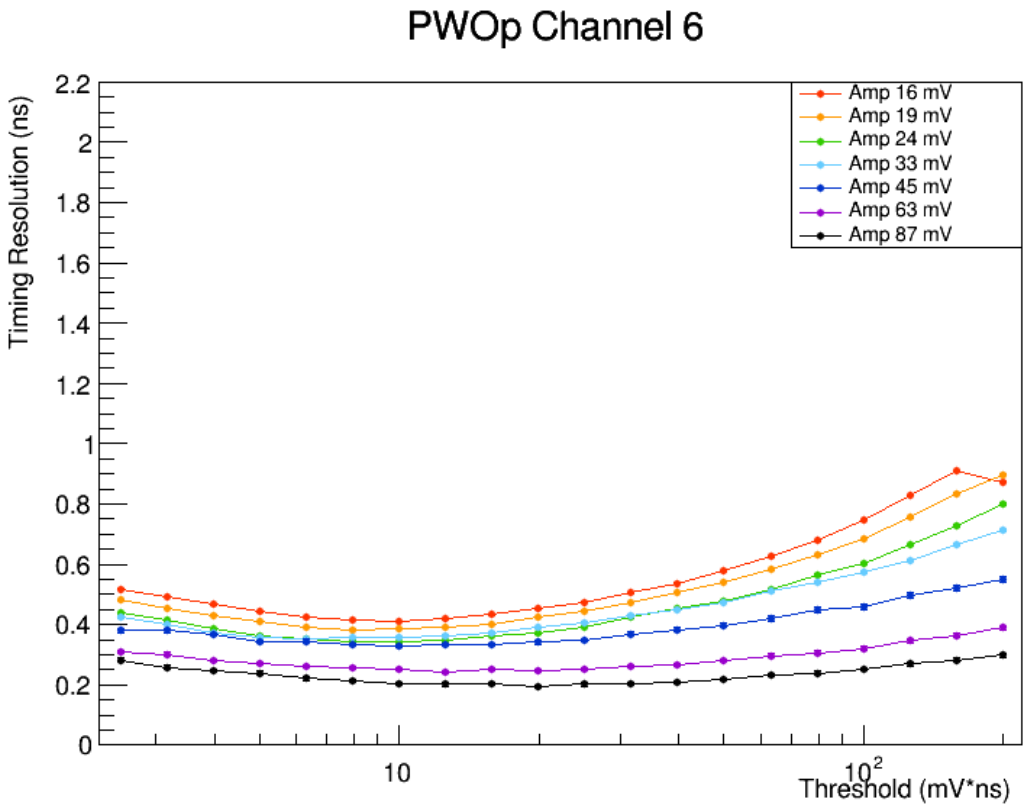

Figure A.14: Unfiltered PbWO_4 timing resolution vs. threshold voltage Channel 6.

A.3 Section 3: Filtered PbWO_4 Timing Resolution by Amplitude

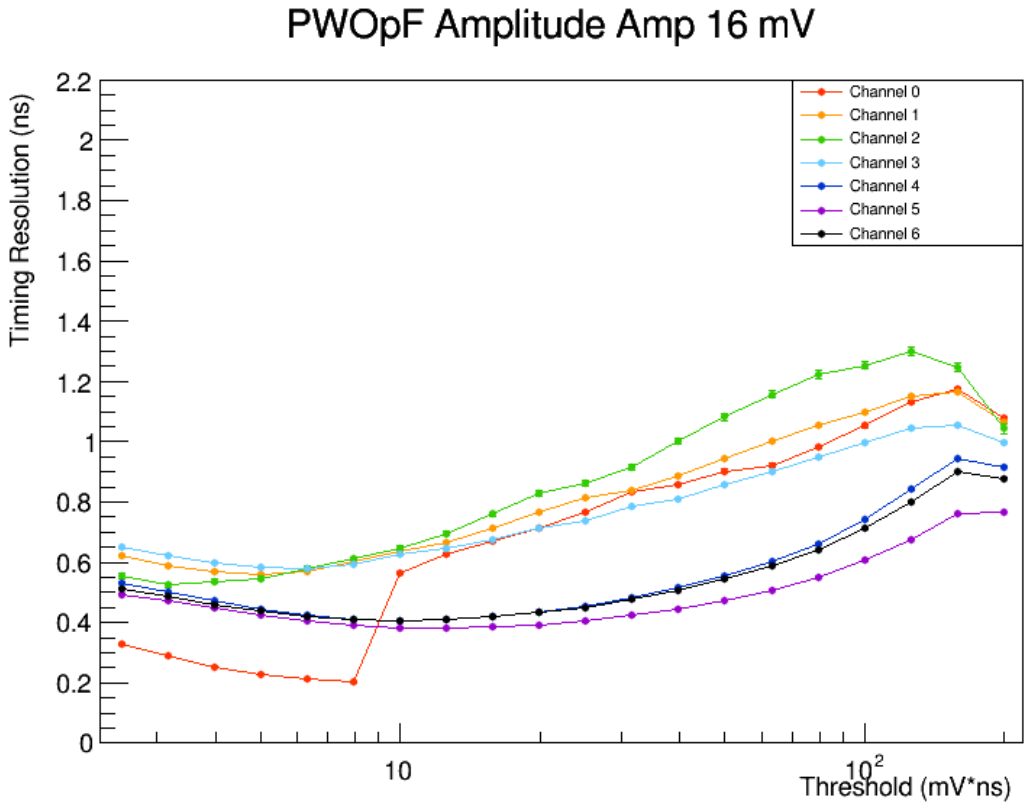

Figure A.15: Filtered PbWO_4 timing resolution vs. threshold voltage for all channels (14-18 mV in amplitude).

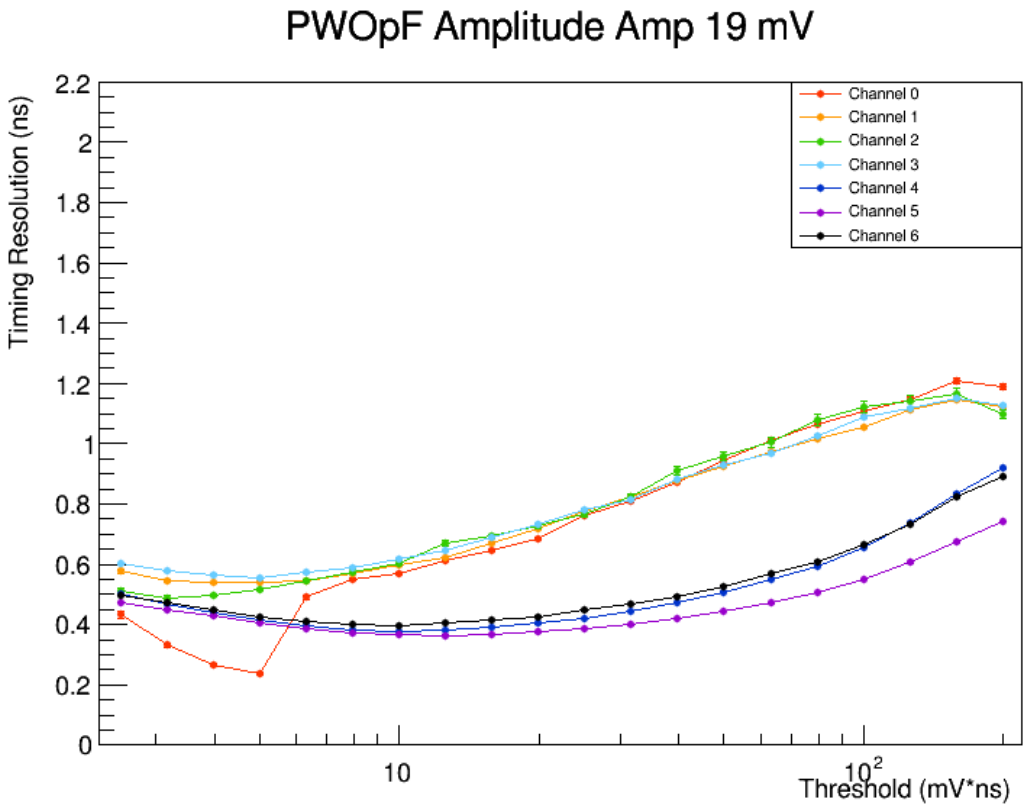

Figure A.16: Filtered PbWO_4 timing resolution vs. threshold voltage for all channels (17-21 mV in amplitude).

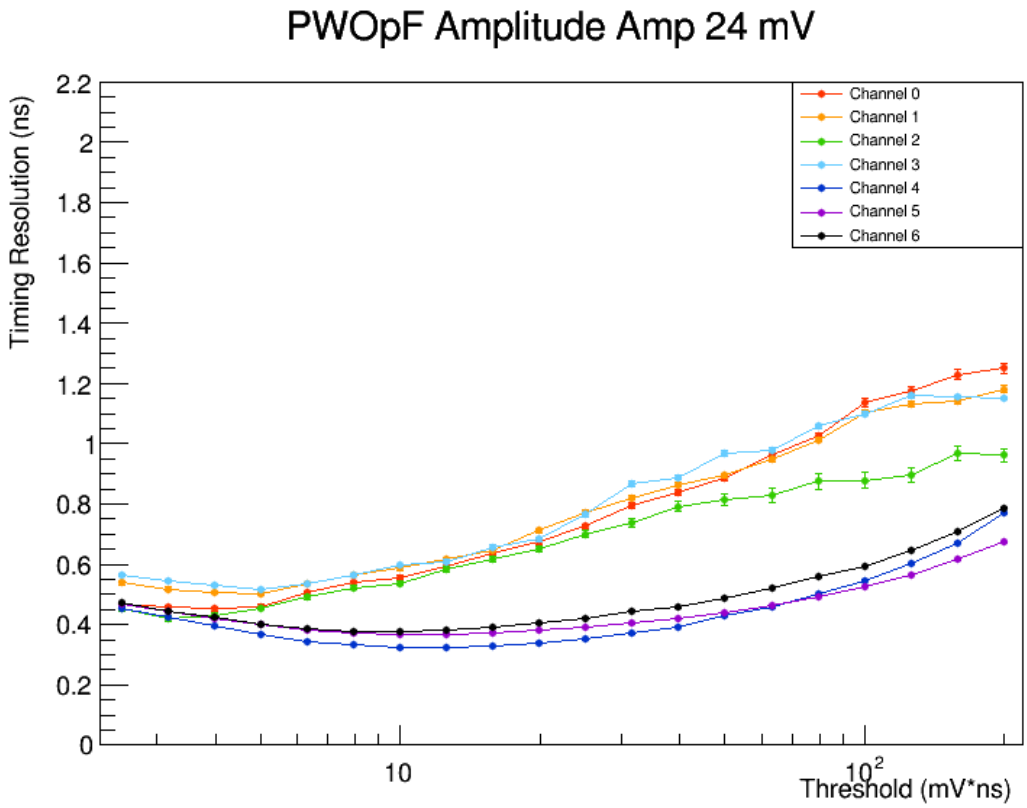

Figure A.17: Filtered $PbWO_4$ timing resolution vs. threshold voltage for all channels (22-26 mV in amplitude).

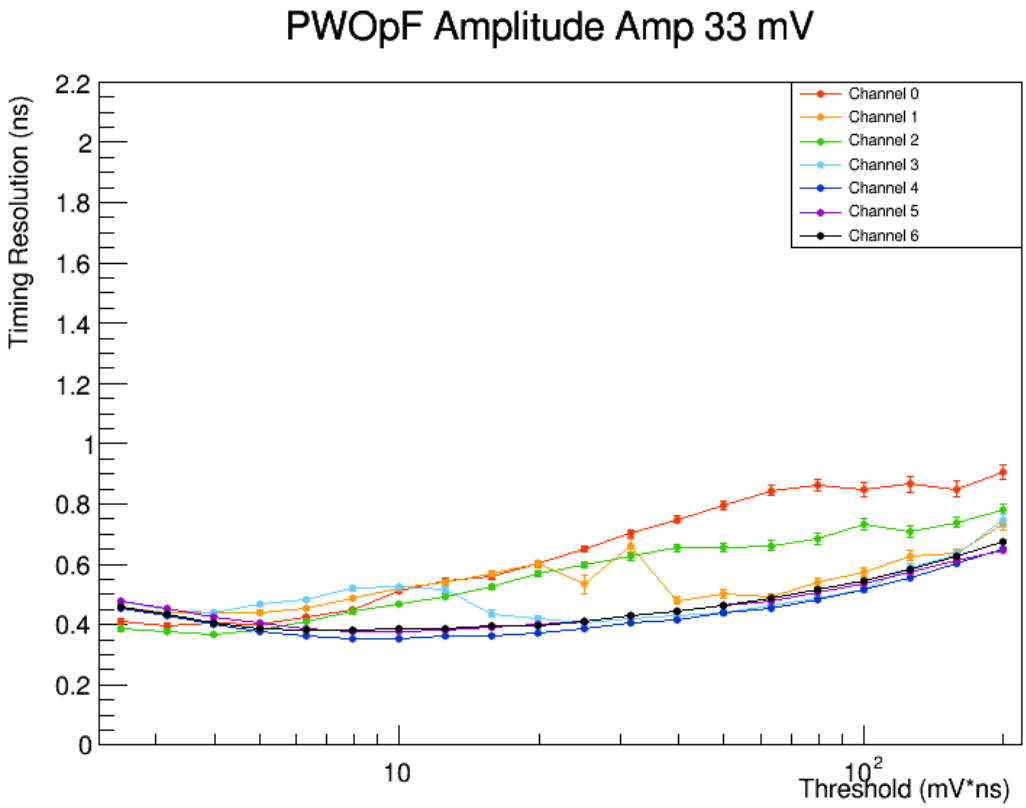

Figure A.18: Filtered PbWO_4 timing resolution vs. threshold voltage for all channels (31-35 mV in amplitude).

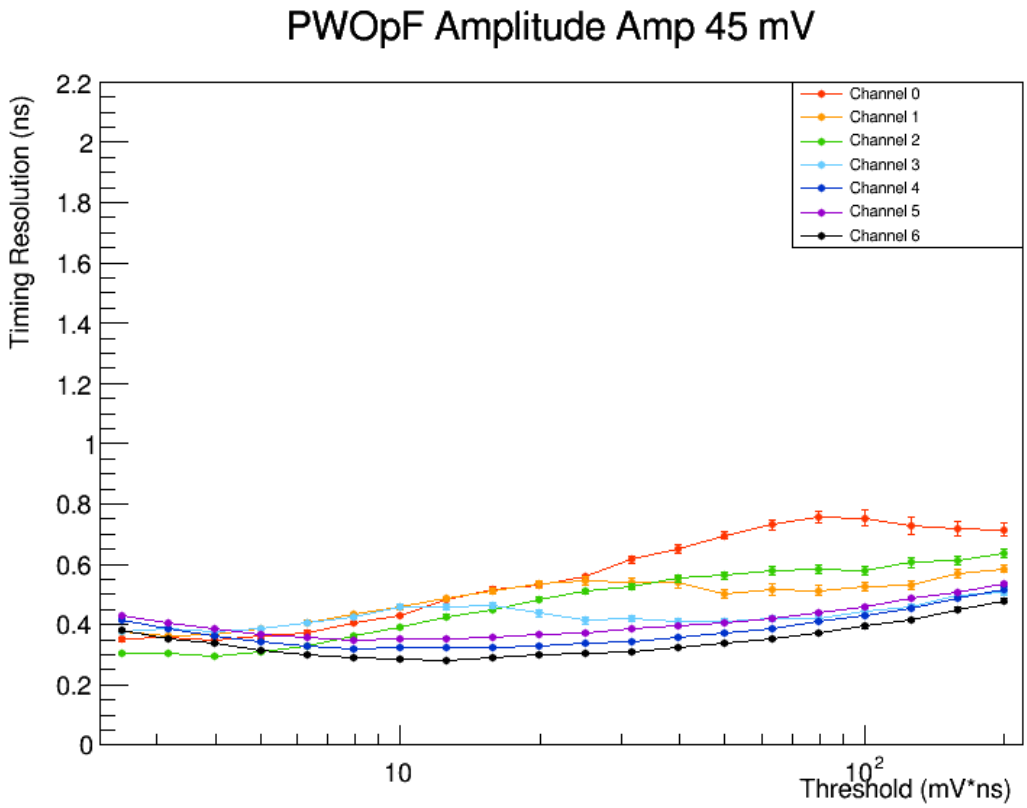

Figure A.19: Filtered $PbWO_4$ timing resolution vs. threshold voltage for all channels (43-47 mV in amplitude).

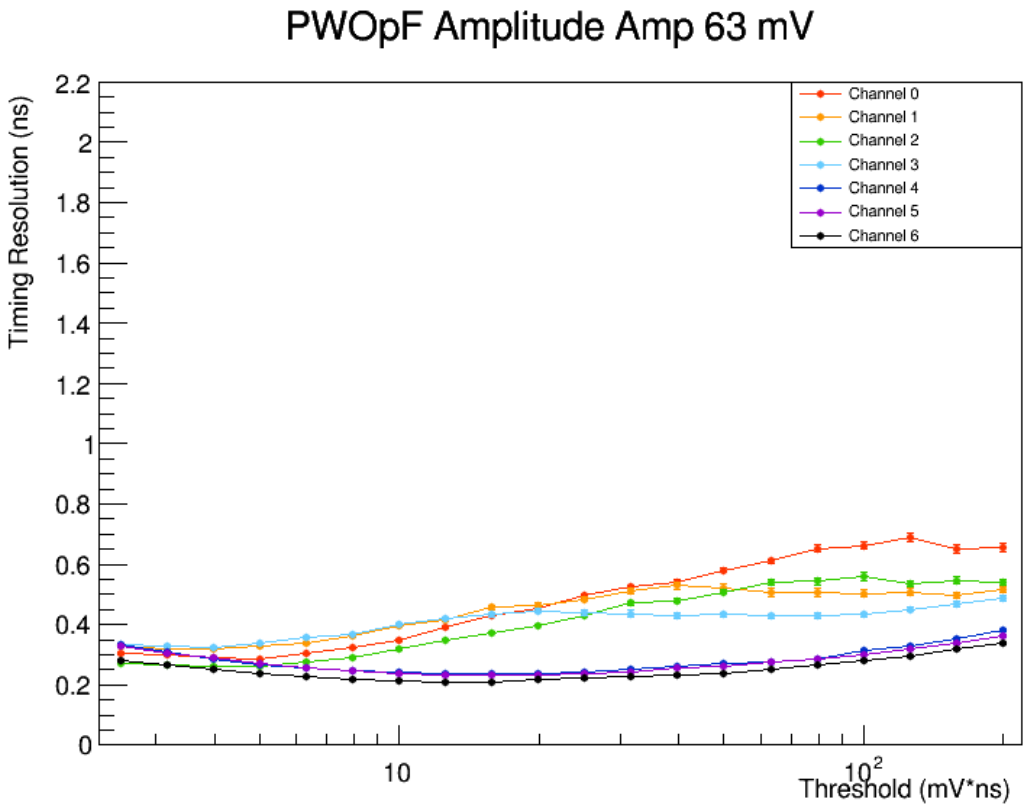

Figure A.20: Filtered $PbWO_4$ timing resolution vs. threshold voltage for all channels (61-65 mV in amplitude).

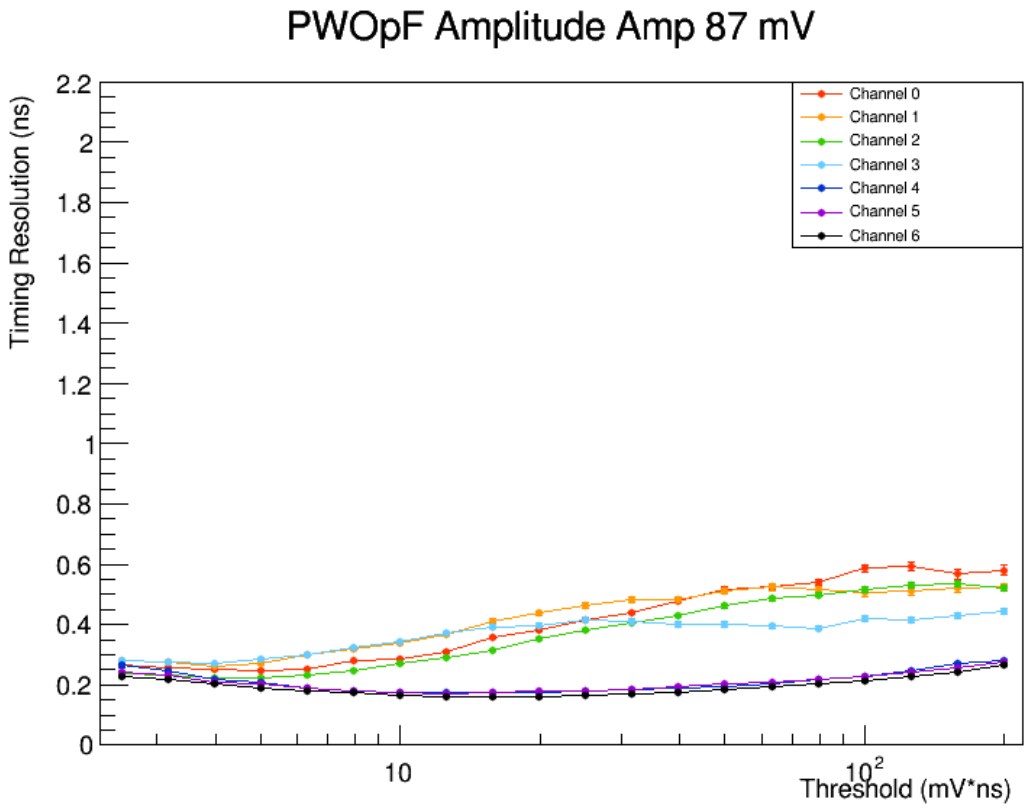

Figure A.21: Filtered $PbWO_4$ timing resolution vs. threshold voltage for all channels (85-89 mV in amplitude).

A.4 Section 4: Filtered PbWO_4 Timing Resolution by Channel

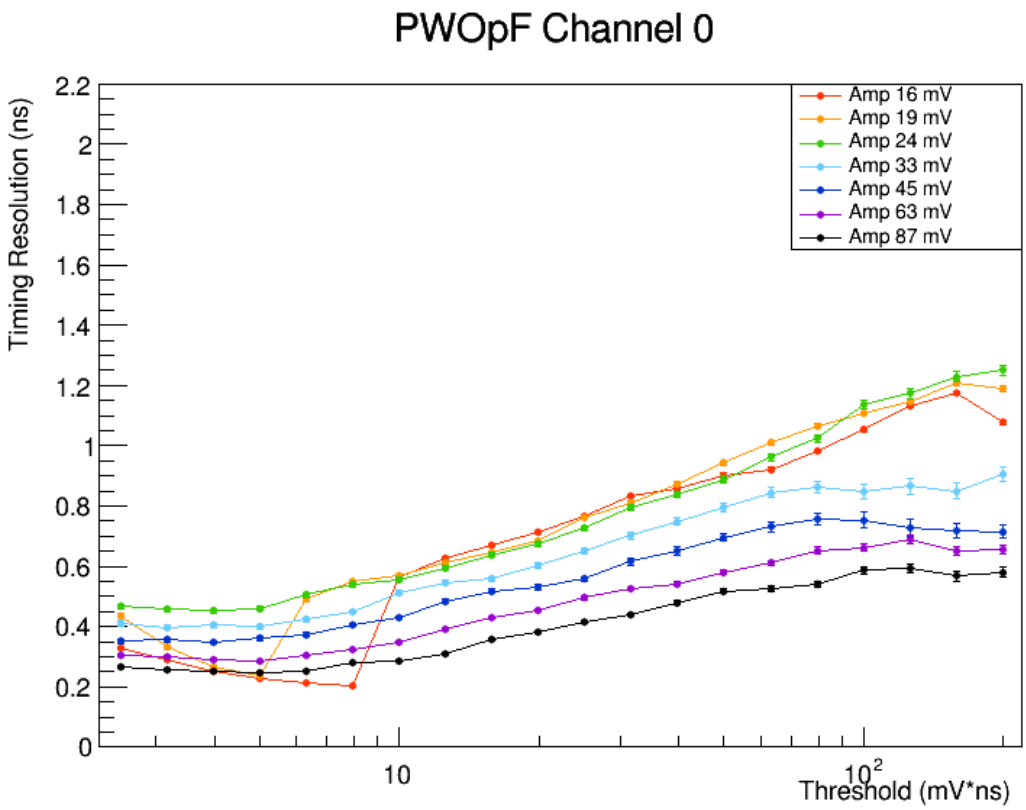

Figure A.22: Filtered PbWO_4 timing resolution vs. threshold voltage Channel 0.

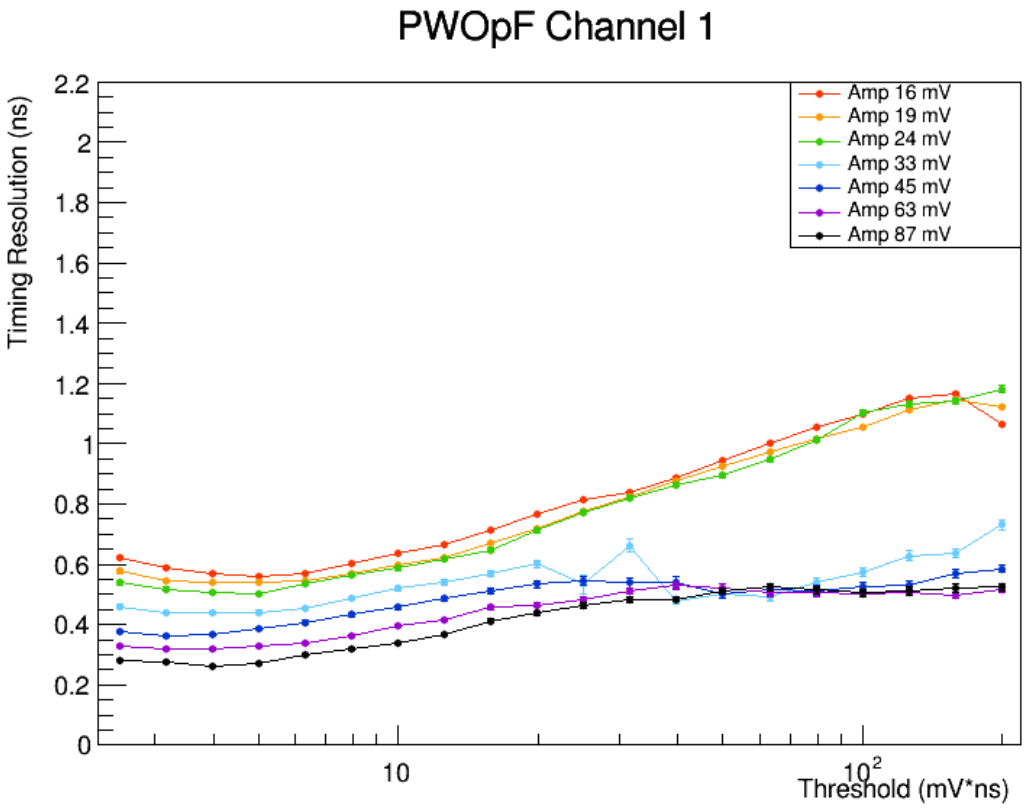

Figure A.23: Filtered PbWO_4 timing resolution vs. threshold voltage Channel 1.

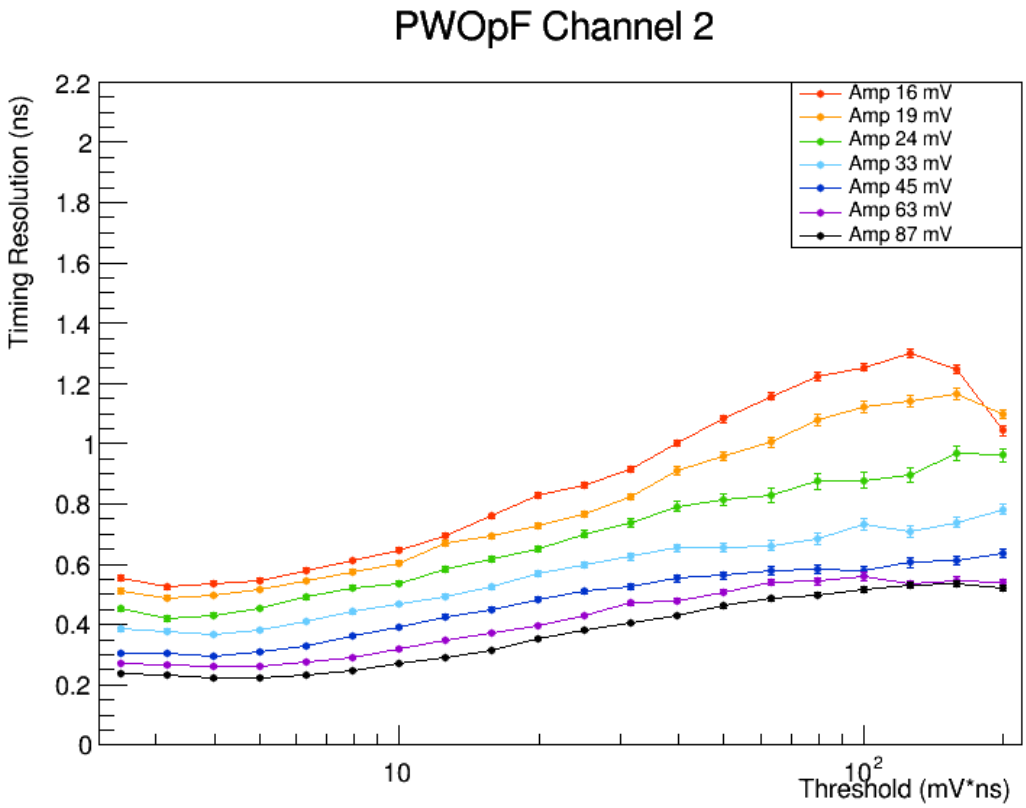

Figure A.24: Filtered PbWO_4 timing resolution vs. threshold voltage Channel 2.

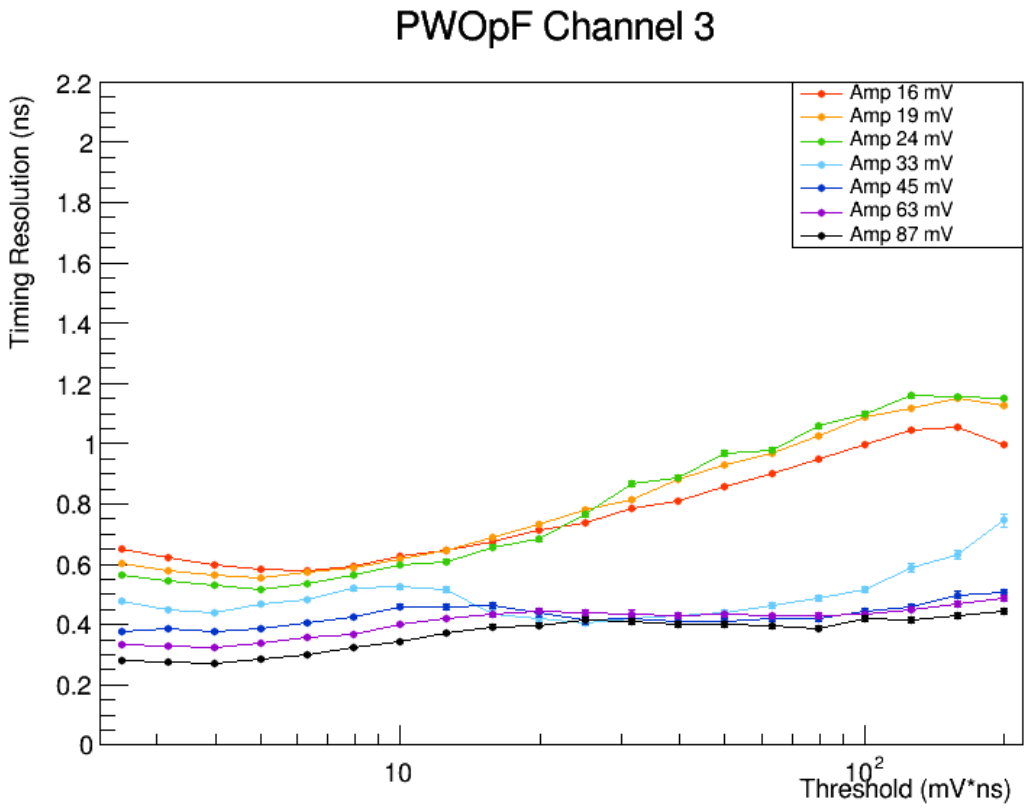

Figure A.25: Filtered PbWO_4 timing resolution vs. threshold voltage Channel 3.

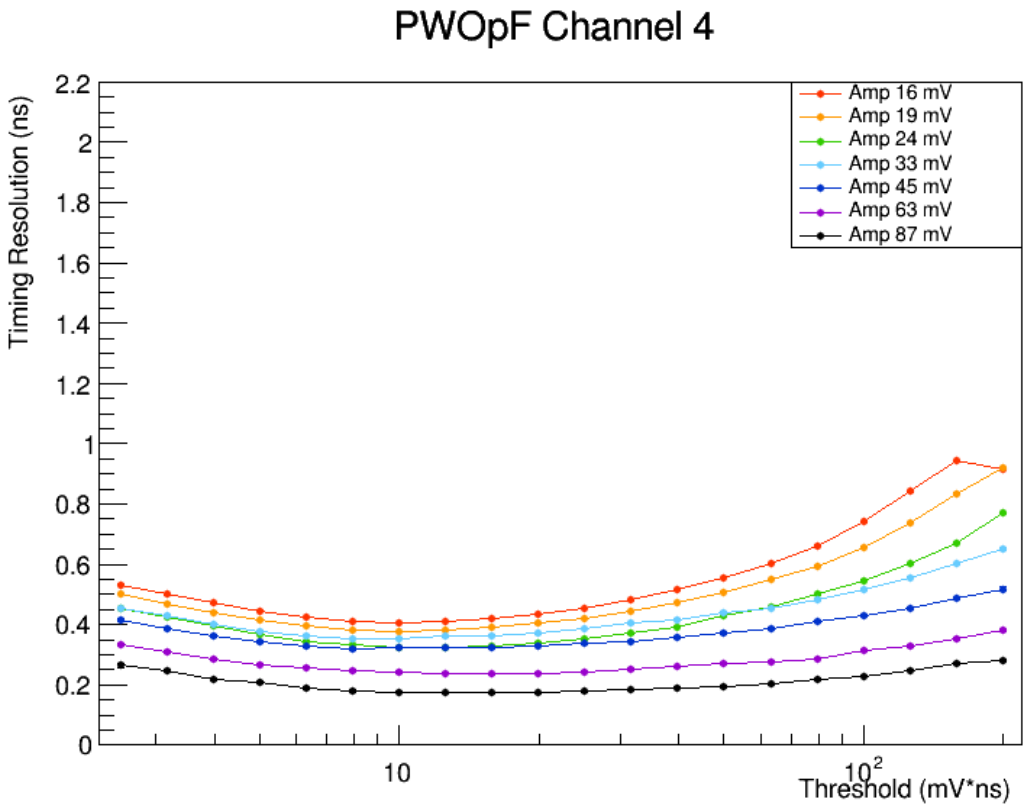

Figure A.26: Filtered PbWO_4 timing resolution vs. threshold voltage Channel 4.

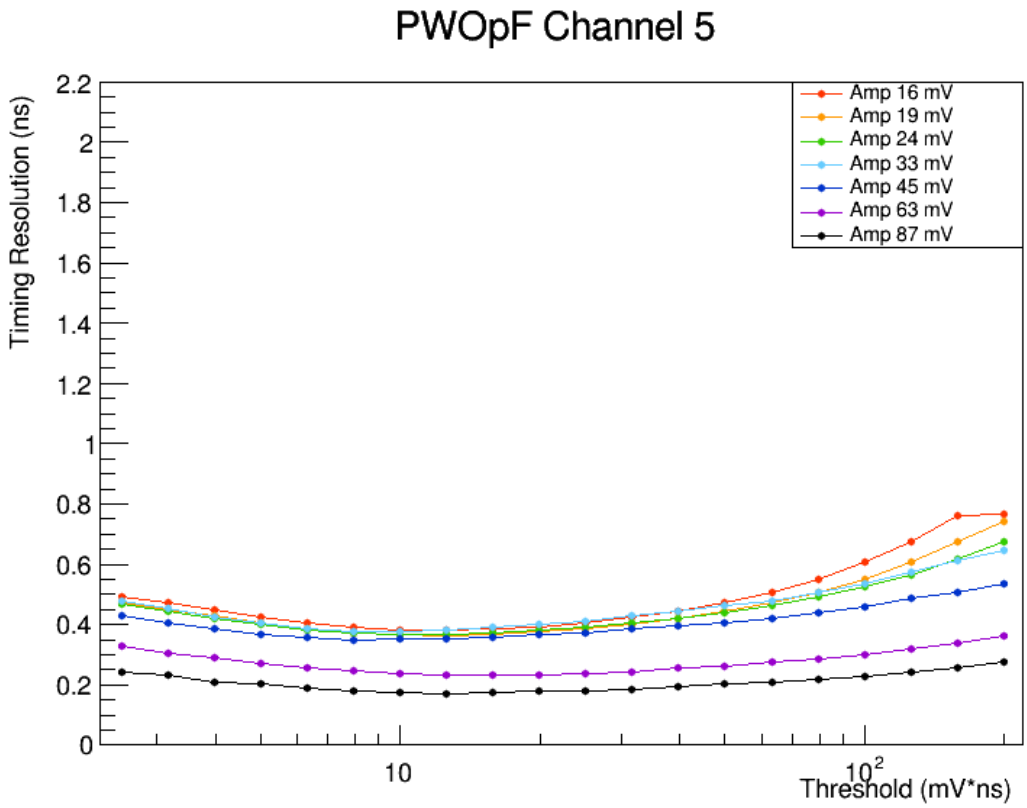

Figure A.27: Filtered $PbWO_4$ timing resolution vs. threshold voltage Channel 5.

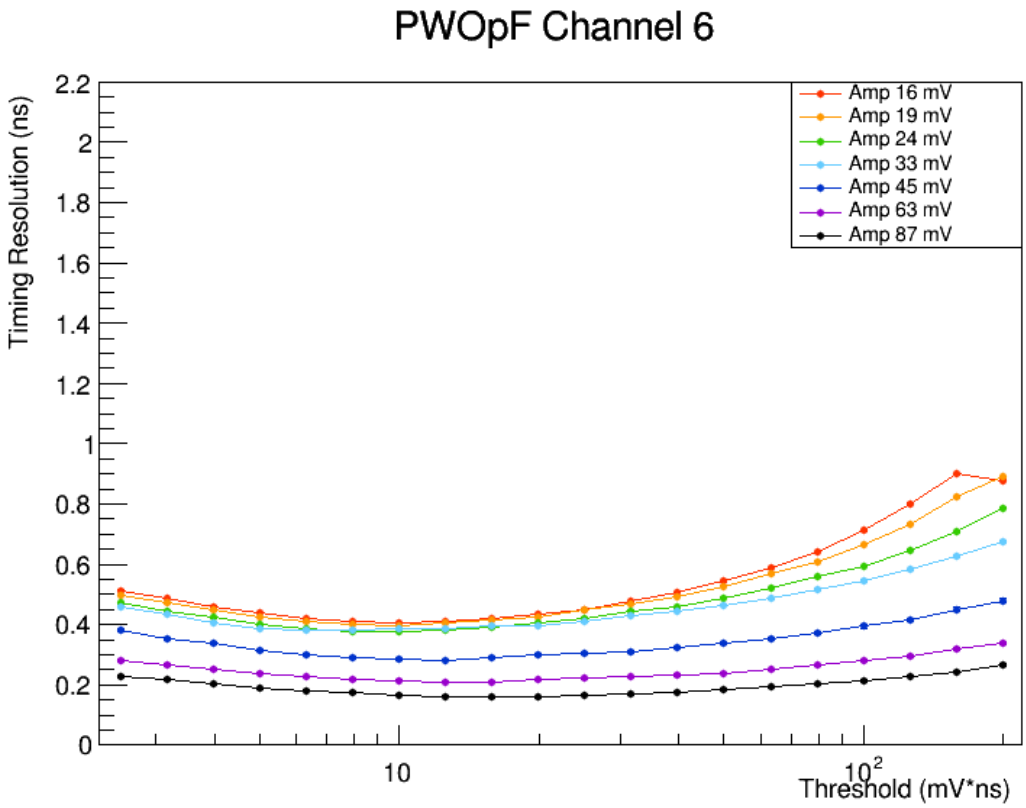

Figure A.28: Filtered PbWO_4 timing resolution vs. threshold voltage Channel 6.